Search for New Particles with Electron-inclusive Multihadronic Signature in e^+e^- Interactions

A Dissertation

by

Nobuyuki Kanematsu

Submitted to Faculty of Science of Osaka University
in Partial Fulfillment of the Requirement
for the Degree of
Doctor of Science

1990

Abstract

We have searched for new heavy particles decaying into an electron and hadrons in e^+e^- collisions with the VENUS detector at TRISTAN. The prompt electron from the decay of a new heavy particle would be clearly distinguished by the signatures of its large energy and of the large isolation from surrounding hadrons. The present work have been focused mainly on search for new quarks, new neutral leptons, and a leptoquark. There was no indication of such new particle productions in the analyzed data with the integrated luminosity of 28.8 pb^{-1} at the center of mass energy between 54 and 61.4 GeV. The result sets new constraints on masses of the new particles. The existence of new quarks with charge 2/3 and 1/3 and with mass below 29.5 GeV/c^2 and 28.0 GeV/c^2, respectively, are excluded. The new neutrino which is coupled dominantly to electron is excluded in the mass range from 9.0 to 28.5 GeV/c^2. Another type of neutral lepton, the electron-type neutral lepton, is excluded below 54.0 GeV/c^2 in the V+A type coupling case and 51.5 GeV/c^2 in the V–A type coupling case. The first-generation scalar leptoquark with charge 1/3 is excluded in the mass range from 6.0 to 22.5 GeV/c^2 and that with charge 2/3 in the mass range from 4.0 to 26.0 GeV/c^2, provided that the branching ratios of the decays into electron and into neutrino are equal.

Table of Contents

Chapter 1 Introduction

1.1. The standard model

The "standard model" is a successful theory which well describes behaviors of elementary particles. This theory contains the electroweak theory and quantum chromodynamics (QCD) both of which are based on the principle of local gauge invariance. The electroweak theory unifies the electromagnetic and the weak interaction,[1] while QCD describes the strong interaction.

1. The electroweak theory

Matter consists of point-like spin 1/2 fermions, leptons, quarks, and their antiparticles in the electroweak theory. Left-handed fermions transform as doublets and right-handed ones are singlets under SU(2) symmetry on weak-isospin, $T = (T_1,T_2,T_3)$. The T_3 eigenstates are expressed as follows;

$$\text{leptons: } l_L = \begin{pmatrix} \nu \\ l^- \end{pmatrix}_L, \; l^-_R, \qquad \text{quarks: } q_L = \begin{pmatrix} u \\ d \end{pmatrix}_L, \; u_R, d_R, \tag{1.1}$$

where the indices, L and R, denote helicity states, namely left-handed and right-handed. We call ν, l^-, u, and d, as neutrino, charged lepton, up-type quark, and down-type quark, respectively. These fermion states in the multiplets share the same weak-hypercharge Y which is the eigenvalue of the quantum state of the U(1) symmetry. T_3 and Y are related to the electric charge Q through the equation, $Q = T_3 + Y/2$. In addition to the fermions, scalar bosons called as Higgs particles, are introduced as a complex isodoublet in $SU(2)_L$ in the minimal standard model. The specifications on leptons, quarks, and Higgs particles are summarized in table 1.1.

	lepton			quark				Higgs	
	ν	l^-_L	l^-_R	u_L	d_L	u_R	d_R	ϕ^+	ϕ^0
T	1/2	1/2	0	1/2	1/2	0	0	1/2	1/2
T_3	1/2	−1/2	0	1/2	−1/2	0	0	1/2	−1/2
Q	0	−1	−1	2/3	−1/3	2/3	−1/3	+1	0
Y	−1	−1	−2	1/3	1/3	4/3	−2/3	1	1

Table 1.1 Specifications of leptons, quarks, and the minimal Higgs.

Spin 1 bosons which correspond to the generators of the symmetry group are called gauge bosons. The introduction of Higgs causes the so-called spontaneous break-down of the original $SU(2)_L \times U(1)$ symmetry and makes the gauge bosons and

fermions massive. Another U(1) symmetry with a generator Q arises after the symmetry breaking, constructing a well established theory called quantum electrodynamics (QED) with a massless gauge boson, photon γ. Three massive gauge bosons, charged weak bosons $W^{\pm}$ and a neutral weak boson Z^0, mediate the weak interaction. There is only one neutral Higgs boson H^0 which physically remains after the spontaneous symmetry breaking. However, the masses of the fermions and H^0 are left as unknown parameters. Besides them, there are three independent parameters which determine the strengths of the electroweak interactions. They are usually chosen to be fine structure constant α, weak mixing angle θ_w, and either Z^0 mass M_Z or Fermi constant G_F.

Quarks and leptons have several species. The mass eigenstates, flavors, are classified in ascending order of mass as follows;

$$\text{leptons: } \begin{pmatrix} \nu_1 \\ e^- \end{pmatrix}, \begin{pmatrix} \nu_2 \\ \mu^- \end{pmatrix}, \begin{pmatrix} \nu_3 \\ \tau^- \end{pmatrix}, \quad \text{quarks: } \begin{pmatrix} u \\ d \end{pmatrix}, \begin{pmatrix} c \\ s \end{pmatrix}, \begin{pmatrix} t \\ b \end{pmatrix}. \tag{1.2}$$

These groups with a repetitive structure are called generations. The corresponding particle in a different generation has the same quantum numbers. In general, mass eigenstates do not always coincide with gauge eigenstates because masses are not given by the gauge interaction but by ad hoc Yukawa interactions with the Higgs particle. Assuming all neutrinos to be massless, any neutrino state can be a mass eigenstate. Therefore, ν_1, ν_2, and ν_3 are usually replaced by the gauge (weak) eigenstates ν_e, ν_μ, and ν_τ and the different lepton generations are completely decoupled. On the other hand, all quarks are massive and actually there is a small mixing between the quark generations in the weak interaction, which is represented by a unitary, Kobayashi-Maskawa (K-M) matrix V as follows;[2]

$$\begin{pmatrix} d_w \\ s_w \\ b_w \end{pmatrix} = \begin{pmatrix} V_{ud} & V_{us} & V_{ub} \\ V_{cd} & V_{cs} & V_{cb} \\ V_{td} & V_{ts} & V_{tb} \end{pmatrix} \begin{pmatrix} d \\ s \\ b \end{pmatrix}, \tag{1.3}$$

where d_w , s_w, and b_w are the weak eigenstates coupled to u, c, and t, respectively. K-M matrix can be determined by three rotational angle parameters and one phase parameter which accounts for CP violating phenomena.

2. QCD

Quarks are SU(3) triplets in QCD, that is, each quark (antiquark) has one of three color (anticolor) charges. The eight SU(3) generators physically correspond to massless gauge bosons, gluons. A gluon g possesses a color and an anticolor, mediating the strong interaction between quarks. Because of its non-Abelian nature, gluons also interact with each other and the visible strength of the strong interaction increases according to the distance. This feature is responsible for the quark-confinement. Quarks and gluons, so-called partons, always collapse into hadrons. At short distances, namely

at high momentum transfer squared q^2, the coupling strength become so small that a perturbative approach can be made.

3. Status of the standard model

Now, the status of the standard model is summarized. The electroweak theory, having 17 parameters to be measured, seems quite successful. There is no evidence which contradicts the theory though there are two missing members, t-quark and H^0. As for the strong interaction, a perturbative approach of QCD successfully explains many phenomena at high energy. But the strong interaction in low q^2 region such as the jet-formation mechanism and the mass-spectrum of hadrons have not been clearly understood. Moreover, there remain some problems which are not well explained by the present theory. For example, the origin and the number of the generations cannot be given theoretically. The theory seems to be far from the ultimate theory, rather a well established phenomenology.

In the experimental approach, it is an important test of the electroweak theory to find the missing members and to do precise measurements of the parameters. Models beyond the standard theory need experimental evidences if they were to describe the real world. In order to inspire the theoretical approach, the shortest way may be to study interactions in unprobed energy region, where new phenomena may appear.

1.2. e^+e^- colliding experiments

Because both an electron, e^-, and its antiparticle, a positron, e^+, are point-like particles, the beam energy is effectively utilized in e^+e^- collision and the ensuing reactions are simple to understand. As a consequence of such advantages of e^+e^- colliding experiments, various contributions to particle physics have been made. In 1974, ψ-series of the $c\bar{c}$ bound states with masses above 3 GeV/c^2 were first observed at SLAC using the e^+e^- collider, SPEAR.[3] The discovery of c-quark completed the second generation. In 1975, τ-lepton was discovered also at SPEAR.[4] This was the first observation of a third-generation particle. The second member, the down-type quark b, was discovered in 1977 at the proton-nucleus collision experiment,[5] and then, Υ-series of the $b\bar{b}$ bound states with masses around 10 GeV/c^2 were clearly resolved in e^+e^- collisions at DORIS storage ring, DESY and at CESR, Cornell.[6] The center of mass energy was increased using PEP accelerator at SLAC and PETRA at DESY up to 46.8 GeV. Though the predicted t-quark was not found there, the results showed good agreements with the standard model. In the electroweak theory, $\sin^2\theta_W$ was determined by the forward-backward asymmetry of lepton-pair productions,[7] combining the results from the neutrino experiments. In a QCD related field, a hard gluon emission was

clearly observed as a three-jet event and its cross section agreed well with the perturbative calculation of QCD.[8]

In 1986, just after PEP and PETRA had finished their operation, TRISTAN in Japan began to work. The first target of TRISTAN project was of course t-quark and in order to find it and also with other probable subjects in mind, a general purpose detector, VENUS, was installed. TRISTAN had been the world-highest-energy e^+e^- collider before SLC at SLAC and LEP at CERN began to work with center of mass energy around Z^0 pole in summer of 1989.

1.3. Motivation and our strategy to find new particles

The most important subject at the highest-energy machine is to search for new particles. Various new particles are expected in the progressive theories. Among them, the most prominent one is the top quark (t-quark) which was predicted by the standard theory, but so far eluded the experimentalists' scrutiny. Either an extension of or a departure from the standard model predicts a variety of new particles, a new charge – 1/3 quark b', a new neutrino N, an another heavy neutral lepton E^0, a leptoquark χ, and so on. These which are relevant to the present analysis will be described in details later. Then, there is always a possibility of finding new particles which no one has expected. It is important to search for such new particles in a broadest approach as possible as extensively. Because the new heavy particle will be produced nearly at rest, its decay-products will be emitted isotropically. Thus, the heavy new particle production will have a characteristic signature of spherical event shape compared with ordinary processes, *i.e.* known quark production. However, it is generally difficult to separate a hadronically decaying new particle from multijet events of higher order QCD processes. Many new particles in our consideration are expected to decay semileptonically into an electron, e, and hadrons. In this thesis, the term, "electron", usually includes its antiparticle. Such e which is a direct decay-product of a heavy particle tends to be energetic and isolated from other decay-products. We have actually made a direct search for new particles by tagging isolated e in a multihadronic final state, which will make better separation of the new particle from the known processes. It is unusual for e from light known particles to satisfy both requirements of "energetic" and "isolated" because of the smallness of releasing energy in decay and of the large boost of the parent particle. Therefore, the background from higher order QCD processes will be nearly completely removed while higher order QED processes of two-photon-exchange interaction will dominate the background in spite of the small cross section.

1.4. Mechanisms of inclusive electron productions

1.4.1. Production processes of known quarks

Before searching for new particles, we must know the behaviors of ordinary processes of known particle productions. We introduce here the ordinary production mechanisms of inclusive e productions.

1. Quark-pair production

In e^+e^- collision, $b\bar{b}$ and $c\bar{c}$ productions yield e's in their decay. First, we review general properties of a fermion-pair production and a semileptonic decay as shown in figure 1.1. According to the lowest order calculation in the electroweak theory, the differential cross section for a fermion-pair production is given as follows;

$$\begin{aligned}\frac{d\sigma}{d\cos\theta} = \frac{\pi\alpha^2\beta}{2s}\Big[&Q_e^2Q_f^2\{1+\cos^2\theta+(1-\beta^2)\sin^2\theta\}\\ &+2\mathrm{Re}(\chi)Q_eQ_f\{g_V^e g_V^f(1+\cos^2\theta+(1-\beta^2)\sin^2\theta)+2g_A^e g_A^f\beta\cos\theta\}\\ &+|\chi|^2\{(g_V^{e2}+g_A^{e2})g_V^{f2}(1+\cos^2\theta+(1-\beta^2)\sin^2\theta)\\ &+(g_V^{e2}+g_A^{e2})g_A^{f2}\beta^2(1+\cos^2\theta)+8g_V^e g_V^f g_A^e g_A^f\beta\cos\theta\}\Big],\end{aligned} \tag{1.4}$$

$$\chi = \frac{1}{4\sin^2\theta_w\cos^2\theta_w}\frac{s}{s-M_z^2+iM_z\Gamma_z},$$

$$\beta = \sqrt{1-\frac{4m_f^2}{s}},$$

$$Q_e = -1,\ g_V^e = -\frac{1}{2}+2\sin^2\theta_w,\ g_A^e = -\frac{1}{2},$$

$$g_V^f = T_{3f}-2Q_f\sin^2\theta_w,\ g_A^f = T_{3f},$$

where Q_f and m_f are the charge and the mass of the fermion, θ is a polar angle which is defined by the angle between the incoming e^- and the outgoing fermion, and Γ_z is Z^0 width. The variable s is a center of mass energy squared, calculated by $4E_{beam}^2$, where E_{beam} is the beam energy.

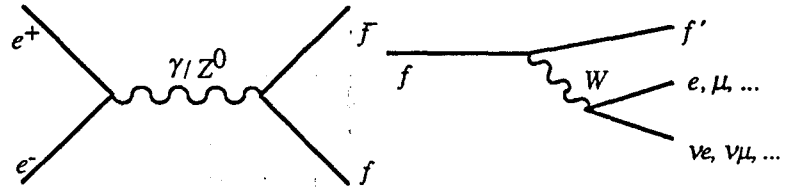

Figure 1.1 Diagrams of a fermion-pair production and a semileptonic weak decay, where f is the weak-isospin-flipped fermion.

There are some special features if the fermion is a quark. The cross section should be multiplied by 3 due to the color degrees of freedom and moreover there are higher order QCD processes such as gluon emissions. The QCD effect amounts to 5 % increase in the total cross section at TRISTAN energy. The event from a quark-pair production often forms a two-jet structure where two clusters of hadrons are ejected in opposite direction. Hard gluon emissions result in a multijet events. Fragmentation mechanism of hadrons which explains the jet-formation is not completely resolved but there are some phenomenological models to describe this. Figure 1.2 shows a schematic diagram of multihadron production.

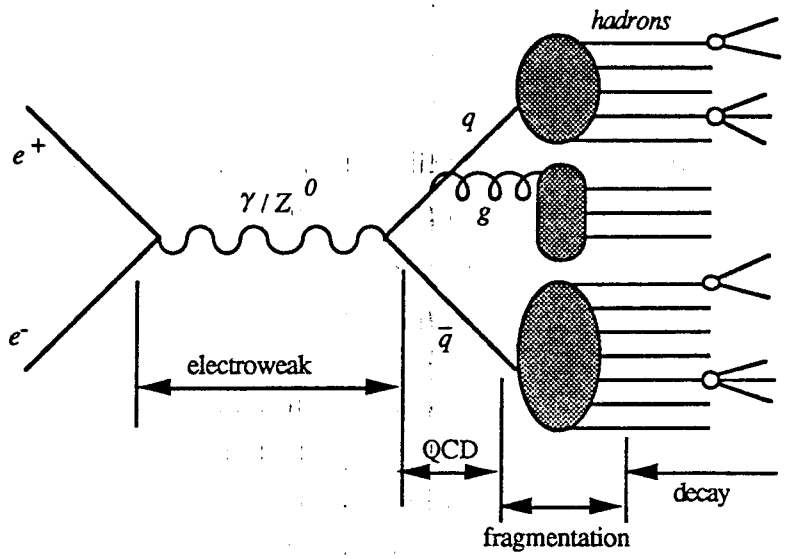

Figure 1.2 A schematic diagram of multihadron production in e^+e^- annihilation.

Neglecting spin polarizations and all the decay product masses, the width for a weak charged current decay of a fermion into three fermions, $f \to gf'g'$, is calculated as;

$$d\Gamma_f = |V_{fg}|^2 |V_{f'g'}|^2 G_F^2 \frac{m_f}{E_f} (2\pi)^{-5} 64 (p_f p_{g'})(p_g p_{f'}) \frac{d^3p_g}{2E_g} \frac{d^3p_{f'}}{2E_{f'}} \frac{d^3p_{g'}}{2E_{g'}} \delta^4(p_f - p_g - p_{f'} - p_{g'}), \quad (1.5)$$

where p_f, p_g, $p_{f'}$, and $p_{g'}$ denote four momenta of the fermions, where f' has the same T_3 value as that of f, while g and g' have the flipped T_3 value.

The weak charged current decay of a heavy flavored hadron is well approximated by the spectator model as shown in figure 1.3. The accompanying light quark in the hadron, so called, a spectator quark, is considered to be irrelevant with decay. Neglecting all the masses of the decay products, the semileptonic branching ratio, for example, for $b \to ce^-\bar{\nu}_e$, is given by;

$$B(b\to ce^-\bar{\nu}) = \frac{\Gamma_{e\nu_e}}{\Gamma_{ud_W}+\Gamma_{cs_W}+\Gamma_{e\nu_e}+\Gamma_{\mu\nu_\mu}+\Gamma_{\tau\nu_\tau}}\frac{|V_{cb}|^2}{|V_{ub}|^2+|V_{cb}|^2} \approx \frac{1}{9}, \tag{1.6}$$

assuming that,

$$\frac{|V_{ub}|^2}{|V_{cb}|^2} \approx 0, \text{ and } \Gamma_{ud_W} = \Gamma_{cs_W} = 3\Gamma_{e\nu_e} = 3\Gamma_{\mu\nu_\mu} = 3\Gamma_{\tau\nu_\tau}$$

where Γs are partial decay widths of the virtual W boson. The factor 3 comes from the color degrees of freedom.

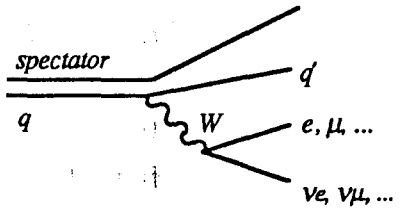

Figure 1.3 Diagram of weak charged current decay of heavy quark in the spectator model, where the spectator quark do not affect the decay.

2. Two-photon-exchange interaction

In searching for isolated e's, We cannot neglect $e^+e^-q\bar{q}$ productions via two-photon-exchange process. In α^4-order QED, $e^+e^-q\bar{q}$ production has four kinds of diagrams as shown in figure 1.4. They are called "multiperipheral", "bremsstrahlung", "conversion", and "annihilation". Most of the scattered e's escape toward the beam-pipe, which comes from the multiperipheral and the bremsstrahlung diagrams. The most dominant one, the multiperipheral diagram, gives Qf^4 dependence to the cross section.

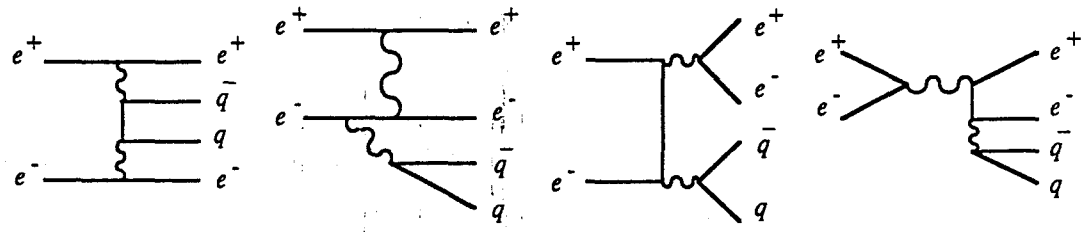

Figure 1.4 Diagrams of $e^+e^-q\bar{q}$ production, (a) multiperipheral, (b) bremsstrahlung, (c) conversion, and (d) annihilation.

1.4.2. New heavy particles decaying into electron

We summarize here new particles which can be effectively searched for by means of e-inclusive final state.

1. Third-generation up-type quark t

The third generation up-type quark, "top" or t-quark, has been found neither in e^+e^- collisions,[9] nor in $p\bar{p}$ collisions.[10] The t-pair production has a comparably large

cross section amounting to a few tens of pb at TRISTAN energy ignoring the threshold effect. The produced t-quark will be immediately confined into a t-flavored hadron nearly at rest and will decay into a b-quark and a virtual W-boson, which will lead to a large multiplicity of final particles and to a spherical event shape to be discussed later.

So far, the lower limit on t-quark mass as $m_t > 44$ GeV/c^2 was obtained by UA1 $p\bar{p}$ colliding experiment at CERN. But, because there may be some ambiguities in QCD calculation for $p\bar{p}$ experiments, it is meaningful to examine by e^+e^- experiments. The results from TRISTAN was reported in the references,[11] where VENUS set the limit on t-quark mass as $m_t > 30.2$ GeV/c^2 by the analysis on multijet events.

2. Fourth-generation down-type quark b'

The existence of the fourth generation is not necessary but is not excluded by any reliable theory, either. The number of light neutrinos is related to Z^0 width which was measured at $p\bar{p}$ experiments,[12] and recently, also in e^+e^- collision on Z^0 pole at SLC and LEP.[13] All of them well agreed with three-generation model. The combined limit of neutrino counting experiments at e^+e^- colliders below Z^0 pole, PEP, PETRA, and TRISTAN, is not in favor for the fourth generation, too.[14] However, if the accompanying neutrino is heavy, there still remains a possibility of its existence. We denote the presumed fourth generation quark doublet as (t',b'). The down-type quark, b'-quark, will be produced with 1/4 cross section of the t-quark production in QED calculation. In searching for b'-quark, the b'-quark mass is assumed to be lighter than t-quark. This assumption is natural by considering the fact that the mass difference between an up-type quark and a down-type quark in a doublet becomes larger as the generation number increases. The decay of b' should be determined by the extended 4×4 K-M matrix, but the matrix elements are of course unknown. Because the decay into t is kinematically suppressed, the weak charged current decay into c is expected to dominate. Search for b'-quark can be possible with the same method as for t-quark.

UA1 excluded b'-quark with mass below 32 GeV/c^2 with 90 % confidence level, reinterpreting the result of t-quark search. In e^+e^- experiments, VENUS excluded b'-quark with mass below 28.2 GeV/c^2 by the analysis on multijet events.

3. Unstable heavy neutrino N

As was already described in the previous section, the number of light neutrinos was nearly determined to three. However, it is meaningful to make a direct search for the fourth neutrino N which should be massive. The fourth-generation charged lepton is naturally assumed to be heavier than N. If we assume N to be massive, there is no reason to think other lighter neutrinos are massless and we must consider the lepton mixing in the weak interaction just like the quark mixing represented by K-M matrix. Therefore, N decays into charged leptons lighter than N according to the lepton mixing matrix U;

$$\begin{pmatrix} \nu_e \\ \nu_\mu \\ \nu_\tau \\ \nu_L \end{pmatrix} = U \begin{pmatrix} \nu_1 \\ \nu_2 \\ \nu_3 \\ N \end{pmatrix} = \begin{pmatrix} U_{e\nu 1} & U_{e\nu 2} & U_{e\nu 3} & U_{eN} \\ U_{\mu\nu 1} & U_{\mu\nu 2} & U_{\mu\nu 3} & U_{\mu N} \\ U_{\tau\nu 1} & U_{\tau\nu 2} & U_{\tau\nu 3} & U_{\tau N} \\ U_{L\nu 1} & U_{L\nu 2} & U_{L\nu 3} & U_{LN} \end{pmatrix} \begin{pmatrix} \nu_1 \\ \nu_2 \\ \nu_3 \\ N \end{pmatrix}. \tag{1.7}$$

N can be pair-produced in e^+e^- collision and we already presented the cross section formula in equation (1.4) which can be applied to N, assuming that N is a Dirac neutrino. If N is produced and if $|U_{eN}|$ is not so small both in absolute value and in comparison with $|U_{\mu N}|$ or $|U_{\tau N}|$, the decay, $N \to e^- W^{+*}$ with subsequent decay of virtual W^{+*} to any weak doublet, must be seen. Neglecting all the masses of the known fermions, the life-time is calculated in analogy with the decay, $\mu^- \to \nu_\mu e^- \bar{\nu}_e$;

$$\tau_N = \frac{m_\mu^5}{m_N^5} \frac{B(W^{+*} \to \nu_e e^+)}{\sum_{l=e\mu\tau} |U_{lN}|^2} \tau_\mu \approx \frac{m_\mu^5}{m_N^5} \frac{1}{9} \frac{1}{\sum_{l=e\mu\tau} |U_{lN}|^2} \tau_\mu \tag{1.8}$$

where m's and τ's denote the masses and the life-times for μ and N. In searching for N, there is an ambiguity of the mixing angles which determines the branching ratios and the life-time.

Searches for a unstable heavy neutral lepton were performed at previous e^+e^- colliders.[15] Mark-II at PEP searched for N with a comparably long life-time which makes separated decay vertices in the detector at $\sqrt{s}$ = 29 GeV. They concluded that N with mean decay length of 1 to 20 cm in mass range 1 to 13 GeV/c^2 was ruled out. CELLO at PETRA searched for short-lived N by tagging light charged leptons from N decay and excluded in the mass range 3.1 to 18.0 GeV/c^2 for dominant N-e couping case and in the range 3.2 to 17.4 GeV/c^2 for dominant N-μ coupling case. AMY at TRISTAN also ruled out the existence in the range 8.2 to 26.5 GeV/c^2 for the N-e case and 7.8 to 28.1 GeV/c^2 for the N-μ case.[16]

4. Electron-type neutral heavy lepton E^0

In some extensions of the standard model, the fermion multiplets represented in (1.1) are extended to larger ones and new heavy leptons and quarks are introduced to each multiplets. Electron-type neutral heavy lepton E^0 is one of such new leptons which weakly couples to e^-. Among so many theoretical models, here we introduce the so-called 2-2 model.[17] In this model again with SU(2)×U(1) symmetry, both left-handed and right-handed leptons form SU(2) doublets in a generation;

$$\psi_L = \begin{pmatrix} \nu_e \\ e^- \end{pmatrix}_L, \qquad \psi_R = \begin{pmatrix} E^0 \\ e^- \end{pmatrix}_R, \tag{1.9}$$

along with a left-handed singlet $E^0{}_L$. The Higgs field is again a complex doublet as in the minimal electroweak model. Though there arise a mixing of $E^0{}_L$ with ν_e, the mixing

is estimated to be of the order of m_e/m_E which is small enough to be neglected. Thus, ν_e remains nearly massless also in this model.

If such a lepton exists, it will be produced in e^+e^- collision together with ν_e via the W exchange process as shown in figure 1.5. The coupling of the $e^-E^0W^+$ vertex is model-dependent. The most likely coupling structure is full V+A (right-handed, R) type as in the 2-2 model. But in general, V–A (left-handed, L) type should be also considered. The cross section for the reaction, $e^+e^-\rightarrow\bar{\nu}_eE^0$ is given for the V–A and the V+A cases as follows;[18]

$$\frac{d\sigma_L}{d\cos\theta}=\frac{G_F^2}{16\pi}\left(1-\frac{m_E^2}{s}\right)^2\left(1-\frac{t}{m_W^2}\right)^{-2}\left[2s(1+\cos\theta)-(s-m_E^2)\sin^2\theta\right], \tag{1.10}$$

$$\frac{d\sigma_R}{d\cos\theta}=\frac{G_F^2}{16\pi}\left(1-\frac{m_E^2}{s}\right)^2\left(1-\frac{t}{m_W^2}\right)^{-2}4s, \tag{1.11}$$

$$\text{with } t=-(s-m_E^2)(1-\cos\theta)/2,$$

where θ and m_E are the polar angle and the mass of E^0. Of course, there also exists the charge conjugated process, $e^+e^-\rightarrow\bar{E}^0\nu_e$. The heavy E^0 will be unstable because the lifetime is given in both cases by;

$$\tau_E=\frac{m_\mu^5}{m_E^5}\tau_\mu B(E^0\rightarrow e^-\nu_e e^+)\approx\frac{m_\mu^5}{m_E^5}\frac{\tau_\mu}{9} \tag{1.12}$$

$$\approx 10^{-17}\text{ seconds for } m_E=10\text{ GeV}/c^2.$$

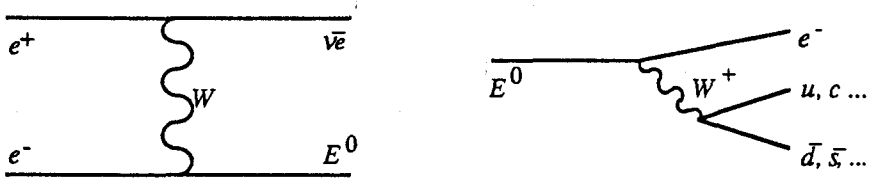

Figure 1.5 Diagrams of production and decay of electron-type neutral lepton.

Searches for E^0 were made at the prior e^+e^- experiments as well as for N in the previous subsection. Mark-I at SPEAR excluded E^0 with mass less than 1.2 GeV/c^2, and CELLO excluded E^0 in the mass range 0.6 to 34.6 GeV/c^2 (V–A) and 0.4 to 37.4 GeV/c^2 (V+A). It is noted that E^0 can be searched for with mass up to $\sqrt{s}$ in principle and that there is no advantage in on-Z^0-pole experiments at SLC/LEP because of large backgrounds from known quark production.

5. First-generation leptoquark χ

Leptoquarks, which couple to a lepton and a quark possessing both a color charge and a lepton number, appear naturally in such models unifying leptons and quarks as technicolor,[19] composite models,[20] grand unified theories,[21] and superstring theories.[22] For example, in the model by Schrempp and Schrempp according to the framework of nearby compositeness and special technicolor schemes, leptoquarks

appear as colored pseudo-Goldstone boson multiplets of charge $Q = 2/3$, one per generation. In the minimal superstring inspired model, $Q = -1/3$ leptoquarks are expected. The general specifications of leptoquarks are summarized in the references.[23] Most of these models were proposed, inspired by the "CELLO event" which has two isolated μ's and two jets,[24] and most of the arguments are valid also at TRISTAN energy.

Here we consider a scalar color triplet leptoquark χ which couples to the first-generation leptons and quarks. The two kinds of specifications on χ are summarized in table 1.2.

electric charge	−1/3	2/3
available decay mode	e^-u, $\nu_e d$	e^+d, $\bar{\nu}_e u$

Table 1.2 Two kinds of specifications on the first-generation leptoquark.

As shown in figure 1.6, χ can be produced in $e^+e^- \to \chi\bar{\chi}$ reaction. Only for the first generation leptoquark, there exists a quark-exchange process besides the γ-annihilation process. From the view point of QCD, a leptoquark behaves as a quark. The produced leptoquark must be immediately confined into a color singlet system, that is, a bound state with a light quark, which decays into a lepton and a quark along the spectator quark as shown in figure 1.6.

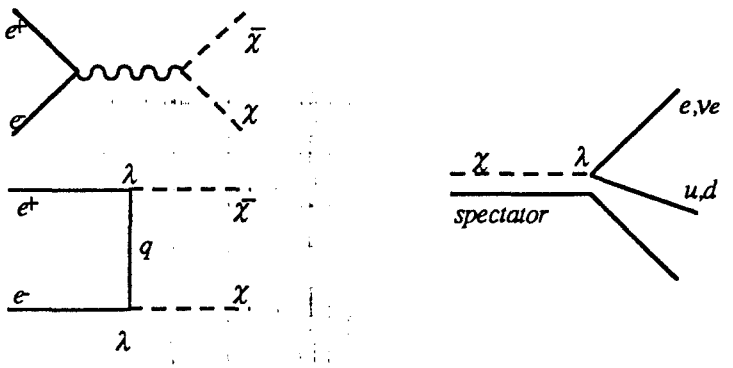

Figure 1.6 Diagrams of production and decay of the first-generation leptoquark, where exist two production diagrams of γ-annihilation and quark-exchange.

Ignoring the undefined weak coupling, the cross section is given as follows;

$$\frac{d\sigma}{d\cos\theta} = \frac{3\pi\alpha^2}{4s}\beta^3\sin^2\theta \left[Q^2 + \frac{|Q|}{1+\beta^2-2\beta\cos\theta}\frac{\lambda_e^2}{e^2} + \frac{1}{4(1+\beta^2-2\beta\cos\theta)^2}\frac{\lambda_e^4}{e^4}\right], \quad (1.13)$$

where, θ is the the polar angle of either χ or $\bar{\chi}$, which couples to e^-. The strength of e-q-χ coupling is determined by λ_e^2 which should be constrained by low energy reactions.

For example, the total hadronic cross section in e^+e^- collision might be affected by χ-exchange process as shown in figure 1.7. Since no anomaly was reported so far, the coupling strength λ_e^2 must be small. Thus, we neglect the second and the third term in equation (1.13) which always enhance the cross section of $e^+e^- \rightarrow \chi\bar{\chi}$ reaction.

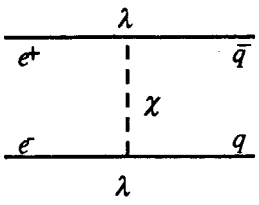

Figure 1.7
Leptoquark-exchange diagram in quark-pair production

A scalar leptoquark is expected to decay into a lepton and a quark isotropically. The partial decay widths are given by;

$$\Gamma(\chi \rightarrow eq) = \frac{\lambda_e^2 m_\chi}{16\pi}, \qquad \Gamma(\chi \rightarrow \nu_e q) = \frac{\lambda_\nu^2 m_\chi}{16\pi}, \tag{1.14}$$

where λ_ν^2 is a strength of ν_e-q-χ coupling. The branching ratio of the decay into e is determined by $\lambda_e^2/(\lambda_\nu^2+\lambda_e^2)$.

There is no publication papers on the first-generation leptoquark but on the second-generation one only,[25] inspired by the CELLO event.

1.5. Outline of the thesis

In chapter 1, we have reviewed the present theory of particle physics and historical contributions of e^+e^- colliding experiments. We also introduced theoretical and experimental background in finding new particles in our consideration. In chapter 2, the apparatus of the accelerator TRISTAN and VENUS detector are presented. The techniques of data reduction and event reconstruction from the detector signals are described in chapter 3. The method and the performance of electron identification are described in chapter 4. The analysis of the search for new particles with electron-inclusive final state is described in chapter 5. The results of the analysis is summarized in chapter 6. Some tools and preparations are given in the appendices. The techniques of Monte Carlo simulation are described in appendix A. The methods of radiative correction which were included in the simulation are described in appendix B. The calorimeter responses for hadrons were parametrized and implemented into the detector simulation program as described in appendix C. In order to evaluate the identification efficiency of e, e sample was collected as described in appendix D.

Chapter 2 Experimental Apparatus

2.1. TRISTAN

TRISTAN is an e^+e^- colliding beam facility at National Laboratory for High Energy Physics (KEK) in Tsukuba city, Japan.[26] It consists of a 400 m long linear accelerator (LINAC), an accumulation ring (AR) with circumference of 377 m, and a main ring (MR) with circumference of 3.0 km as shown in figure 2.1.

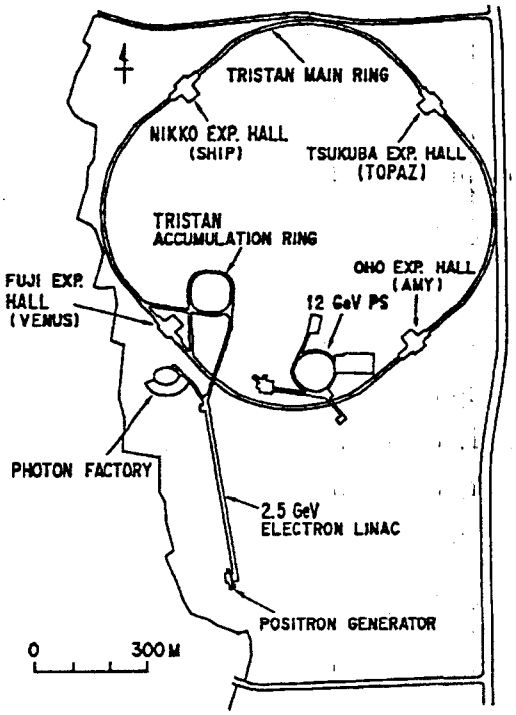

Figure 2.1
Site layout of TRISTAN at KEK.

TRISTAN began since November 1986. Since then, the beam energy and intensity have been improved steadily. The beam operation in MR has four stages, e^+-filling, e^--filling, acceleration, and storage. The e^+ beam is produced by bombarding a tantalum target with an e^- beam. The LINAC accelerates both the e^+ and e^- beams up to 2.5 GeV and injects them into AR. AR stores the beam up to 20 mA and accelerates the beam up to 8 GeV and injects them into MR. The injection is repeated until MR acquires enough intensity. MR accelerates the beams up to around 30 GeV. Two e^- bunches and two e^+ bunches, circulating in opposite directions, intersect with each other every 5.0 μs at the central points of four straight sections. A large portion of the straight section is allocated to RF cavities which accelerate the beams and compensate for enormous energy loss by synchrotron radiations. The operation with beam energy greater than 30 GeV became possible by installation of superconducting RF cavities in summer 1988. The beam life-time was typically three hours and the beams were dumped and refilled about every two hours. The peak luminosity was 10^{31} $cm^{-2}\cdot s^{-1}$ and the integrated luminosity per day was up to 300 nb^{-1}. Four experimental halls, named Fuji, Oho, Tsukuba, and Nikko, were constructed at the colliding points. VENUS detector is located in Fuji hall.

2.2. VENUS detector

2.2.1. General description

VENUS is a general purpose detector for e^+e^- collision physics.[27] The main feature is high resolution measurement of both charged particle momentum and electromagnetic shower energy with wide solid angle coverage. VENUS was first operated in November 1986 with $\sqrt{s} = 48$ GeV and accumulated data with $\sqrt{s} = 50$ and 52 GeV. It was upgraded by the installation of the end-cap calorimeters and the muon detector during the summer shutdown in 1987. This analysis is based on the data which have been taken after the end-cap calorimeters began to work. A side view of VENUS is shown in figure 2.2.

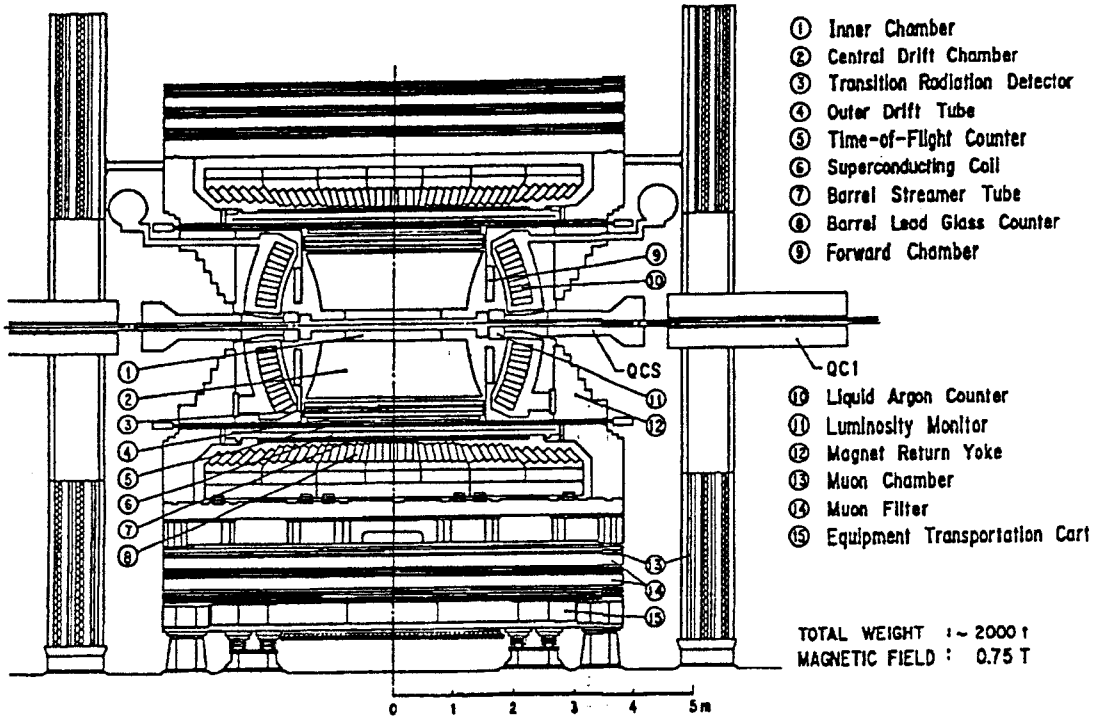

Figure 2.2 Side view of VENUS detector, where Forward Chamber and Transition Radiation Detector had not yet been installed in the data taking period of this analysis.

The coordinate system for the analysis was defined as shown in figure 2.3, where the origin is set at the colliding point, x axis directs horizontally outward from the center of MR, y axis directs vertically upward, and z axis is the direction of the e^- beam at the origin. Since most of the detector components have axial symmetry around z axis, cylindrical coordinate with radius defined by the distance from z axis is also used to describe the geometry of the detector. In the analysis, polar coordinate is mainly

used, where polar angle θ is defined with respect to z axis, and azimuthal angle ϕ is measured counterclockwise from x axis in x-y (r-ϕ) plane.

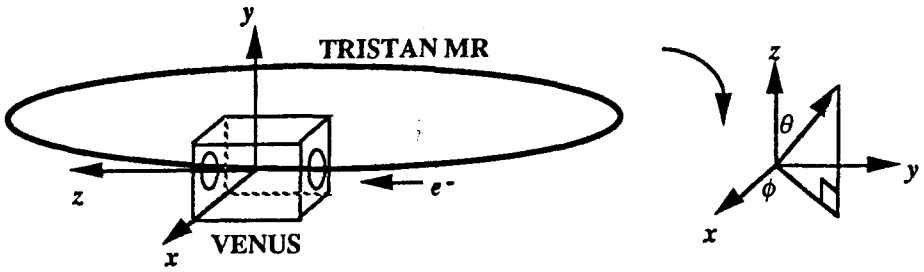

Figure 2.3 Definition of the coordinate system.

2.2.2. Beam-pipe

The vacuum beam-line around the colliding point is shielded by an aluminium beam-pipe with a radius of 9 cm and with a length of 270 cm. The thickness is 2.5 mm for $|z| < 25$ cm and 5 mm otherwise.

2.2.3. Inner Chamber

The inner chamber (IC) is a cylindrical multiwire drift chamber located outside the beam-pipe.[28] The inner radius, the outer radius, and the length are 10 cm, 24 cm, and 160 cm, respectively. Figure 2.4 shows the structure of IC. The 6 layers of anode wires give information of charged tracks in r-ϕ plane. Each of the 6 cathode layers is divided into 16 (θ) × 8 (ϕ) = 128 elements, on each of which a cathode pad of 18 μm-copper sheet is attached. The cathode pads are arranged in tower-geometry, that is, the total 128 towers, each consisting of the 6 layers of the pads, are pointing at the colliding point. Three-dimensional informations from the pads are used for the first level trigger. Charged particles which did not come from the beam-beam interactions, namely the beam-associated backgrounds, are mostly suppressed by the requirement of the hit pattern pointing to the colliding point.

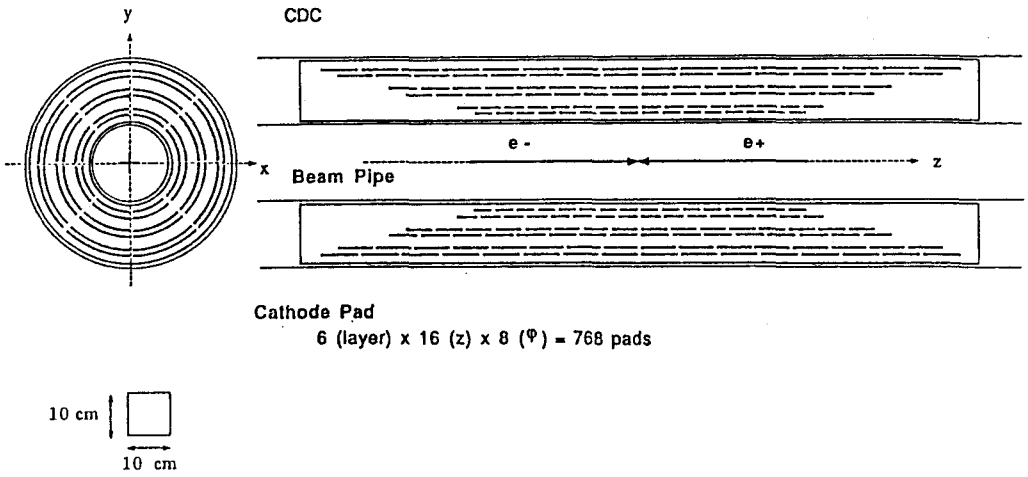

Figure 2.4 Layout of the cathode pads of the inner chamber (IC).

2.2.4. Central Drift Chamber

The central drift chamber (CDC) is a main tracking detector which measures the momenta of charged particles.[29] The chamber has an inner radius of 25 cm , an outer radius of 126 cm, and a length of 300 cm, where HRS gas, the mixture of $Ar/CO_2/CH_4$ (90:9:1), is filled with. CDC has 7104 sense wires and 21312 field wires. The end-view and the cell-structure are shown in figure 2.5. 20 layers of axial wires are strung parallel to z axis and 9 layers of slant wires are tilted by ±3.3° in ϕ direction from z axis. Two axial layers are arranged always adjacent each other, staggered by half a cell in order to resolve the left/right ambiguity of the drift direction. The axial wires are used for the tracking in r-ϕ plane and the slant wires are for z reconstruction. The total 29 layers cover a angular region of $|\cos\theta| < 0.75$. The drift-time is measured by a time to digital convertor (TDC) system and is converted to the position information of the trajectory. The spatial resolution in the chamber was measured to be 270 μm.

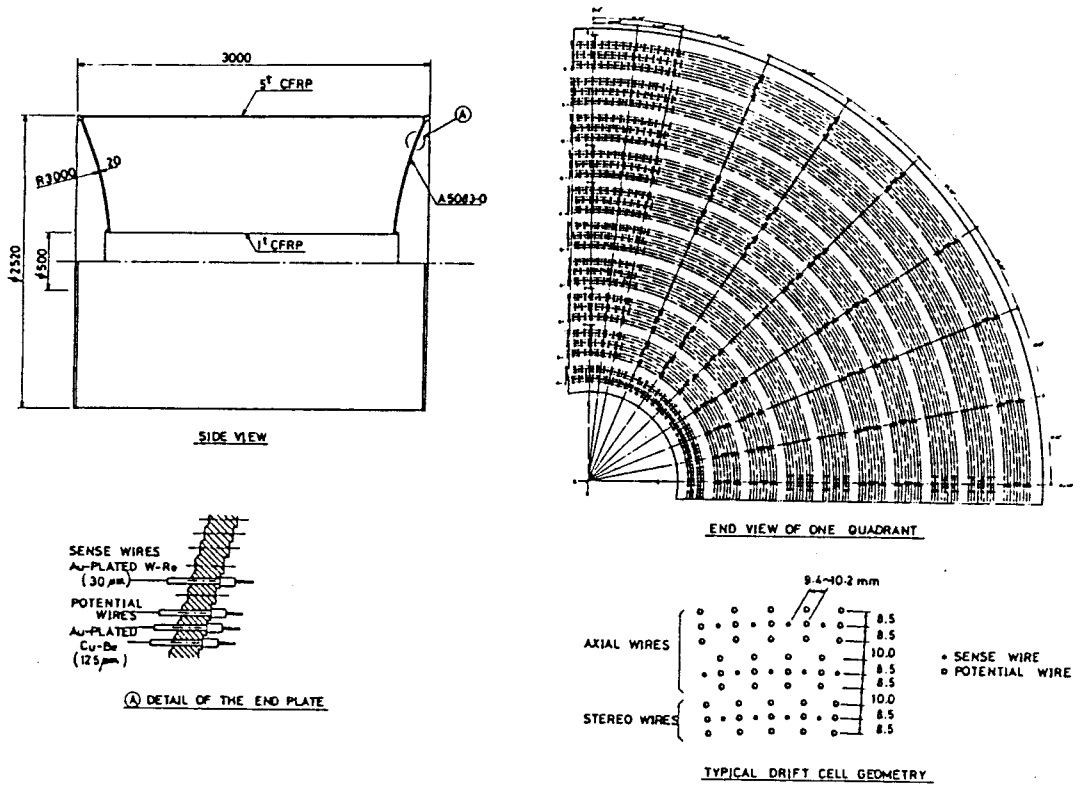

Figure 2.5 End-view of one quadrant and typical drift cell geometry of the central drift chamber (CDC).

2.2.5. Outer Drift Tubes

The outer drift tube system (ODT) consists of staggered 3 layers of cylindrical drift tubes which have a length of 284.4 cm and are placed cylindrically at radius between 157 cm and 162 cm. ODT covers a region of $|\cos\theta| < 0.66$ and the accuracy of the momentum measurement for a charged particle can be improved with a help of ODT.

2.2.6. Time-of-Flight Counters

The time-of-flight counter system (TOF) consists of 96 scintillation counters with a rectangular cross section of 10.7 cm × 4.2 cm and a length of 466 cm.[30] They are arranged in parallel to z axis cylindrically at inner radius of 164 cm. Phototubes are attached to both sides of each counter through light-guides of 145 cm long. TOF covers $|\cos\theta| < 0.81$. The time resolution was checked by Bhabha events to be 200 ps. From

the time difference between the both sides of the counter, z position can be measured with resolution of 5 cm.

2.2.7. Superconducting Magnet

For momentum measurement, a uniform magnetic field of 7500 gauss is produced in parallel to z axis by a superconducting solenoidal coil.[31] It is 520 cm in length, 170 cm in inner radius, and 20 cm in thickness which corresponds to 0.64 radiation lengths. The magnetic field is uniform within 0.3 % deviation over the whole volume of CDC.

2.2.8. Barrel Streamer Tubes

The barrel streamer tube system (BST) consists of two staggered layers of conductive plastic tubes cylindrically arranged outside the magnet.[32] Each tube has a rectangular cross section of 1.9 cm $\times$ 1.35 cm and a length of 444 cm. The total 1200 tubes are grouped into 16 modules. At the center of the tube, an anode wire is strung. Copper cathode strips are attached onto the inner and the outer side of the module. The inner strips are arranged perpendicular to z axis and outer ones are inclined by 45° to them. BST is operated in the limited streamer mode, where the pulse height is large enough not to require considerable amplification for read-out. BST gives informations on hit positions of charged particles and converted γ's which inject into the barrel calorimeter.

2.2.9. Barrel Lead-Glass Calorimeter

Electromagnetic calorimeter measures energies and incident positions for e and γ. The barrel lead-glass electromagnetic calorimeter (LG) has a cylindrical shape with a radius of 2 m and a length of 6 m.[33] The structure of LG is shown in figure 2.6. There are 43 rings along z axis each of which has 120 counter modules. The total 5160 modules are arranged in a semitower-geometry, approximately pointing to the colliding point. They are tilted by 3° in ϕ-direction and by typically 7° in θ-direction so as not to miss particles through the counter gaps, typically 1.5 mm. The calorimeter covers a region of $|\cos\theta| < 0.79$. The structure of the counter module is shown in figure 2.7. It consists of a lead-glass block, a plastic light-guide, and a phototube which detects the Cerenkov light emitted by charged particles in the counter. An electromagnetic shower induced by e or γ is well contained in the lead-glass for the energy up to more than 30 GeV. Electromagnetic shower is a multiplication of e's and γ's by the cascade process of pair-conversion ($\gamma \rightarrow e^+e^-$) and bremsstrahlung ($e \rightarrow e\gamma$) in material. The shower constituent becomes lower in energy by the multiplication and stops by energy losses. The integrated electric charge from the phototube is interpreted as the energy deposit in the counter.

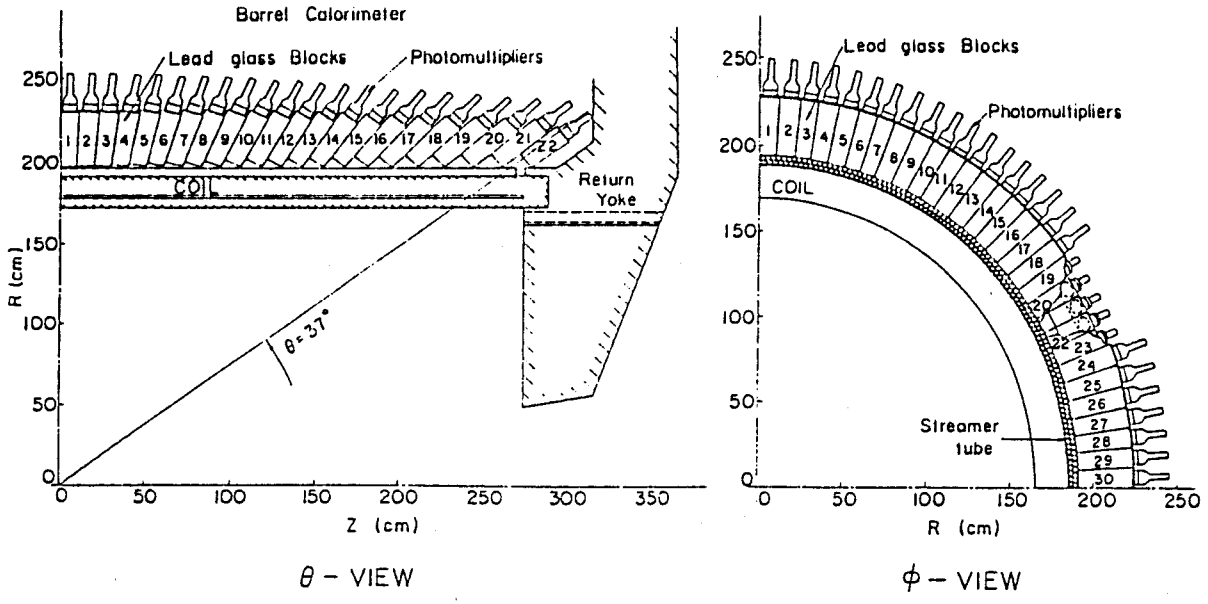

Figure 2.6 Structure of the barrel lead-glass calorimeter (LG).

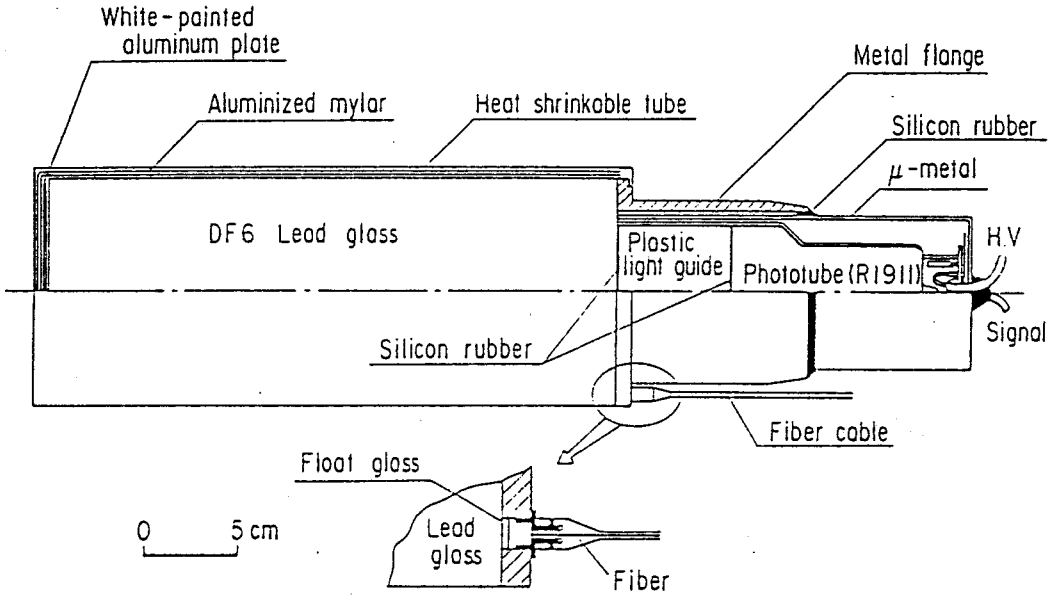

Figure 2.7 Structure of the lead-glass counter module.

The lead-glass block is 30 cm in depth corresponding to 18 radiation lengths or 1 nuclear interaction length and the typical cross section is 12 cm × 11.6 cm at the front face.[34] The main ingredients of the material of the lead-glass, DF6, are PbO (70.9 %) and SiO_2 (27.3 %). The density is 5.18 g/cm^3, the radiation length is 1.68 cm, and the refractive index is 1.805. The critical energy is 12.6 MeV, below which the ionization energy loss dominates the energy loss by bremsstrahlung.

A plastic light-guide of 6 cm long is inserted so as to keep the phototube away from the leakage magnetic field, extending the magnetic shield of μ-metal which surrounds the phototube and the light-guide.

Two different types of 3-inch phototubes, Hamamatsu R1911 and R1652 are used.[35] The box-and-grid type phototubes (R1911) cover the central 31 rings with a little better resolution. For the peripheral 6 rings of each side where the leakage field is up to 30 gauss, the mesh type phototubes (R1652) are used.

In order to monitor the gain fluctuation of the phototubes, two independent xenon flash lamps provide the light to each lead-glass module through optical fibers. During the running time, the monitoring system was operated usually once a week utilizing the beam-filling time. More than 95 % of all the modules were stable within 2 % in pulse height. The relative fluctuations were calibrated by this system and the overall normalization factor was adjusted by monochromatic electrons in Bhabha events. The energy resolution for e was measured by Bhabha events to be 3.8 % at 28 GeV.

2.2.10. End-cap Liquid-Argon Calorimeters

Two end-cap liquid-argon electromagnetic calorimeters (LA's) are located between CDC and both end-caps, covering $0.80 < |\cos\theta| < 0.99$.[36] LA has 480 towers consisting of 70 lead-plates with 1.5 mm thickness and with 3 mm spacing dipped in liquid-argon. Figure 2.8 shows the structure of the liquid-argon calorimeter. The tower depth corresponds to 20.3 radiation lengths. All the towers are pointing 80 cm beyond the colliding point. The 70 lead-plates in the tower are held at +3.0 kV or 0.0 kV alternately and grouped into four read-out channels to record longitudinal shower developments. The electrons from the ionizations by charged particles in liquid-argon are collected at the anode plates and the deposited energy is measured. The energy resolution for e is measured by Bhabha events to be 3.5 % at 28 GeV.

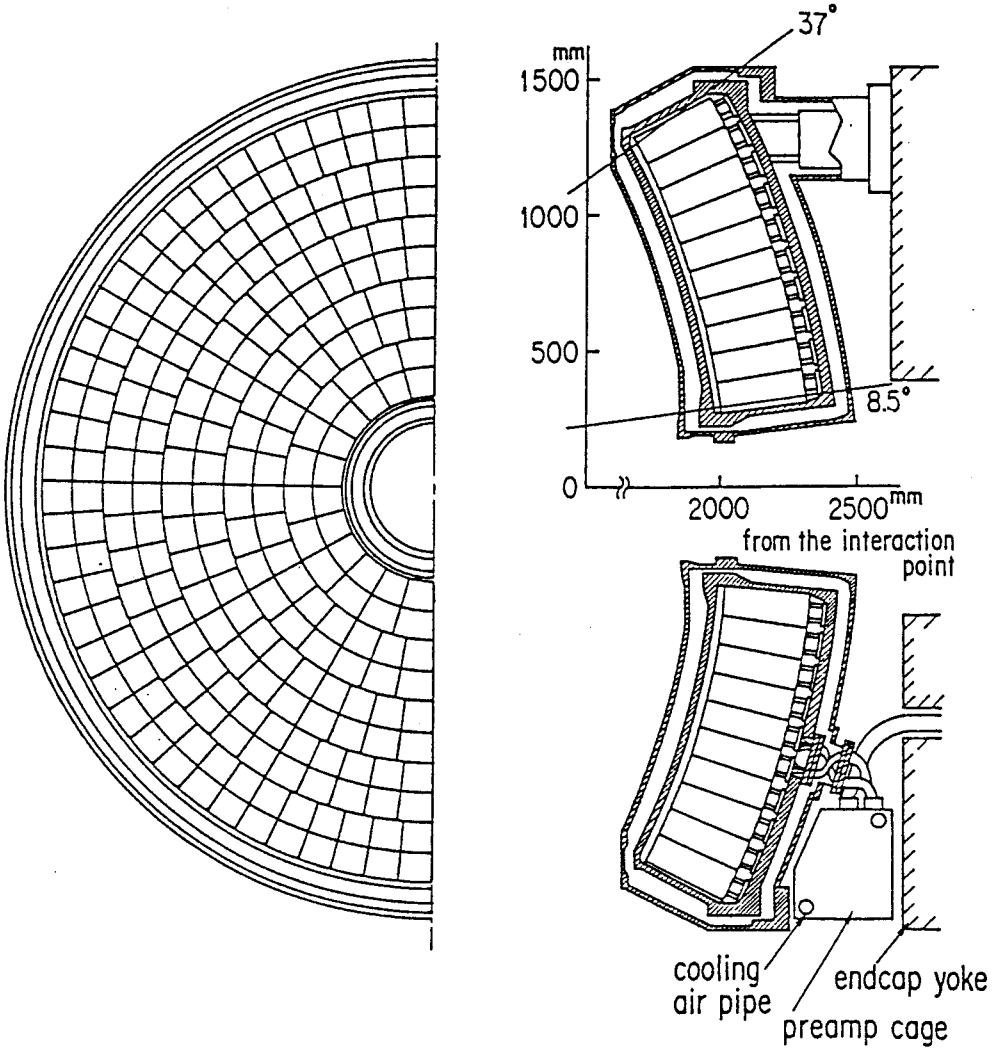

Figure 2.8 Structure of the end-cap liquid-argon calorimeter (LA).

2.2.11. Muon Detector

The muon detector (MU), which is placed outside the return yoke, consists of a barrel part and forward/backward parts of drift tubes sandwiched between thick iron absorbers.[37] The barrel part has 8 layers of the tubes, covering $|\cos\theta| < 0.69$ and 90 % in ϕ. The tubes of inner 6 layers are parallel to z axis and ones of outer 2 layers are perpendicular to them. The forward/backward part has 4 layers of drift tubes covering $0.69 < |\cos\theta| < 0.93$. The total material, before a particle encounters the fifth layer of the barrel part, amounts to at least 5.3 absorption lengths. It was checked by cosmic-rays that μ with momentum above 2.0 GeV/c penetrates all the absorbers, while hadrons are expected to be absorbed with a probability about 99.5 %.

2.2.12. Luminosity Monitor

A pair of electromagnetic shower counters, the luminosity monitoring counters (LM's), is installed to detect small angle Bhabha scattering. Each counter is located

between the beam-pipe and LA and consists of 8 sectors which are made of 27 plastic scintillators sandwiched between 27 lead-plates, covering $0.985 < |\cos\theta| < 0.997$. In this angular region, the cross section of Bhabha scattering is very large and luminosity can be measured with very small statistical error. Therefore, this system is useful to monitor short-term variations of luminosity.

2.3. Data acquisition

2.3.1. Trigger system

The trigger system provides flexible trigger-signals, which are efficient for most of e^+e^- reactions.[38] The first-level decision must be carried out quickly before the next beam-crossing, which means every 5 μs. The trigger conditions were optimized to have sufficient efficiencies for the physics reactions of significance and enough reduction rate of the backgrounds. Several kinds of triggers were implemented according to the expected event signatures as follows:

(1) Two-track trigger
There exist at least two tracks from the origin with $p_t > 0.7$ GeV/c, $|\cos\theta| < 0.81$ corresponding to the coverage of TOF, and with their opening angle larger than 120° in r-ϕ plane, where p_t is the transverse momentum to z axis.

(2) LG total sum trigger
The total detected energy in LG is more than 4 GeV.

(3) LA total sum trigger
The total detected energy in either side of LA is more than 5 GeV.

(4) LM Bhabha trigger
There exists at least one pair of back-to-back hits with energy more than 10 GeV at LM sectors. LM is divided into 8 sectors.

(5) LA sector sum trigger
There exists at least one LA sector hit with energy more than 2 GeV. LA is divided into 48 sectors.

(6) LG segment × two-track trigger
There exist at least one LG segment hit with energy more than 0.7 GeV and at least two tracks with $p_t > 0.7$ GeV/c. LG is divided into 58 segments.

It is noted that most of the triggered events were backgrounds, namely interactions between the beam and the beam-pipe or the remaining gas, cosmic-rays, or other noises. Therefore, the trigger rate depended on the beam conditions. The minimum opening angle of two tracks for the two-track trigger had been limited to 170° till July

1988. The track trigger was produced by a fast pattern recognition of signals from IC, CDC, and TOF using a track-finder electronics with RAM (random access memory) look-up-table. The energy triggers were produced by discriminating analogue-sum signals of the counter outputs. The LG segment × two-track trigger was produced by LG signals and CDC track finder outputs. The block-diagram is shown in figure 2.9. The second level reduction system using the online-processor module, 68K20FPI,[39] was implemented in June, 1989. It dose more precise evaluation in track-finding only for track-triggered events and reduced about a half of them with dead-time of about 5 ms.

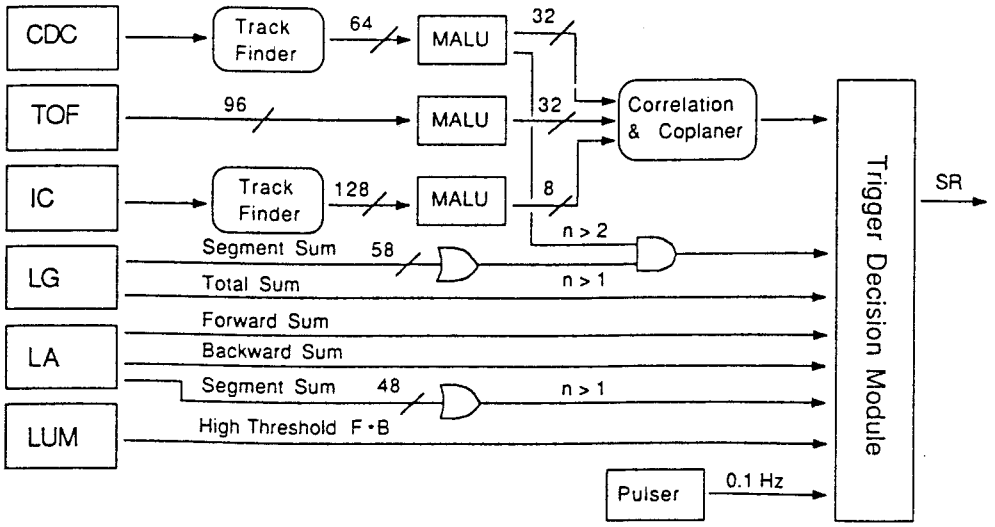

Figure 2.9 Block-diagram of the trigger system, where MALU (Majority Logic Unit) counts the multiplicity of hits.

These various trigger signals are complementary and make nearly no bias on the selection of multihadronic events. The efficiencies of these triggers were checked against each other by offline analysis. For example, figure 2.10 shows the efficiency of LG total sum trigger and the the segment hit efficiency with respect to the measured total energy in LG and to the segment energy, respectively.

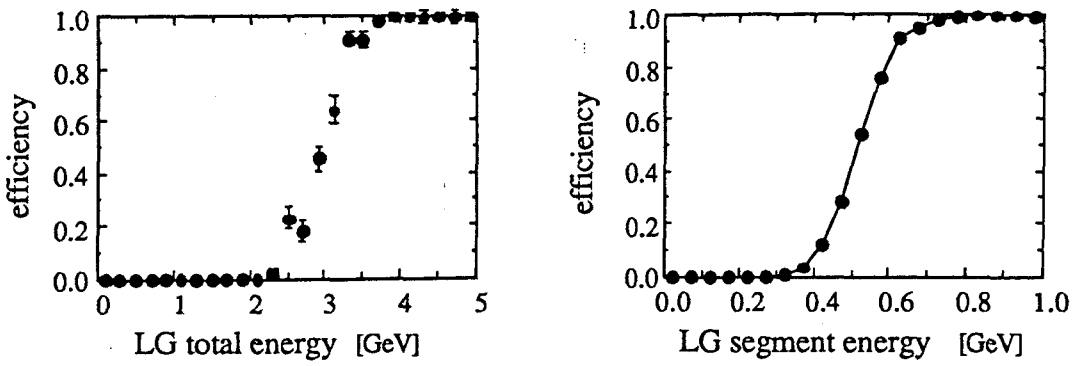

Figure 2.10 Efficiency of LG total sum trigger and that of the segment hit.

2.3.2. Data acquisition system

The data acquisition system has a tree-like structure as shown in figure 2.11,[40] where more than 30000 channels of read-out electronics exist. In order to deal with such vast data efficiently, FASTBUS, CAMAC, and TKO[41] systems are used. The data are collected at the VAX11/780–VAX8530 mini-computer cluster and sent to main computer FACOM M382 (replaced by M780 in March 1988) and stored in magnetic tapes there. Typical data size was 8 kbyte per event and the dead-time for read-out was 25 ms per event.

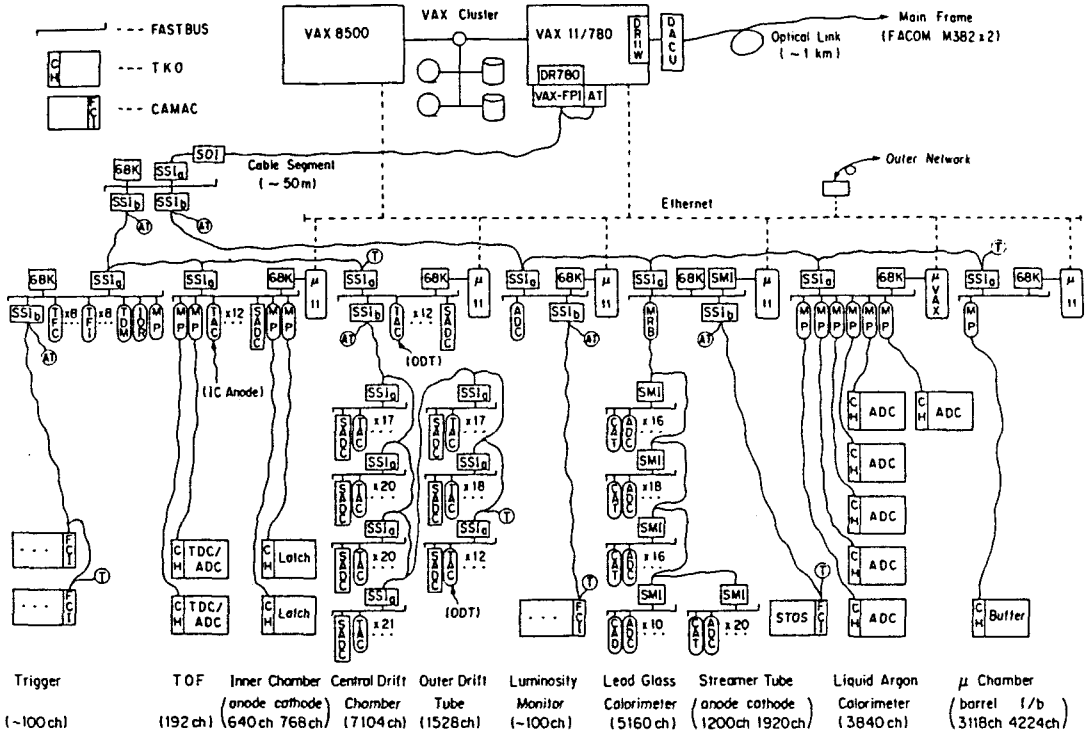

Figure 2.11 Block-diagram of the data acquisition system. Abbreviated module names are as follows; 68K – 68000 FASTBUS processor interface, ADC(FASTBUS) – 96 ch ADC, ADC(TKO) – 32 ch ADC, CAT – calibration and trigger module, CH – control head, FCI – FASTBUS-CAMAC interface, IOR – input/output register, MAL – majority logic, MP – memory partner, MRB – multirecord buffer, SADC – scanning ADC, SMI – segment manager/interface, SOI – segment optical isolator, SSI – simplex segment interconnect, STOS – streamer tube operating system, TAC – 64 ch time-to-amplitude converter, TDC – 16 ch time-to-digital converter, TFC – track finder for CDC, TFI – track finder for IC, TDM – trigger decision module, (A)T – cable segment (active) terminator.

2.4. Luminosity measurement and integrated luminosity

Luminosity L represents the rate of e^+e^- collision and is related to a number of events N through,

$$N = \sigma \int L \, dt \,, \tag{2.1}$$

where σ is cross section for a given reaction. Luminosity is originally defined by,

$$L = \frac{I_{e^+} I_{e^-}}{4\pi f_{rev} \, n_b \, e^2 \sigma_x \sigma_y}, \qquad [\mathrm{cm^{-2}s^{-1}}] \tag{2.2}$$

where I_{e+} and I_{e-} are the beam currents, e is the magnitude of e^+ charge, f_{rev} is beam revolution frequency, n_b is number of bunches per beam, and σ_x and σ_y are horizontal and vertical beam sizes at the colliding point. However, because the precise measurement of σ_x and σ_y is very difficult, the integrated luminosity is usually measured using equation (2.1) inversely for a well-known reaction with large cross section. Bhabha scattering,*i.e.* $e^+e^- \rightarrow e^+e^-$ reaction, was used to measure luminosity in this experiment. Figure 2.12 shows the development of center of mass energies and the daily integrated luminosity used in this thesis.

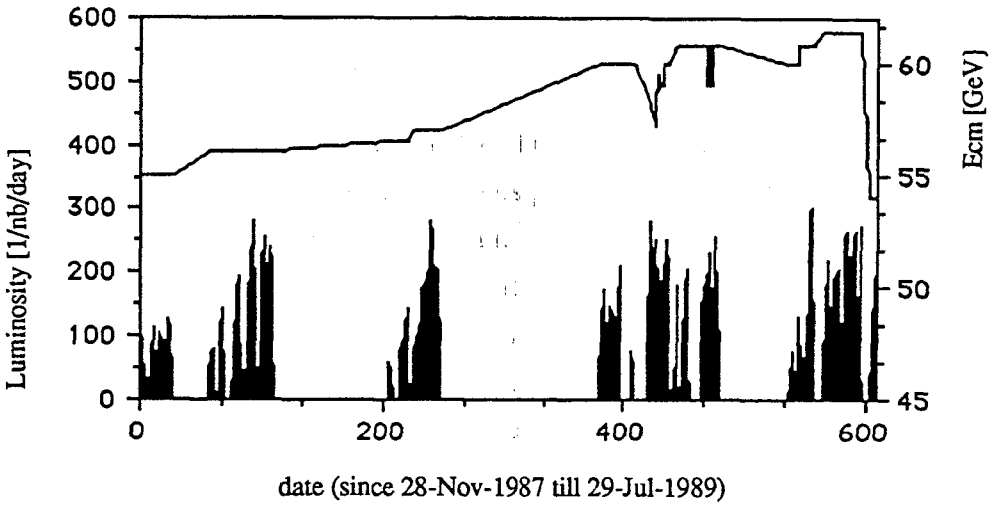

Figure 2.12 Integrated Luminosity per day (black histogram) and center of mass energy (solid line) since 28-Nov-1987 till 29-Jul-1989 corresponding to the data-taking period of this analysis.

Chapter 3 Reconstruction and Reduction of Data

3.1. Overview

In order to make a physics analysis, kinematical informations must be reconstructed from the detector signals. For example, a charged particle leaves discrete hit points along the trajectory in CDC and a particle injected into LG or LA leaves energy deposits over several modules which should be grouped into a cluster. Track-reconstruction from CDC hits and cluster-reconstruction from LG or LA hits are foremost steps of event-reconstruction. In any analysis, a specific selection must be carried out beforehand according to expected signature of the reaction to be studied. Because there are too many unwanted events in the taken data, the data reduction, which makes specific data sample, must be accomplished.

3.2. Event reconstruction

3.2.1. Track reconstruction

In order to recognize charged particles and to measure their momentum, the trajectory of the particle must be drawn from the discrete hit points of CDC. First, two-dimensional tracks in r-ϕ plane are reconstructed, where only the axial wire hits are used. The trajectory in r-ϕ plane is expected to be an arc in the uniform magnetic field, neglecting energy loss and multiple scattering. A two-dimensional track is obtained by fitting the hit points to a semicircle, where at least 6 hit points must exist within the allowable deviation from the trajectory. From the curvature, the transverse momentum with respect to the beam axis, p_t, is obtained. The associated hits in the slant layers are surveyed along the two-dimensional track. They can be seen as in figure 3.1 at the endplate of CDC. The z coordinate for a slant wire hit is given by the formula;

$$z = \frac{l}{2} - \frac{d}{\tan\alpha}, \tag{3.1}$$

where l is the length of the slant layer, d is a distance between the axial trajectory and the slant hit position at the $+z$ side end-plate of CDC, and α is the slant angle, either $+3.3°$ or $-3.3°$. The trajectory is expressed as a straight line in s-z plane, where s is the distance along the trajectory. By linear-fitting, the three-dimensional track is obtained if at least 3 slant wire hits are accepted. The starting point of the track is defined by the position which minimizes R_{min}, the distance to the origin in r-ϕ plane, where the z coordinate is called Z_{min}, as shown in figure 3.2. The detailed description of the tracking can be found elsewhere.[42]

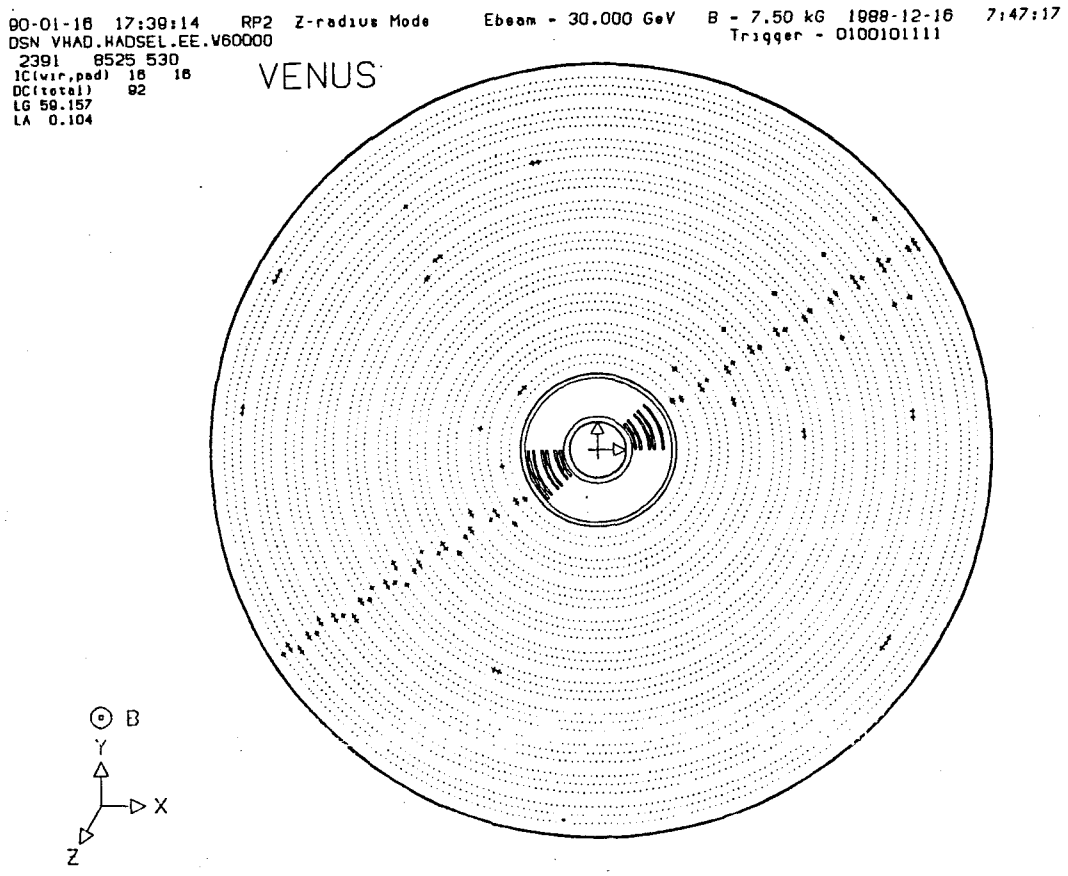

Figure 3.1 Example of a track and its associated hit wires at the end-plate of CDC for Bhabha event in r-ϕ view. There are three lines of hit wires belong to +3.3° slant layers, axial layers, and –3.3° slant layers. The right-side particle went away from this end-plate and the left-side one approached toward it.

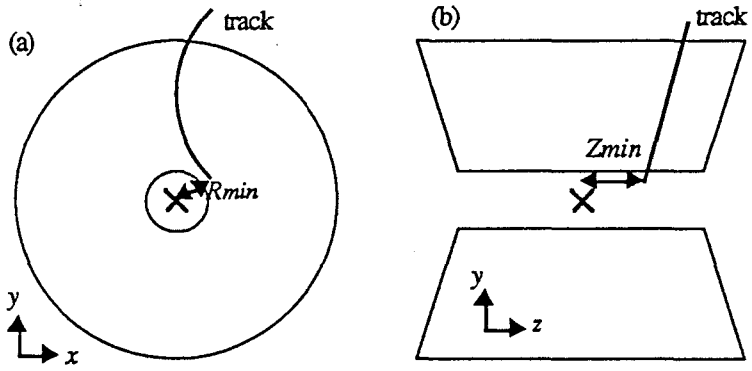

Figure 3.2 Definitions of R_{min} and Z_{min}. in (a) x-y view and (b) y-z view, where CDC is schematically drawn and the origin (colliding point) is indicated by a cross.

The efficiency of three-dimensional reconstruction was estimated by Monte Carlo simulation to be 92 % for charged particles with $|\cos\theta| < 0.766$ and with $p_t >$

0.15 GeV/c in multihadronic events. The momentum resolution σ_p in 7.5 kG magnetic field was measured by using real data and is represented as follows;

$$\frac{\sigma_p}{p} = \sqrt{(0.008p_t)^2+0.013^2}, \tag{3.2}$$

with p_t in GeV/c. The position and the angular resolutions near the colliding point for comparably high p_t tracks were found to be;

$$\sigma_{xy} = 500\ [\mu\text{m}], \qquad \sigma_z = 8\ [\text{mm}],$$
$$\sigma_\phi = 1.3\ [\text{mrad}], \qquad \sigma_\theta = 9\ \sin^2\theta\ [\text{mrad}]. \tag{3.3}$$

3.2.2. Cluster reconstruction

A particle injected into LG or LA usually leaves energy deposit over some neighboring modules. Such modules should be grouped into a "cluster", which is a group of modules intended to correspond to a single particle. Here, the definition and property of LG cluster are described briefly.

Each module in a cluster must adjoin to others side by side. Basically, an outer module from the most energetic module must have a smaller energy deposit than the adjoining inner modules in θ and ϕ directions. However, considering the energy fluctuations, we made an exception where a module is included with only one adjoining module with larger energy. The exception is applied for a module with energy less than 0.1 GeV in order to recover fluctuations in low energy. The exception is also applied for a module if it is next to an energetic module with 30 % of the cluster energy which may be a true central module.

Two examples of the reconstructed clusters are shown in figure 3.3, where in (a) a clean cluster made by a 30 GeV e is seen and in (b) a more complicated pattern was produced by hadrons and γ's in a hadronic jet. An electromagnetic shower is strongly collimated and nearly always result in a single cluster with a characteristic pattern of the energy-sharing among the modules according to the incident position. Thus the incident position of e and γ can be measured with a good resolution by evaluating the sharing pattern.

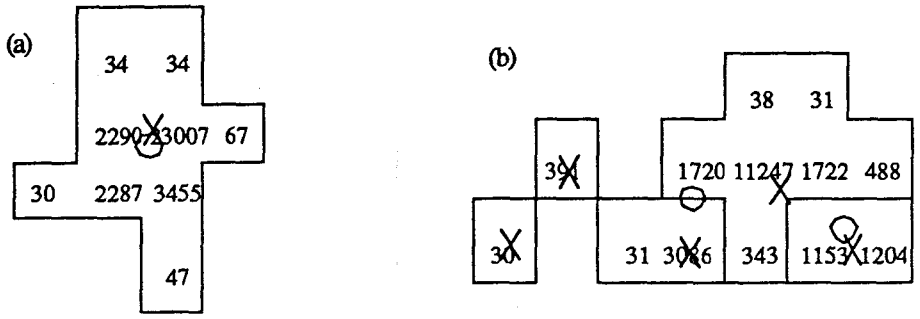

Figure 3.3 Examples of LG clusters in a view from the colliding point, (a) for a 30 GeV e, and (b) hadrons and γ's in a jet. The cluster boundary is drawn by a line including modules of which energy deposits are written. Cluster centers and track-injection points are indicated by crosses and circles, respectively.

The incident position into LG is determined by the energy-sharing pattern over the modules in a cluster assuming a single electromagnetic shower. An approximate electromagnetic shower density projected onto an arbitrary axis x which is perpendicular to the incident direction is given by the following formula;

$$\frac{dE}{dx} = \frac{E}{\lambda} \exp\left(-\frac{|x-x_0|}{\lambda}\right), \tag{3.4}$$

where λ characterizes the lateral spread of the shower determined to be 1.0 cm by optimizing the position resolution and x_0 is the incident position. In practice, a cluster is divided into three regions along an axis, in practice, in either θ or ϕ directions, as shown in figure 3.4. The first region is the most energetic row of modules, the second is more energetic side region than the third region. Fitting the energy deposits in those three regions to the above formula, the best value of x_0 in each of the two directions can be obtained.

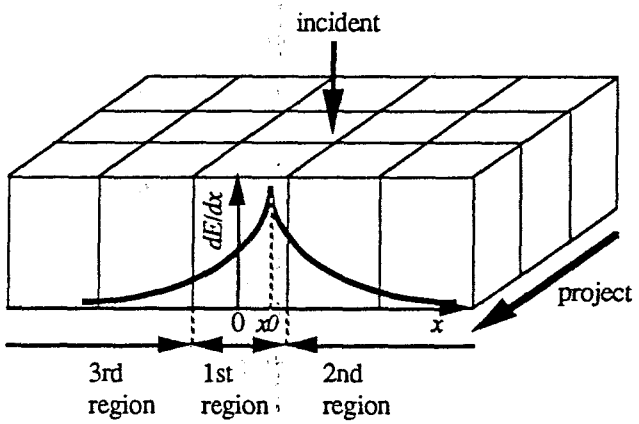

Figure 3.4 Approximated lateral profile of an electromagnetic shower in LG. The deposition is divided into three parts of integrations along the axis.

The energy resolution for e measured by using $e^+e^- \rightarrow e^+e^-$, $e^+e^-\gamma$, and $e^+e^-e^+e^-$ events is represented by the formula;[43]

$$\frac{\sigma_E}{E} = \frac{0.054}{\sqrt{E}} + 0.028, \tag{3.5}$$

where the energy E must be expressed in GeV. The angular resolutions of the measurement of incident position for e with energy around 30 GeV were;

$$\sigma_\theta = 4 \sin\theta \text{ [mrad]}, \qquad \sigma_\phi = 4 \text{ [mrad]}. \tag{3.6}$$

Each CDC track is extrapolated to LG surface and is related to the nearest LG cluster with track-cluster opening angle less than 0.1 radian typically corresponding to about two times of the LG module size. Such a cluster is called a "charged" cluster while a cluster without associating tracks is called a "neutral" cluster. The association efficiency for e with $p > 1$ GeV/c and $|\cos\theta| < 0.75$ is nearly 100 %.

3.2.3. Process-1

The event-reconstruction described above was applied to all the collected data. As a first step of data reduction with minimum bias, the trigger condition was examined again, that is, after CDC tracks and LG/LA clusters were reconstructed, the events which were found not to satisfy the physical trigger condition were discarded and the selected data were stored onto magnetic tapes. This procedure is called Process-1. Specific data reductions for various physics analyses, so-called Process-2's, were made from Process-1 data according to each specific signature.

3.3. Multihadronic event selection

3.3.1. Process-2 (Pre-selection)

The events with multihadronic final state were pre-selected by requiring that the total calorimeter energy was greater than 1.5 GeV and that there were at least two good tracks. The definitions of the total calorimeter energy and also the good track are slightly different from those in the final selection described in the next section where the criteria will be tightened. Here, the total energy is a sum of all the calibrated energies in the calorimeters. The good track is defined by the same criteria used in the final selection except for the $|\cos\theta|$ cut which is not used here. The selected events, namely Process-2 data, were stored onto another magnetic tapes. It is noted that a large fraction of the data were yet dominated by backgrounds such as pure-leptonic processes, two-photon-exchange processes, beam-associated noises, and cosmic-ray events.

3.3.2. Multihadronic selection criteria

Multihadronic event sample were made from the Process 2 data by the standard multihadronic selection which were determined in order to select $q\bar{q}$ events via single γ/Z^0 annihilation. There are many final particles in such a multihadronic event, where charged particles are mostly $\pi^{\pm}$'s and neutral ones are mostly γ's from π^0's. Since VENUS detector can well detect them, multihadronic events are characterized by large energy deposit in the calorimeters with many charged tracks. The multihadronic event sample to be used by subsequent analyses have selection criteria as follows:

(1) Total calorimeter energy E_{cal} is greater than 5.0 GeV.

(2) Number of good tracks N_{good} is at least 5.

(3) Total visible energy E_{vis} is greater than the beam energy E_{beam}.

(4) Longitudinal momentum balance P_{bal} is less than 0.4.

1. Total calorimeter energy

The total calorimeter energy E_{cal} is redefined as a detected energy sum in LG and the outer rings of LA's corresponding to the region, $|\cos\theta| < 0.89$. This is a tighter condition than that in Process-2.

2. Number of good tracks

A track is accepted as a "good track" when it satisfies all the following conditions;

$$\begin{aligned} N_{hitxy} &\geq 8, & N_{hitrz} &\geq 4, \\ |R_{min}| &< 2.0 \text{ cm}, & |Z_{min}| &< 20.0 \text{ cm}, \\ p_t &> 0.2 \text{ GeV}/c, & |\cos\theta| &< 0.85. \end{aligned} \tag{3.7}$$

where N_{hitxy} and N_{hitrz} are numbers of axial and slant wire hits, respectively. The conditions on $|R_{min}|$ and $|Z_{min}|$ suppress the particles from the beam associated backgrounds or cosmic-rays. The condition on p_t suppresses the curling tracks in CDC. Fake tracks from accidental noise hits can be completely removed. The distributions for all the three-dimensional tracks in the multihadronic data sample are shown in figure 3.5. This cut reduces τ-pair and Bhabha events which have considerable cross sections. Backgrounds which did not come from e^+e^- interaction are also reduced.

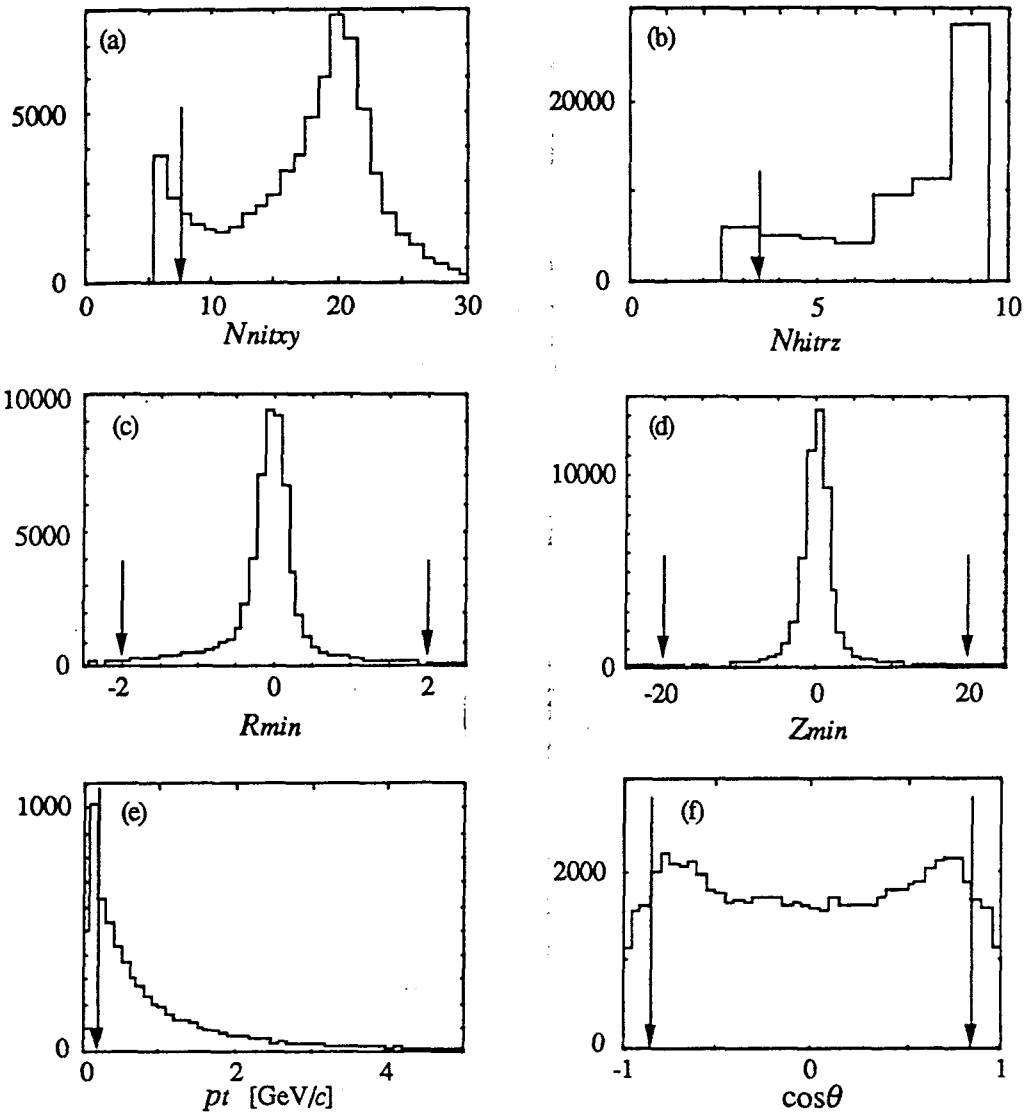

Figure 3.5 Distributions of the cut-off parameters of good track conditions, (a) N_{hitxy}, (b) N_{hitrz}, (c) R_{min}, (d) Z_{min}, (e) p_t, and (f) $\cos\theta$ for all the three-dimensional tracks in the multihadronic data sample, where cut-off points are indicated by arrows.

3. Total visible energy

Total visible energy is defined by a sum of energies of the reconstructed particles, namely tracks and clusters, defined by;

$$E_{vis} = \sum_i E_i, \tag{3.8}$$

where i runs over tracks with momentum more than 0.2 GeV/c and clusters with energy more than 0.1 GeV, neglecting their masses. This requirement reduces hadronic two-photon-exchange interaction where the high energy e^+ and/or e^- escapes toward the beam direction.

4. Longitudinal momentum balance

Longitudinal momentum balance is defined by the following formula;

$$P_{bal} = \frac{|\Sigma p_z|}{E_{vis}} \tag{3.9}$$

where the sum is taken over all the accepted tracks and clusters and p_z denotes z component of their momentum or energy. This cut also reduces two-photon-exchange events because they are usually unbalanced longitudinally. Multihadronic events with a hard γ escaping toward the beam direction are also lost.

3.3.3. Selection results

The expectation values from various known processes had been studied using Monte Carlo simulation and the real data. Figure 3.6 shows distributions of total calorimeter energy, number of good tracks, total visible energy, and longitudinal momentum balance for the events of the data and of the simulation of five-flavor $q\bar{q}$ production, each after applying the selection on the other three criteria. Due to contamination of backgrounds mainly from pure-leptonic processes and two-photon-exchange processes, the distributions don't coincide well with the expectation of $q\bar{q}$ production below the cut-off value of the selection. It is evident that the criteria on number of good tracks and on total visible energy are essentially effective to discriminate $q\bar{q}$ production from the backgrounds. The numbers of events obtained and expected from ordinary processes are summarized in table 3.1. The expectation value of "e^+e^-" which includes higher order QED processes was obtained by scanning the events with the conditions, $E_{cal} > 1.75E_{beam}$ and $N_{good} < 9$, in the multihadronic data sample. 31 events in the selected 35 events were clearly found to be such QED processes with initiating electromagnetic showers in front of the tracking volume. Three events were $q\bar{q}$ events with hard γ emission. The remaining one event was clearly a cosmic-ray shower. We did not remove these clear background events because we don't apply such a scanning for simulated events of new particles we are searching for. They will be removed by the subsequent selection criteria in the analysis.

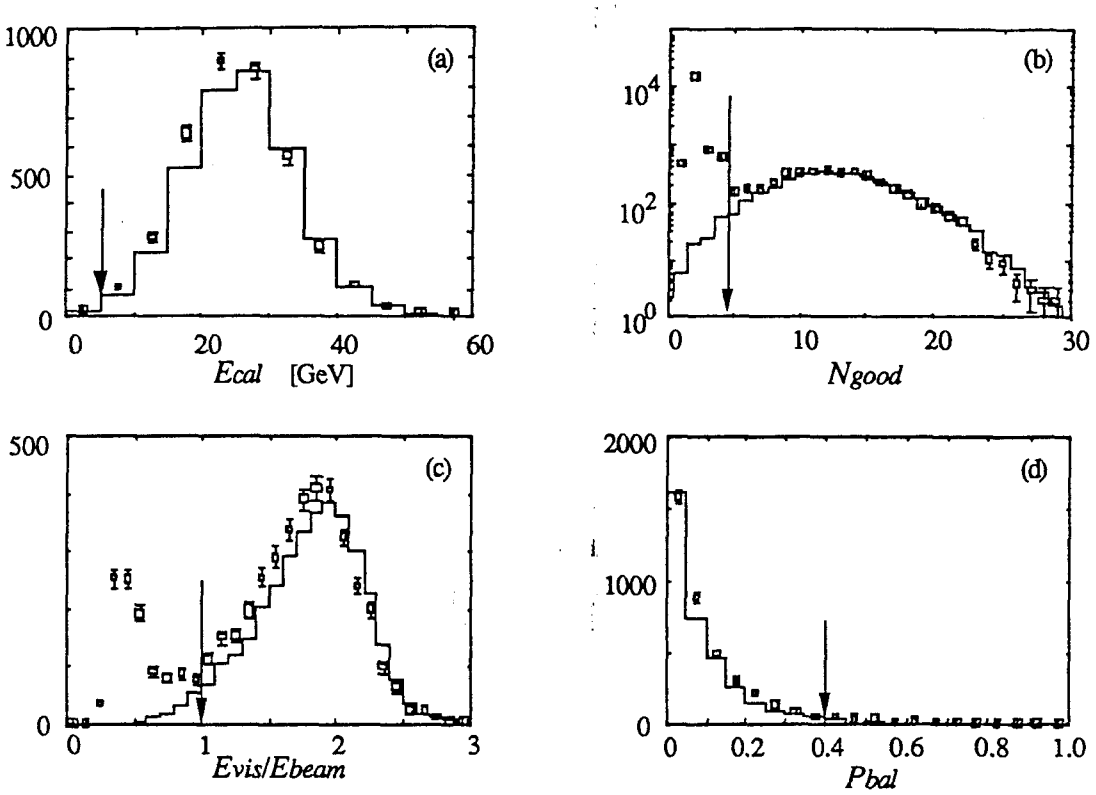

Figure 3.6 Distributions of the cut-off parameters of multihadronic selection, (a) E_{cal}, (b) N_{good}, (c) E_{vis}, and (d) P_{bal} Each distribution was taken for the events with the other three criteria.

$q\bar{q}$	$\tau^+\tau^-$	$e^+e^-q\bar{q}$	e^+e^-	cosmic-ray	data
3473	36.1	22.2	31	≥ 1	3776

Table 3.1 Numbers of events after the multihadronic selection for expected dominant reactions and for the data.

Chapter 4 Electron Identification

4.1. General

The performance of particle identification is evaluated by efficiency for the object and by misidentification probabilities of unwanted particles. In a search for new particles with small production cross section, the efficiency for detecting e essentially determines the sensitivity. The misidentification probability of hadrons should be of course small but in this analysis, may be loosened by requiring the signatures, "energetic" and "isolated" in multihadronic events. This requirement intrinsically suppresses most of background hadrons. On the other hand, when a large number of hadrons are expected such as in the study of b-quark properties, strong suppression of hadron contamination becomes important as much as the efficiency.

Particle identification is performed utilizing differences of the behaviors of particles in a detector. Charged and neutral particles are separated by a tracking detector which is sensitive only to charged particles. An electron characteristically behaves in a material due to its small mass. As a consequence of electromagnetic interaction with a material, e emits γ's (bremsstrahlung) and γ converts into an e^+e^- pair (pair-conversion). These successive reactions result in a multiplication of particles which is called an electromagnetic shower. Radiation length which is a characteristic length for material is defined by the path length of e with losing (1-1/e) $\approx$ 63 % of its energy in average by bremsstrahlung. Mean path length before γ converts is 9/7 of X_0. Other kinds of charged particles are too heavy to induce an electromagnetic shower. Hadrons do the strong interaction with nuclei in a material which leads to a hadronic shower, that is, an inelastic multiplication of hadrons. Mean free path of hadrons in material is called a nuclear interaction length, λ, which is generally much larger than the radiation length.

These features are utilized to separate e from hadrons with an electromagnetic calorimeter which is made of heavy material. The difference between electromagnetic showers and hadronic showers appears both in shower shape and in shower energy to be detected. For instance, most hadrons escapes the calorimeter without depositing much energy. Hence, a mismatch between the momentum as defined by tracking and the energy as measured by the calorimeter provides a very powerful method to separate e from hadrons.

4.2. Identification procedure

4.2.1. Selection criteria of electron identification

Combined informations on CDC tracks and the associated LG clusters are used to identify e's. We focused on the following subjects;

(1) track fiducial,

(2) cluster configuration,

(3) track-cluster matching,

(4) cluster energy to track momentum ratio, E/p, and

(5) contamination of γ-conversion.

Because of occasional hard bremsstrahlung where e loses its energy in front of LG, thereby distorting the responses of the detector, some corrections should be made before applying the selections on these subjects. The corrections for bremsstrahlung are described in the next subsection.

In order to determine the identification criteria and to estimate the efficiency for e, a minimum biased sample of e which is described in appendix D were used.

1. track fiducial

A subsequent selection to the standard "good" tracks is made requiring to satisfy both $p > 1.0$ GeV/c and $|\cos\theta| < 0.75$. The angular cut confirms to be in a sensitive region of both LG and CDC. The momentum cut was introduced because it becomes difficult to separate e from hadrons in low momentum region. An example, the scatter plot of E versus p for e's and for hadrons is shown in figure 4.1. The loose cut-off value of 1 GeV/c was placed to be tightened later in the analysis.

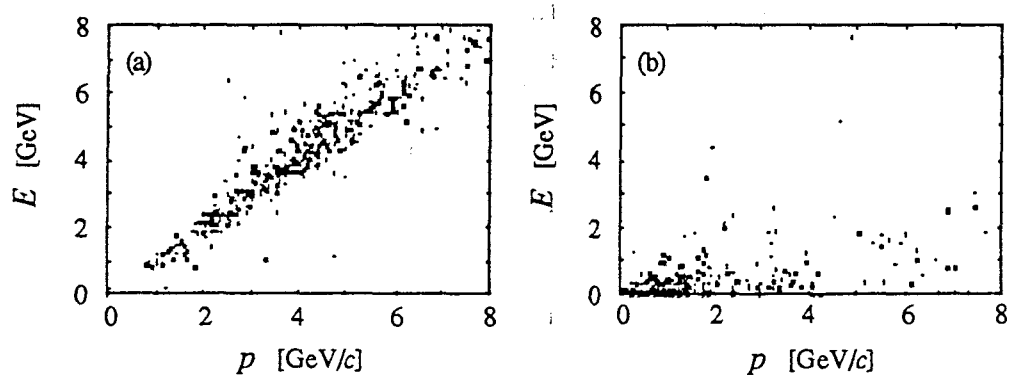

Figure 4.1 Plots of cluster energy versus track momentum, (a) for e and (b) for hadrons.

2. cluster configuration

Many hadrons and γ's are usually produced in a narrow angle region due to the jet-structure. In this case, the induced showers in LG may overlap and result in a single cluster or clusters where the energy sharing dose not reflect the true nature of the showers. In order to eliminate those low-quality clusters, we required following criteria on the associated cluster with the track:

(1) Number of associated tracks is only one.

(2) Number of adjoining clusters is at most one and it must be neutral.

The reason for that one adjoining neutral cluster is allowed is not to lose e's with a bremsstrahlung γ to result in such a topology. The efficiency of this cut for e was evaluated using the e sample to be 99.5 ± 0.2 % while the reduction rate for hadrons was 63.0 ± 0.3 % using the particles in the multihadronic event sample, each of which had passed cut 1.

3. track-cluster matching

For e, LG can measure the injection point with much better resolution than for a hadron. The deviation, D, between the injection points measured by LG and by CDC is defined as follows and is required to be less than unity;

$$D = \left(\frac{\Delta\theta}{a \sin^2\theta}\right)^2 + \left(\frac{\Delta\phi}{b}\right)^2 < 1, \tag{4.1}$$

where,

$$\Delta\theta = \theta_{cluster} - \theta_{track}, \qquad \Delta\phi = \phi_{cluster} - \phi_{track},$$

$$a = 20 \text{ [mrad]}, \qquad b = 15 \text{ [mrad]}.$$

The factor $1/\sin^2\theta$ was introduced so as to cancel out the dependence of $\Delta\theta$ resolution caused by θ_{track}. Figure 4.2 shows the distribution of D for the e sample and for the tracks in the multihadronic events.

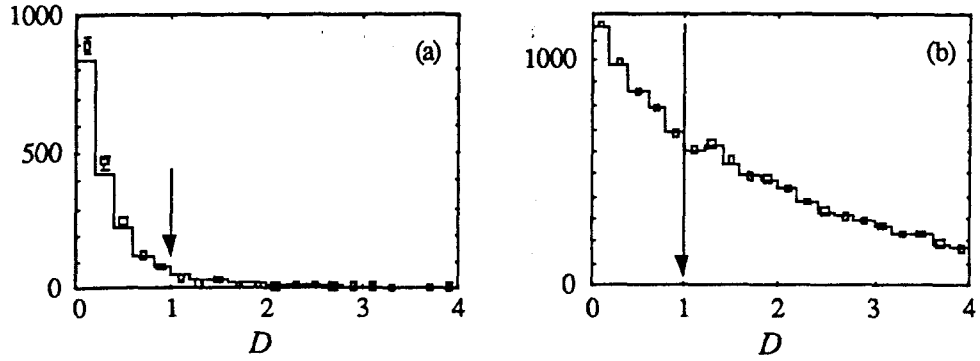

Figure 4.2 Distribution of track-cluster matching parameter D before (solid histogram) and after (square points) the bremsstrahlung correction, (a) for e and (b) for hadrons. The arrow indicates the cut-off point.

4. *E/p* ratio

Because each module of LG has a depth of 18 radiation lengths or 1 nuclear interaction length, an electromagnetic shower is well contained in LG while hadrons penetrates the total depth of LG with probability of about 1/3 without hard interaction. The energy deposition of e is equivalent to the incident energy since there is no escaping energy. Therefore the ratio of the cluster energy E to the track momentum p, E/p, distributes around unity. On the other hand, since a hadronic shower contains escaping components such as $\pi^{\pm}$, n, and p, E/p for hadrons is principally smaller than unity. Figure 4.3 shows the E/p distribution for the e sample and for the tracks in the multihadronic events, respectively. In order to extract e's, we set the following criterion on E/p;

$$0.8 < E/p < 1.3. \tag{4.2}$$

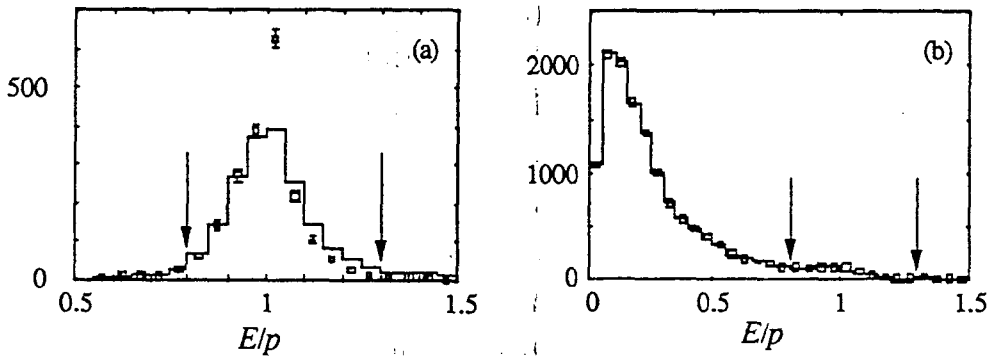

Figure 4.3 E/p distribution before (solid histogram) and after (square points) the bremsstrahlung correction, (a) for e and (b) for hadrons.

5. possibility of γ-conversion

The material before CDC, amounting to about 0.063 radiation lengths at θ = 90°, causes a γ-conversion to an e^+e^- pair with probability of 5 %. Since we have no

interest in such e's, they must be removed. Such $e^{\pm}$ from γ-conversion always accompanies $e^{\mp}$ nearly in the same direction at the conversion point. The $e^{\pm}$ candidates which have such $e^{\mp}$ are removed if the following conditions are satisfied at the point where the two tracks are parallel in r-ϕ plane;

$$\begin{aligned} 5\ [\mathrm{cm}] < Rpara < 100\ [\mathrm{cm}], \\ |\delta xy| < 0.5\ [\mathrm{cm}], \\ |\delta\theta| < 100 \sin^2\theta\ [\mathrm{mrad}], \\ E'/p' > 0.7\ (\mathrm{if}\ p' > 1.0\ [\mathrm{GeV}/c]), \end{aligned} \tag{4.3}$$

where $Rpara$ is the distance of the parallel point from z axis and $|\delta xy|$ is the distance between the two tracks in r-ϕ plane. The conversion vertex should be after the beam pipe (R = 9.0 cm) and mostly before CDC (R = 25 cm). $|\delta\theta|$ is a polar angle difference between the two tracks and must be small for those from a pair creation. E' and p' are the cluster energy and the track momentum of the oppositely charged particle, which should be $e^{\mp}$. The definitions of the parameters are illustrated in figure 4.4.

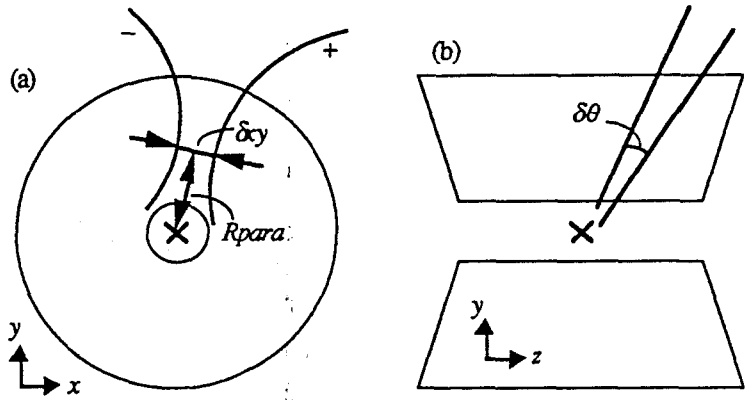

Figure 4.4 Definition of the parameters for conversion finding, (a) in x-y view and (b) in y-z view.

The solid histograms in figure 4.5 show the distributions of the cut-off parameters for converted isolated γ's, each after requiring all the criteria to find a conversion except for itself. The dashed histograms shows the same distributions for non-converted particles using the hadron-like tracks with $E/p < 0.4$ in the multihadronic event sample. The efficiency to find a conversion of isolated γ is estimated by Monte Carlo simulation as shown in figure 4.6.

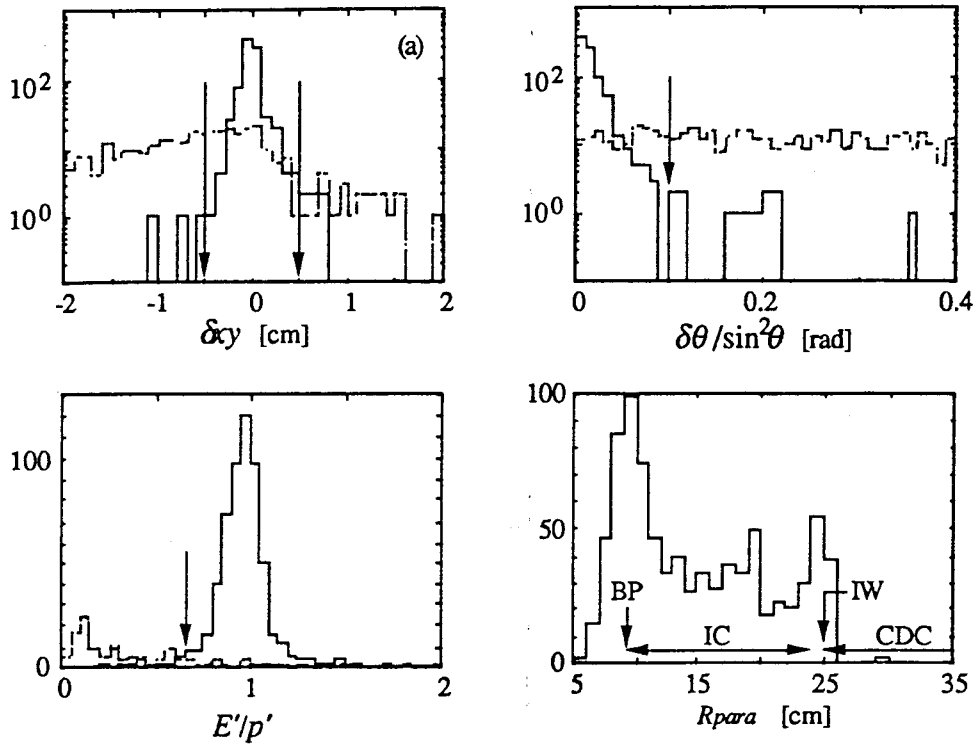

Figure 4.5 Distributions of parameters to find a conversion e^+e^- pair, where distributions of (a) δxy, (b) $\delta\theta$, and (c) E'/p', (d) R_{para} were made with all the other criteria of conversion finding, each for the converted γ's in the simulation (solid) and for hadron-like tracks in the multihadronic events. The conversion point in (d) clearly reflects the density of the material of the detector as the peaks at BP (beam-pipe) and IW (inner wall of CDC).

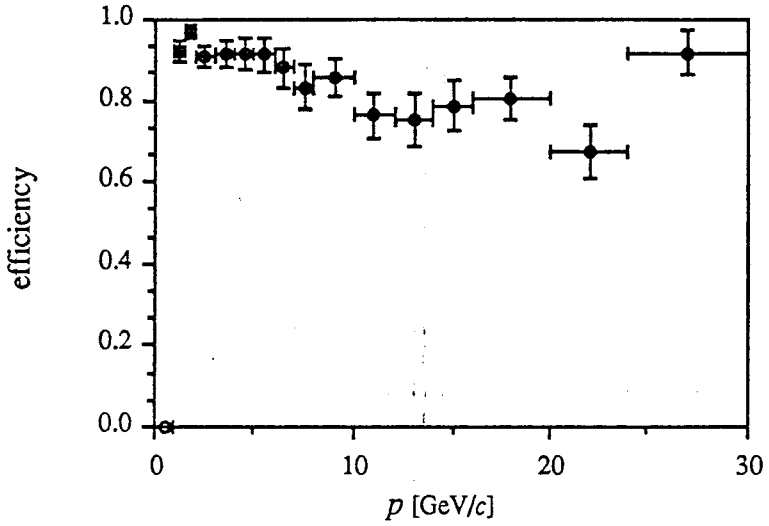

Figure 4.6 Conversion finding efficiency estimated by the simulation with respect to the converted track momentum for e from a conversion of isolated (single)γ.

4.2.2. Corrections for bremsstrahlung

The material before LG may also cause a bremsstrahlung. The radiated γ, which carries away part of the energy of e, makes additional energy deposition around the e and may deteriorate E/p and $\Delta\phi$ for the true e. If the radiated γ is identified, it can be possible to correct the effect before applying the cuts in the identification procedure described above. Therefore, a search for a neutral cluster corresponding to such a radiated γ is made assuming that the radiation had occurred at one of the following probable four points; beam pipe (9.25 cm), the inner wall of CDC (25 cm), the outer wall of CDC (125 cm), and outer drift tubes (ODT) (160 cm). If the expected hit point on LG, $(\theta_\gamma,\phi_\gamma)$, of γ originating from one of those points matches well to a real neutral cluster position, (θ_n,ϕ_n), with energy E_n, this cluster is identified as coming from a radiated γ. The criteria for the matching parameter D_b was defined as follows,

$$D_b = \left(\frac{\Delta\theta_b}{c\ \sin^2\theta}\right)^2 + \left(\frac{\Delta\phi_b}{d}\right)^2 < 1, \tag{4.4}$$

where,

$$\Delta\theta_b = \theta_n - \theta_\gamma, \qquad \Delta\phi_b = \phi_n - \phi_\gamma,$$

$$c = 20\ \text{[mrad]}, \qquad d = 20\ \text{[mrad]}.$$

Figure 4.7 shows the distribution of D_b for the e sample and for hadron-like sample with $E/p < 0.4$ in the multihadronic event sample.

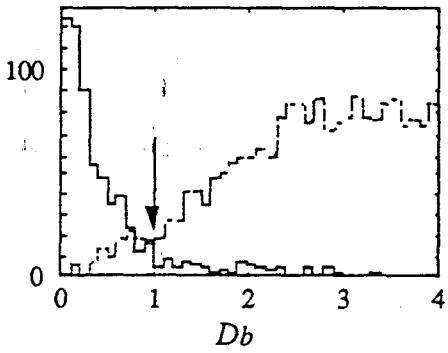

Figure 4.7 Matching parameter D_b between the real and the expected cluster from bremsstrahlung, for the e sample (solid) and for the hadron-like sample in the multihadronic events (dashed).

A hard bremsstrahlung is considered to result in one of the three cases shown in figure 4.8, for each of which a different correction should be made.

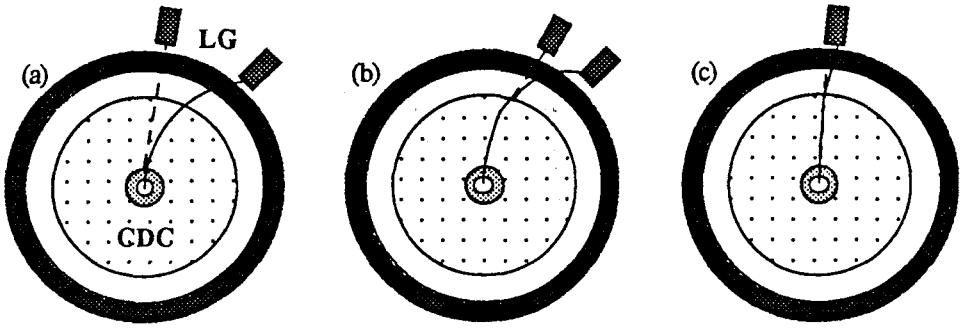

Figure 4.8 Three cases from a hard bremsstrahlung.which we have considered. Illustration (a), (b), and (c) correspond to cases (1), (2), and (3) in the text, respectively.

(1) A neutral cluster was identified as a radiation before CDC.
Both the track momentum p and the cluster energy E corresponding to the e are corrected so as to include the neutral cluster energy E_n corresponding to the radiated γ energy.

(2) A neutral cluster was identified as a radiation after CDC.
E is corrected so as to include E_n and the extrapolation of the CDC track to LG is retried assuming that the track had lost E_n at the radiation point.

(3) No radiated γ candidate was found but the expected hit point of the γ was on the e cluster with $E/p > 1$.
Assuming that the bremsstrahlung of energy $E_\gamma = E - p$ had occurred at either the beam pipe or the inner wall of CDC and that the cluster is composed of two overlapping showers of e and γ, the injection point of the track is replaced by the hypothetical mean position of the e and the γ by the next empirical formulae;

$$\theta_{track} \leftarrow \frac{\theta_{track}p^{\alpha}+\theta_{\gamma}E_{\gamma}^{\alpha}}{p^{\alpha}+E_{\gamma}^{\alpha}}, \quad \phi_{track} \leftarrow \frac{\phi_{track}p^{\alpha}+\phi_{\gamma}E_{\gamma}^{\alpha}}{p^{\alpha}+E_{\gamma}^{\alpha}}. \quad (\alpha = 0.34) \tag{4.5}$$

The correction on p is also made so as to minimize $|\Delta\phi| = |\phi_{track} - \phi_{cluster}|$ in above formula.

Figure 4.9 shows the correlation between E/p and $Q \cdot \Delta\phi$ for e and for hadrons each before and after the correction. The ordinate, $Q \cdot \Delta\phi$ is $\Delta\phi$ multiplied by its electric charge. Because a bremsstrahlung of case (3) always increases both E/p and $Q \cdot \Delta\phi$, there is a tail in the upper-right region in figure 4.9 (a), which is to be corrected as shown in (b).

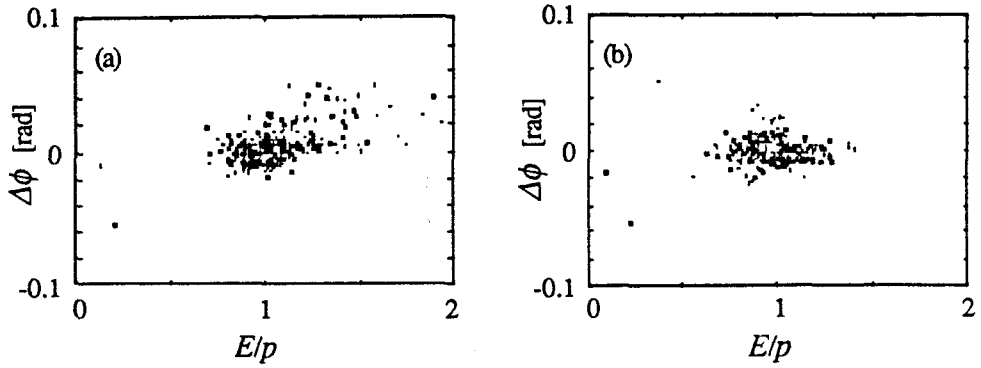

Figure 4.9 Correlation between E/p and $Q \cdot \Delta\phi$ for e, (a) before and (b) after the bremsstrahlung correction.

4.3. Efficiency and backgrounds

4.3.1. Efficiency for detecting an isolated electron

The efficiencies of the cuts introduced in the previous section and the overall efficiency were estimated both by the e sample and by the simulated single e events with detector simulation program VMONT, where cuts 1 and 5 can not be evaluated by the sample due to the bias caused by the selection condition. Table 4.1 shows each efficiency and the overall efficiency with and without the bremsstrahlung correction for single (or isolated) e in the fiducial. The efficiency is momentum-dependent as shown in figure 4.10. The discrepancy between the two estimations in low momentum region was mainly due to cut 3, the track-cluster matching cut, where this cut essentially determines the overall efficiency. This means that the lateral spread of electromagnetic shower is not completely simulated. This may be responsible to the lack of optical treatment of Cerenkov light in the simulation. The discrepancy will be included into the systematic uncertainty in the analysis.

source	sample		VMONT	
correction	on	off	on	off
cut 1	–	–	99.7	99.7
cut 2	99.5	99.5	99.6	99.6
cut 3	90.3	83.4	86.8	79.5
cut 4	94.3	90.0	96.5	93.0
cut 5	–	–	99.9	99.9
total	86.6	78.3	81.6	75.6

Table 4.1 Efficiencies of each cut in the electron identification for e in the fiducial by the e sample and by the simulation, with and without the bremsstrahlung correction. Values for cut 1 only represent the efficiencies to be recognized as a good track.

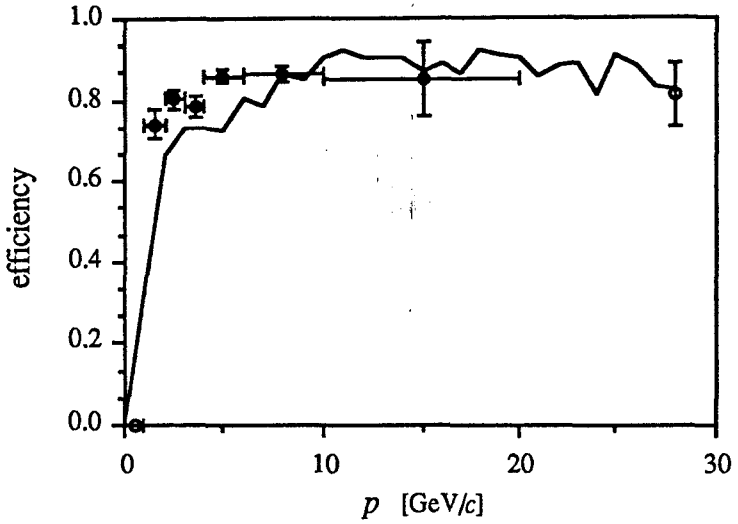

Figure 4.10 Efficiency of the identification procedure for isolated e. estimated by the e sample (circle with error bars) and by Monte Carlo (solid line).

4.3.2. Efficiency for electron and the background contamination in multihadronic events

We applied this identification procedure to the multihadronic event sample with $\sqrt{s}$ between 54 and 61.4 GeV corresponding to the integrated luminosity of 28.8 pb^{-1}. Total 310 e candidates were selected from the 3776 multihadronic events.

Because there are vast number of hadrons or γ's in multihadronic events, it is difficult to eliminate their contamination to the e candidates completely. Moreover, the efficiency for tagging e will be degraded in multihadronic events because of the overlapping of showers in LG and the scrambling of hit points of CDC in a jet.

Since the responses of CDC can be simulated precisely in VMONT, the contamination of converted γ's can be estimated by VMONT fairly well. However, as described in appendix C, the lateral spread of hadronic shower in LG may not as well be reproduced in VMONT. The cut on track-cluster matching gives the discrepancy in reduction rate. Considering that E/p for hadrons are independent with track-cluster matching, we utilized E/p distribution to normalize the spectrum. Since the contribution of e can be neglected in the region $0.4 < E/p < 0.8$, we have determined the normalization factor to adjust the entry number in this region. Figure 4.11 shows the E/p distribution in the data and the normalized one in the simulation, where the line shows the exponential curve fitted by the data point in the region.

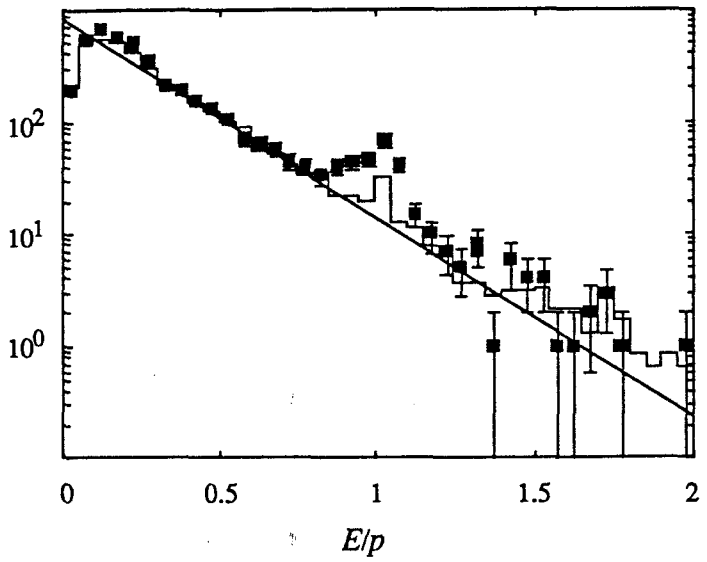

Figure 4.11 *E/p* distribution after the cut on track-cluster matching for the data (black square) and for the simulation of hadrons in multihadronic events (histogram). The line was fitted using the data points in the range $0.4 < E/p < 0.8$.

The reduction efficiency of converted γ and the false-reduction rate of non-converted particles are influenced by the surrounding particles in the event. In multihadronic events, the mean reduction efficiency for e from a converted γ was estimated to be 66 ± 4 % using the Monte Carlo simulation and the mean false-reduction rate was estimated to be 1.3 ± 0.1 % using the hadron-like tracks with $E/p < 0.4$ in the real data.

The expected ingredients of the candidates are summarized in table 4.2, where the sources of e are classified with primary quark, including the decay-product of the cascade decay. Figure 4.12 shows momentum distribution for the e candidates in the data and for the expected yields of e's from the ordinary multihadron production together with the backgrounds by the simulation. We observed no significant discrepancy from the expectation.

	hadrons	γ	$b \to e$	$c \to e$	$u,d,s \to e$	total	data
produced	74750	79100	342	631	475	155298	–
p and $\lvert\cos\theta\rvert$	17491	471	121	185	38.9	18267	21732
before cut 5	179	157	65.2	62.2	10.7	474	422
identified as e	173	52.6	62.6	59.7	10.3	358	310
$1<p<2$ [GeV/c]	70.5	37.4	13.2	21.6	7.1	150	131
$2<p<4$ [GeV/c]	61.9	10.6	16.5	21.3	2.6	113	88
$p>4$ [GeV/c]	40.9	4.5	32.9	16.8	0.6	95.7	91

Table 4.2 Summary and the expected ingredients of the e candidates in the multihadronic event sample, where p and $\lvert\cos\theta\rvert$ means the requirement to be well reconstructed with $p > 1$ GeV/c and $\lvert\cos\theta\rvert < 0.75$.

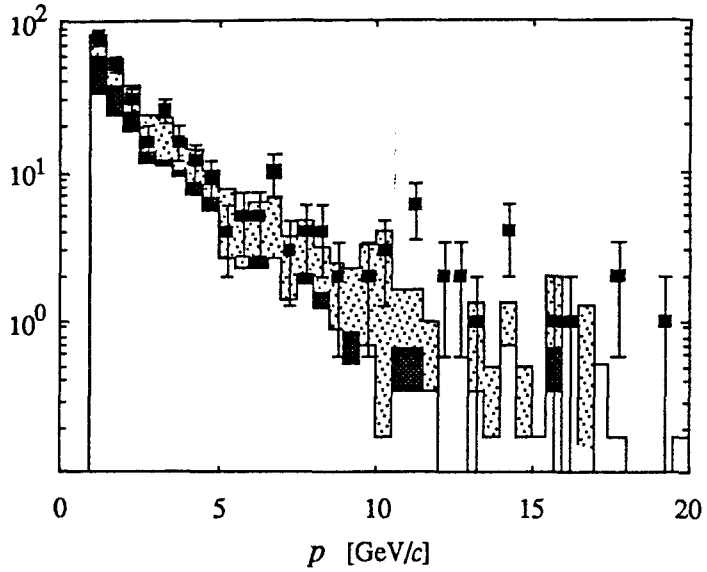

Figure 4.12 Obtained momentum distribution of the e candidates (black square) and the expected signals and backgrounds by the simulation. The white, dark, and dotted area in the histogram exhibit the contribution of hadrons, converted γ's and e's from decays.

In searching for new particles, all those ordinary yields become backgrounds. Since the expected yields from the new particles in this thesis will be small compared with those ordinary yields, the other condition should be required to enhance them as described in the next chapter.

Chapter 5 Search for New Particles in Electron-inclusive Multihadronic Events

5.1. Total cross sections of the new particles

Total cross section σ is related to expected number of events N_{exp} through;

$$N_{exp} = \sum_i \sigma_i L_i \varepsilon_i, \tag{5.1}$$

where the sum is taken over the center of mass energies with integrated luminosity L and selection efficiency ε. The basic mechanisms and the cross section formulae of the new particle productions were described in chapter 1. We conservatively ignored the QCD correction which would increase +5 % in total cross section. Because of unknown behaviors due to meson resonances near the threshold, we ignored the cross section with center of mass energy below 1 GeV over the threshold for the colored particle productions, namely for new quarks and a leptoquark.

The significant contribution of higher order diagrams, what is called the radiative correction, was included into σ and ε. We used the calculation by Berends, Kleiss, and Jadach for γ/Z^0 annihilation processes, where vertex correction, vacuum polarization, and initial-state radiation are included as described in appendix B. The initial-state radiation is most significant in heavy particle productions because it enhances the threshold effect which suppresses the production. For E^0 production, which is a W-exchange process, we used the basic procedure by Etim, Pancheri, and Touschek also described in appendix B, where only initial-state radiation is included.

The corrected total cross sections of the new particle productions at $\sqrt{s}$ = 60 GeV are drawn in figure 5.1 as functions of the new particle mass.

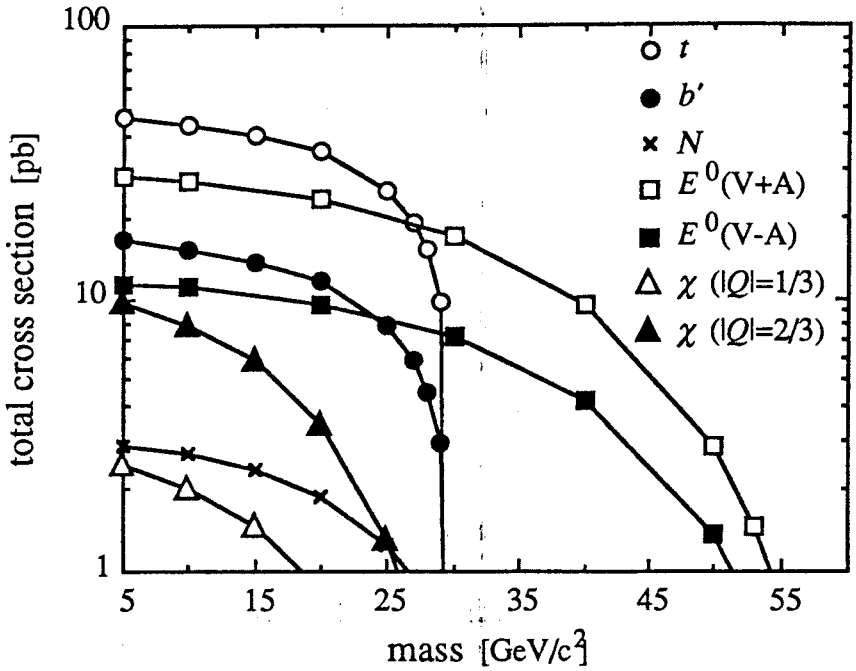

Figure 5.1 Total cross sections for the new particle productions as functions of these masses at $\sqrt{s}$ = 60 GeV.

5.2. Integrated luminosity

As already described in chapter 2, the integrated luminosity was measured by using Bhabha events. Because Bhabha scattering is detected mainly by a calorimeter, the luminosity can be independently measured by the three calorimeters in VENUS detector. In this thesis, we used the integrated luminosity measured by large angle Bhabha scattering detected by LG in the region, $|\cos\theta| < 0.743$,[44] which has sufficiently a large cross section to give a small statistical error and also a clear event topology to give a small systematic error with the help of CDC. The cross section of this reaction was calculated according to the electroweak theory including α^3-order radiative corrections.[45]

The data were grouped into 6 parts with respect to center of mass energy region in this analysis, where the minimum efficiency and the minimum total cross section were chosen for the new particle production. The corresponding integrated luminosities L's are summarized in table 5.1. The background contamination was expected to be less than 1 % and was corrected.

$\sqrt{s}$ [GeV]	N_{ee}	$L \pm$ stat. $\pm$ syst. [pb^{-1}]
54.0~55.0	972	2.612 ± 0.084 ± 0.068
56.0~58.0	3572	10.236 ± 0.171 ± 0.266
58.5~59.5	945	2.922 ± 0.059 ± 0.076
60	1084	3.486 ± 0.105 ± 0.090
60.8	1336	4.412 ± 0.121 ± 0.115
61.4	1524	5.115 ± 0.131 ± 0.133
total	9431	28.78 ± 0.30 ± 0.75

Table 5.1 The integrated luminosities measured by large angle Bhabha events, where N_{ee} is the number of observed Bhabha events.

5.3. Selection criteria

We are searching for new heavy particles decaying into e with hadrons in the multihadronic event sample. In order to find such signals, we must optimize the selection criteria to be effective and distinctive from backgrounds. The optimization and quantitative evaluation of the result were performed using Monte Carlo technique described in appendix A.

In the following subsections, we demonstrate the distributions for the new particle productions, assuming these typical specifications on these masses as, $m_t = m_{b'} = 28$ GeV/c^2, $m_N = m_\chi = 25$ GeV/c^2, and $m_E = 55$ GeV/c^2, where the electron-type neutral heavy lepton E^0 is V+A type and the leptoquark has $Q_\chi = 2/3$ and $B(\chi \to e^+ d) = 50$ %.

We start to search for new particles described in chapter 1 from the multihadronic event sample described in chapter 3. Next, high-thrust events are removed, where thrust is a variable to measure the degrees of two-jet structure defined later, which gives a low value for a heavy particle production event. Our essential strategy is to search for energetic and isolated e, where the "isolated" means that there is no activities of other particles around the e. A "prompt" e from a decay of a heavy particle tends to be energetic and isolated from the other decay-products because the heavy parent particle nearly at rest gives the decay-products isotropically ejected. An example of a prompt e is the e in the decay, $t \to b \nu_e e^+$, while the e from the cascade decay, $t \to bX \to e^- Y$, is not considered as the "prompt" e in our definition. The isolation requirement makes the signal clear, suppressing most of the backgrounds from ordinary multihadronic events, where a small value of the releasing energy in the decay and a large boost of the parent particle make it difficult to yield such an isolated e. We used quite the same selection in searching for the various new particles because the above mentioned feature is common to all of them. The selection criteria are classified into

three parts, namely, those used in selecting events as described in chapter 3, the low-thrust condition, and the isolated e condition.

5.3.1. Multihadronic event condition

The standard multihadronic selection criteria were optimized for ordinary quark-pair (u,d,s,c,b) productions as described in chapter 3. Though these criteria did not aim particularly to select a possible new particle production, they are sufficiently general to be adopted. They are rather loose so as not to reduce critically the new particle production. As an evidence of the looseness, each distribution of the criteria is shown in figure 5.2 for the events which passed the other criteria of the multihadronic event.

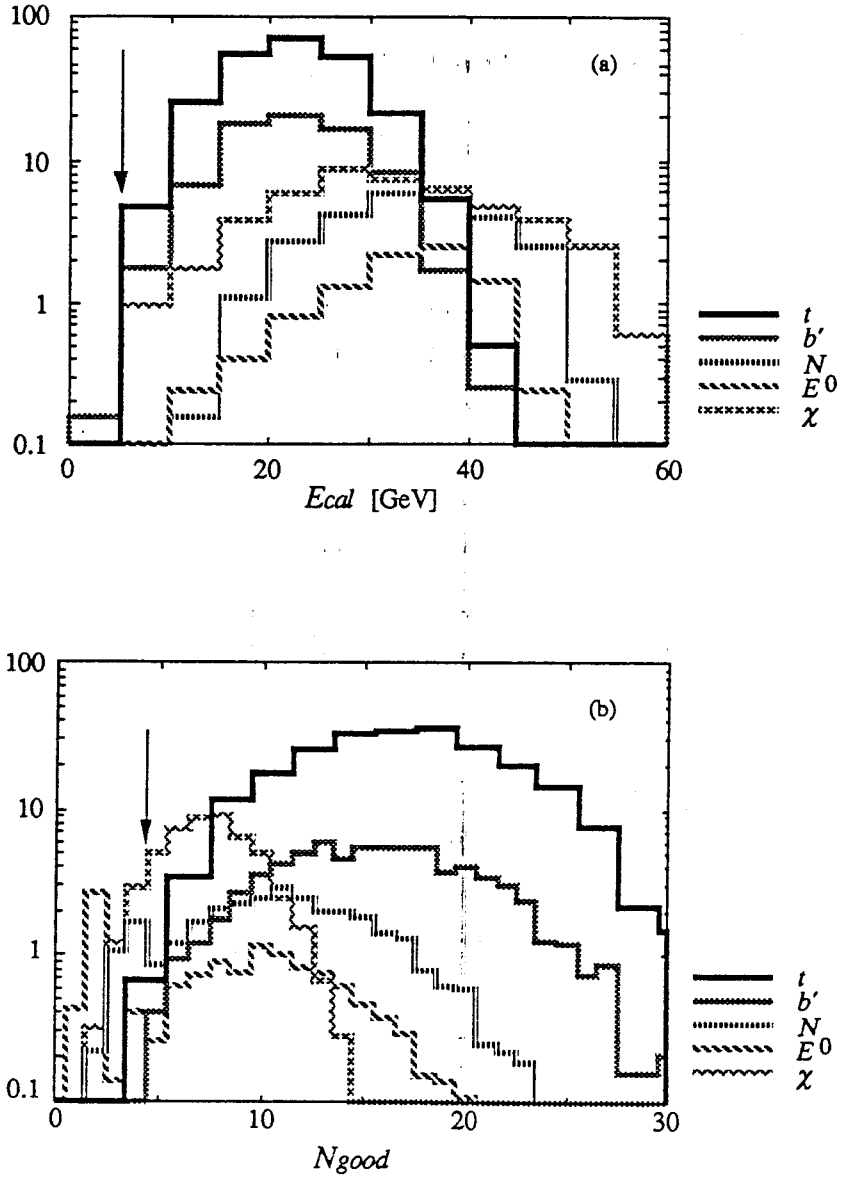

Figure 5.2 Distributions of (a) total calorimeter energy and of (b) number of good tracks, for the simulated new particle productions, each of which were taken for the events with the other three criteria of the multihadronic event. (continue to the next page)

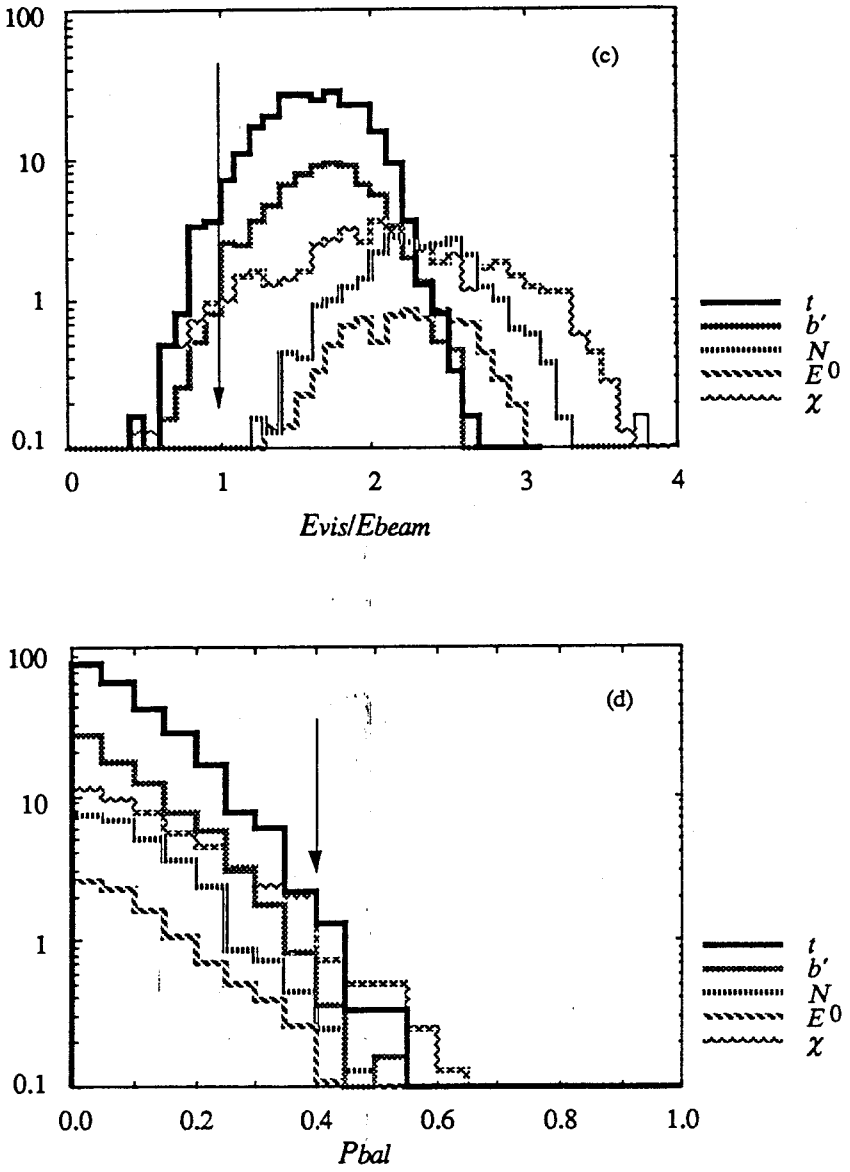

Figure 5.2 Distributions of (c) total visible energy and of (d) longitudinal momentum balance, for the simulated new particle productions, each of which were taken for the events with the other three criteria of the multihadronic event.

5.3.2. Low-thrust condition

Thrust, T, is defined by the following formula, representing a collimation of energy-flow along an axis;

$$T = \max\left[\frac{\sum|p_i \cdot t|}{\sum|p_i|}\right], \tag{5.2}$$

where a unit vector t, the thrust axis, is chosen to maximize T. Thrust value is in a range $0.5 < T < 1.0$ and the event with $T \approx 1$ corresponds to a collinear two-jet event. Thus, ordinary $q\bar{q}$ production mainly results in a high thrust value because of the two-jet structure. On the other hand, a low thrust value is generally expected for a heavy

particle production near its threshold because the decay-products will be ejected isotropically.

Figure 5.3 shows the obtained thrust distribution for the data and those expected for the new particles. To enhance the new particle signals from the background of ordinary multihadronic events, we imposed a criterion on thrust to be less than 0.95.

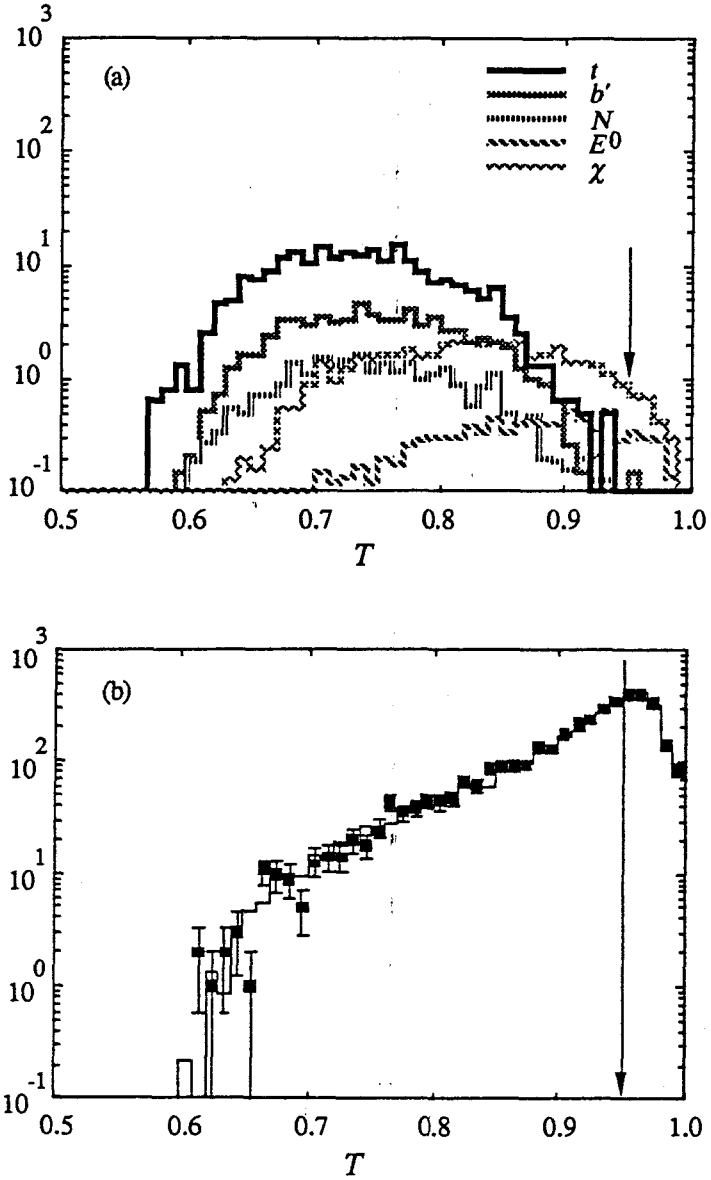

Figure 5.3 Thrust distributions, (a) expected for the new particles and (b) obtained for the data (square) and expected for ordinary multihadronic events (histogram).

5.3.3. Isolated electron condition

In principle, an e produced in a decay of a light particle cannot simultaneously satisfy the two signatures, "energetic" and "isolated", because of smallness of released

energy in the decay and large boost of the light parent particle. They are only expected for heavy particle decays.

There are many particles in a multihadronic event and if there is no activities of other particles around a particle, the particle is said to be "isolated". In order to measure the degree of such isolation of e, we defined an isolation angle δ by a maximum half angle of the cone around the e , where energy sum of other particles inside the cone must be than 1.0 GeV as shown in figure 5.4. The cut-off energy of 1.0 GeV allows small contamination of accidental noises.

We applied the cuts on scaled momentum of e, $x_e = p_e/E_{beam}$, and the isolation angle δ. Figure 5.5 shows the distribution of x_e, where we put the cut-off as $x_e > 0.15$. Figure 5.6 shows the distribution of δ after the scaled momentum cut, where we put the cut-off as $\delta > 30°$. Events with at least one such energetic isolated e are now treated as possible candidate for a new particle.

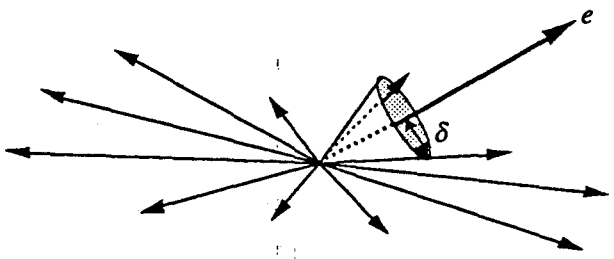

Figure 5.4 Definition of the isolation angle δ. In this example, the nearest particle to e has small momentum (or energy) below 1 GeV and the cone energy exceed 1 GeV with the second particle with opening angle δ.

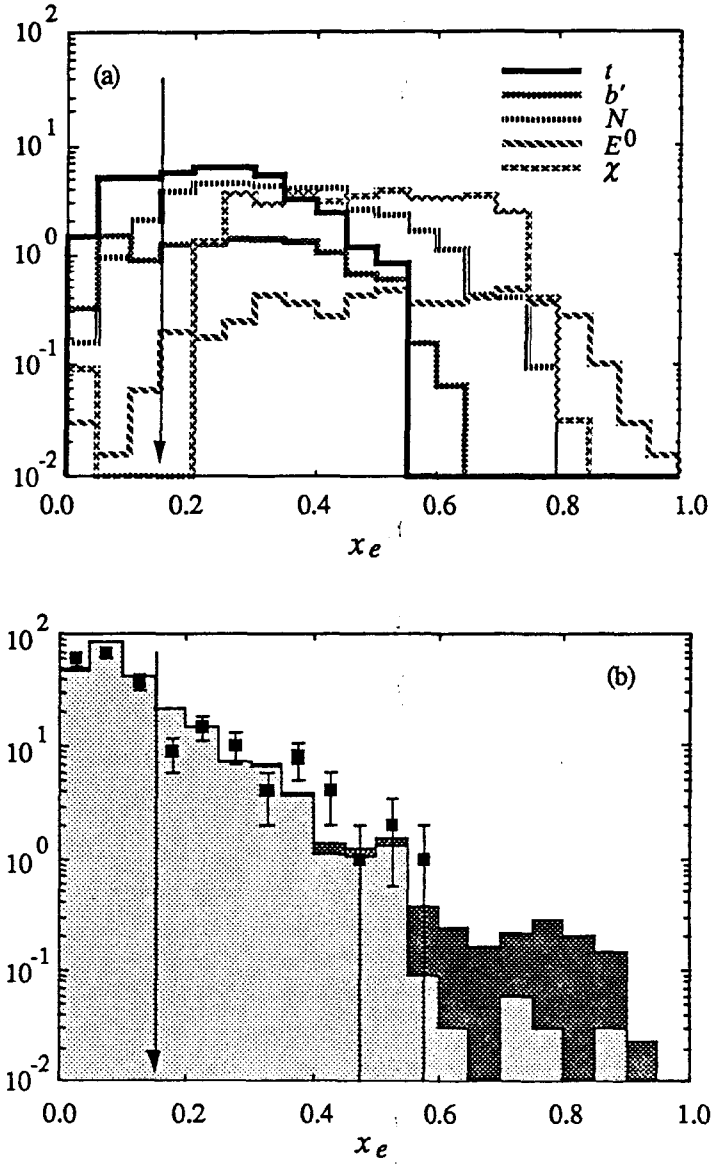

Figure 5.5 Scaled momentum distribution for e, (a) for the new particle (Monte Carlo) and (b) for the data and the expected background (Monte Carlo) where dotted area came from multihadron productions via single-photon process and dark area came from two-photon process.

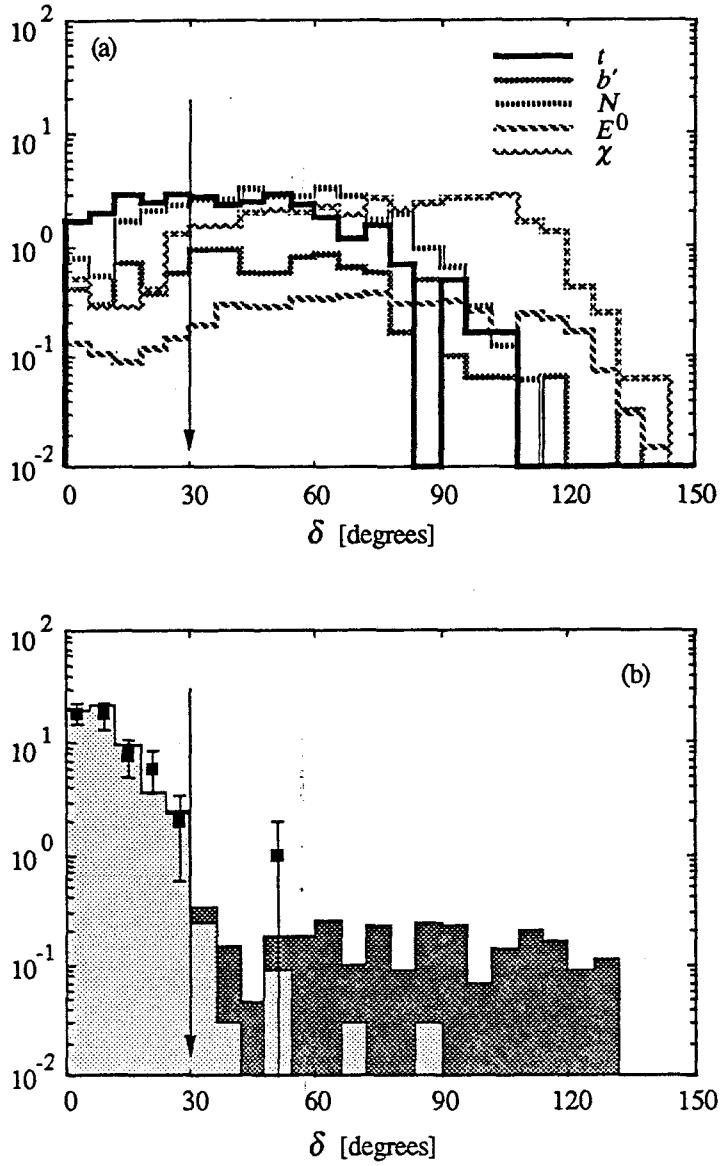

Figure 5.6 Distribution of isolation angle δ of e with $x_e > 0.15$, (a) for the new particles and (b) for the data and expected backgrounds in the same format as in figure 5.5.

5.4. Results and discussion

5.4.1. Selection results

There remains one event with $\sqrt{s}$ = 60.8 GeV in the data as shown in figure 5.6. Table 5.2 shows a summary of the selection for data and the expected numbers of events for ordinary processes and for the new particles with given masses.

	data	expected background			signal				
		$q\bar{q}$	$eeqq$	others	t	b'	N	E^0	χ
produced	–	4624	–	–	248	76.5	31.2	14.9	30.8
multihadronic	3776	3473	22	68	234	72.6	27.3	9.1	22.6
Thrust	2420	2197	19	2.5	234	72.4	27.2	8.1	21.6
Isolated e	1	1.0	2.6	< 0.1	16.7	5.8	18.6	4.5	12.7

Table 5.2 Number of events in the selection for the data and Monte Carlo simulations, where E^0 is assumed to be of V+A type and the charge of χ is assigned to 2/3 with $B(\chi \to e^+d) = 50$ %. The "others" in background includes τ-pair and Bhabha events. Here, the masses of the new particles were assumed as, $m_t = m_{b'} = 28$ GeV/c^2, $m_N = m_\chi = 25$ GeV/c^2, and $m_E = 55$ GeV/c^2.

Figures 5.7 shows the event display of the remaining event in the real data. We really do not know what this event is but it dose not conflict with the assumption of $ee \to eeqq$ reaction. This event clearly includes two e's and two jets, where e^- with $p =$ 17.9 GeV/c was recognized as the isolated e while e^+ with $p = 3.3$ GeV/c was dropped by the requirement, $p = x_e E_{beam} > 4.56$ GeV/c. Each jet has three strongly collimated charged tracks and no neutral clusters. The cluster with energy of 5.1 GeV may be also considered as a overlapping cluster of a charged hadron with momentum of 7.8 GeV/c and a γ.

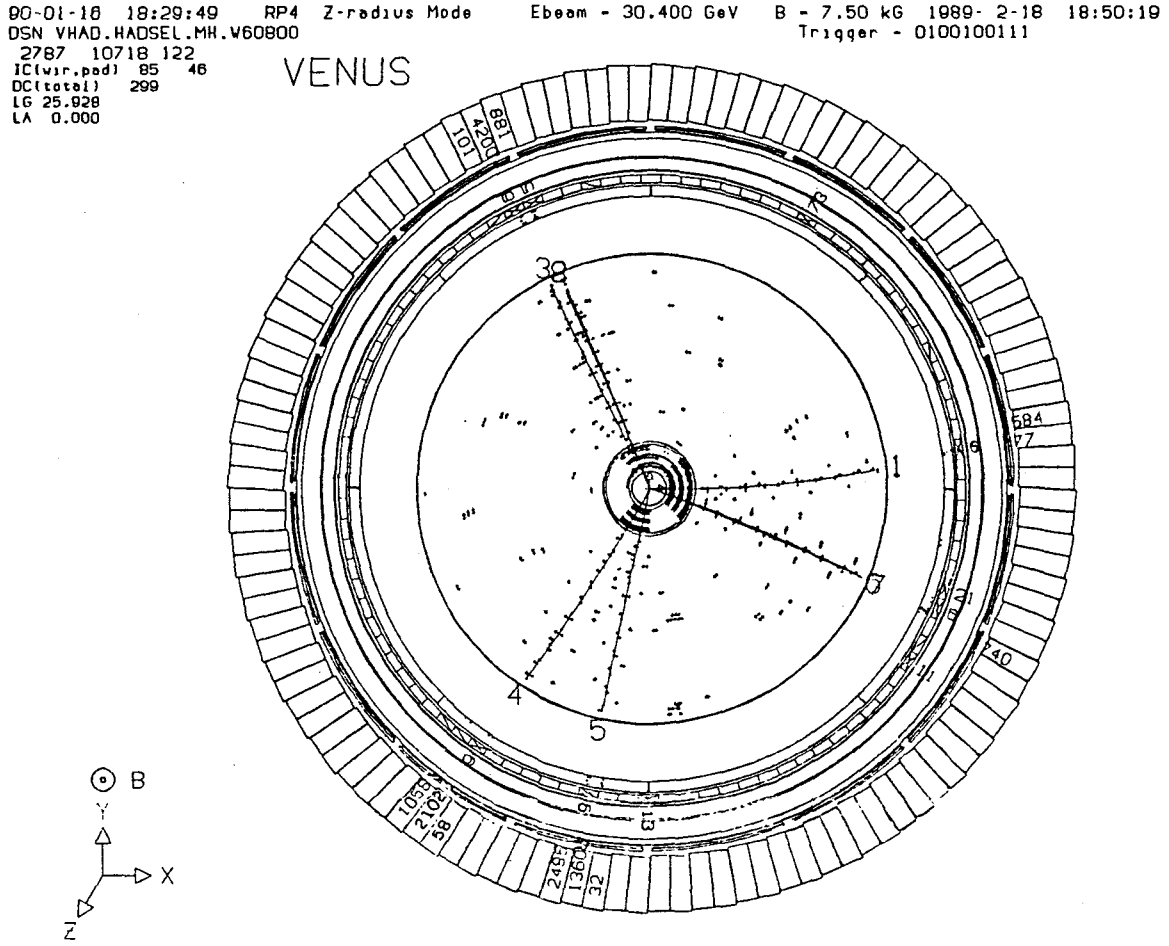

Figure 5.7 Display of the selected event in r-ϕ view, the track numbered as 5 is the isolated e (17.9 GeV/c) and number 4 is also a e (3.3 GeV/c).

We did not intend to study rare events of ordinary particle production, where a large error in estimation of the selection efficiency is expected. If we found an excess in the result, the error in background estimation would be precisely evaluated in order to prove the excess as an indication of a new particle. However, since the result shows no such indication, we proceed the argument to set constraints on the new particle productions. In evaluating the limits, it is simplest and most conservative to consider the remaining event to be a signal of each new particle without subtracting the background.

5.4.2. Systematic errors for the new particle productions

In performing a statistical argument on the observed phenomena, the systematic error of the expected number of events for a possible new particle production must be taken into account. The total cross section for the new particle production has some

ambiguity in radiative correction. The luminosity measurement of course has its statistical and systematic errors. The error of the efficiency comes from many sources of uncertainty such as, the statistics of the Monte Carlo simulation, the hadronization processes, the decay branching ratios, inaccuracy of the detector simulation, and the e identification efficiency. Table 5.3 shows each contribution of the source of uncertainty. Total systematic error was evaluated by summing them quadratically because they are nearly independent. Each number of events for the new particle was lowered by the amount of the systematic error when evaluating the upper limit of the yield.

source of uncertainty	t	b'	N	E^0	χ
radiative correction	3 %	3 %	3 %	10 %	3 %
integrated luminosity	4 %	4 %	4 %	4 %	4 %
statistics of Monte Carlo	9 %	6 %	5 %	6 %	5 %
QCD, fragmentation	5 %	5 %	5 %	5 %	5 %
branching ratio to e+hadrons	9 %	9 %	5 %	5 %	free
detector simulation	4 %	4 %	4 %	4 %	4 %
e identification	6 %	6 %	6 %	6 %	6 %
total	17 %	15 %	12 %	16 %	12 %

Table 5.3 Systematic errors in the numbers of events from the new particles.

1. Radiative correction

The error of the correction by Berends, Kleiss, and Jadach was estimated to be 3 % which is implied by the deviation of total cross section when the full electroweak correction by Fujimoto and Shimizu is used.[46] The error of the correction for E^0 production, where only the effect of real γemission is included, was estimated to be 10 %, led by the fact that the effect of virtual corrections in neutrino-pair production via Z^0 annihilation is +8.4 % at $\sqrt{s}$ = 60 GeV.

2. Luminosity measurement

The luminosity measurement was already described in chapter 2. The statistical part should be combined quadratically weighted by the expected contribution of each data-taking period. In the new particle productions, the data with the maximum center of mass energy of 61.4 GeV most strongly contributes to the expected number of events, where the statistical error was relatively 2.6 %. Additional contribution from the other data always reduces the statistical error which was neglected safely. The systematic error in the luminosity measurement was also 2.6 % and is nearly common throughout the data-taking periods. The total error in the luminosity was 3.7 % combining these two errors quadratically because they are independent to each other.

3. Monte Carlo statistics

The selection efficiency ε and its statistical error $\Delta\varepsilon$ for the simulated events are given by a binomial distribution as;

$$\varepsilon = \frac{N_{sel}}{N_{prod}}, \qquad \Delta\varepsilon = \sqrt{\frac{N_{sel}(N_{prod}-N_{sel})}{N_{prod}^3}}, \tag{5.3}$$

where N_{sel} is number of the selected events in the produced N_{prod} events. The relative error of $\Delta\varepsilon/\varepsilon$ directly affects the expected number of events. The number of events to be simulated is constrained by the capability of the main computer. Moreover, in fact, the full simulation procedure with detailed detector simulation was not always applied in order to save the CPU time. The full simulation was only applied to the typical combinations of the parameters, one or two points per new particle. The systematic dependences on the parameters were estimated with large statistics using the fast simulation program also described in appendix A. However, since the efficiencies were normalized to the full simulation at the benchmark point, the statistical error of the full simulation commonly remains there.

4. Simulation of hadronization processes

As described in appendix A, we have mainly adopted LUND parton-shower scheme with string fragmentation for QCD correction and subsequent fragmentation processes. Matrix-element scheme of QCD correction was also used to estimate the uncertainty. The model has several parameters to determine the QCD effects, which are correlated to each other. MARK-II group at PEP and TASSO group at PETRA tuned these parameters which are presented also in appendix A,[47] besides the default values suggested by LUND group which we mainly adopted. We estimated the significance of the effect by the deviation of the selection efficiency between them. A typical reaction, that is, in practice t-pair production with mass 28 GeV/c^2 was used in the estimation, where the maximum effect is expected among the new particles in our consideration. Table 5.4 shows the relative deviation of the efficiency ε with each parameter-set to the efficiency ε_0 with default set in the parton-shower model, where each of which has a statistical error of about 2.6 % in the simulation. We found a rise of the efficiency when the parton-shower evolution was turned off in the decay of t-flavored hadrons. Such a operation has the effect to reduce the multiplicity and the spatial extent of final particles and thus, e produced by the decay becomes more isolated.

	parton-shower scheme				matrix-element scheme		
	default	MarkII	TASSO	no shower in decay	default	Mark II	TASSO
$\varepsilon/\varepsilon_0-1$	0	+2.1 %	−1.5 %	+4.7 %	+ 4.3 %	+0.9 %	−0.4 %

Table 5.4 Relative deviation of the efficiency for t-pair production with m_t = 28 GeV/c^2 between the parameter-sets of LUND 7.1, where in "no shower in decay",the parton-shower evolution was disabled in decays of t-flavored hadrons.

5. Decay branching ratios

For the branching ratios of the heavy new particle weakly decaying into e, we have generally assumed that;

$$B(W^* \to e\nu_e) = 11 \pm 1\ \%,$$
$$B(W^* \to ud \text{ or } cs) = 67 \pm 3\ \%. \qquad (5.4)$$

Though the effect of this uncertainty will appear somewhat complicatedly due to the contribution of e from cascade decays, we conservatively estimated the effect simply looking into the prompt e from the new particle.

6. Detector simulation

Though the distributions shown in figures 5.2 to 5.6 may be smeared by the incompleteness of the detector simulation, each selection criterion is sufficiently loose no to lose the designed new particle productions. It is noted that we treat the effect on the e identification separately in the next subsection. If the overall energy calibration of the calorimeters was artificially lowered by 5 % which is the estimated limit of the deviation from the real detector, this manipulation makes negligible effects in the multihadronic selection because we require energetic e in the final sample. For the effect of uncertainties in detector simulation, we adopted the value of 2.7 % for ordinary multihadronic events estimated by Kurashige,[48#] which would be comparable or larger than the value for the new particle production in our consideration.

We also used a fast detector simulation program described in appendix A to evaluate systematic dependences of the efficiencies of the new particles on various parameters in the models. Since the systematics from the detector simulation is expected to be common for events with similar event topology, it should be mostly canceled out in estimating such relative variations as parameter dependences. For the remaining systematic error from the fast detector simulation, we put 3 % which came from the deviation between the fast simulation and the full simulation for t-pair event with t-quark mass of 28 GeV/c^2 as a typical new particle production. The absolute efficiencies were normalized to those by the full simulation at certain points in studying the parameter dependences.

Therefore, two uncertainties from the full simulation and from the fast simulation are included in the calculated efficiency. The total systematic error of the efficiency from the detector simulation was estimated to 4 % which is a quadratic sum of these two errors.

7. Electron identification

Since the isolated e can be treated as a single track, the efficiency to identify e was estimated both by Monte Carlo simulation and by the real e sample directly. The deviation of the two estimations in the relevant momentum region amounted relatively within 6 % as shown in figure 4.10, which was also included into the systematic error.

5.4.3. Constraints on new particles

We could not find an indication of the new particle production. Instead we put some constraints on new particles. Actually, we have obtained more strict lower mass limits than those from PEP/PETRA results.

The cut-off values of the selection criteria were generally placed at the steep tail-ends in the distributions of the background ordinary processes. Since the efficiency for the background was determined mainly by the contribution near the cut-off point, a small error of the simulation, which may smear the distribution, may lead to a large error in the selection efficiency for the background events. And also the tail distribution is intrinsically hard to reproduce reliably. Therefore, in evaluating the constraints on the new particles, the selected one event was considered to be a signal and no background-subtraction was made conservatively. The fact that we observed one event excludes the reaction which yields more than 4.74 events in average at 95 % confidence level by Poisson statistics. This number was taken to be the upper limit of observable signals for each search of new particle.

1. Third generation up-type quark t

The efficiency to detect isolated e in t-pair production is nearly constant for the t mass more than 25 GeV/c^2 as shown in figure 5.8 (a) with $\sqrt{s}$ = 60 GeV, for example. Since we took the minimum efficiency in the mass range, the mass dependence of the expected number of events from t-pair production reflects simply its total cross section. Figure 5.8 (b) shows the expected number of events, where the horizontal line represents the upper bound of allowable yield. We found that t-quark must be heavier than 29.5 GeV/c^2 with 95 % confidence level.

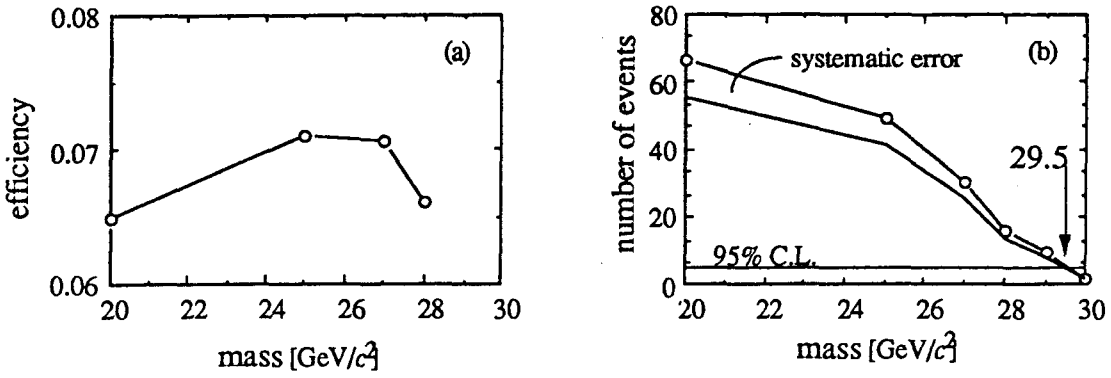

Figure 5.8 (a) Efficiency and (b) expected number of events for t-pair production where the line with points shows the expected value and another line below is lower bound subtracting the systematic error.

2. Fourth generation down-type quark b'

The total cross section of b'-pair production is smaller than t-quark case by factor 1/4 in QED calculation. In this thesis, b'-flavored hadrons were assumed to decay always into c-jet, virtual W-boson, and a spectator-jet in the same way as t-flavored hadron decays into b-jet, virtual W-boson, and a spectator jet. The difference between c-jet and b-jet appears in multiplicity of final particles but dose not drastically influence the efficiency in this analysis, because we are looking into e from virtual W-boson. We found the efficiency for b'-quark to be slightly better than for t-quark. The main difference between these events appears in the multiplicity of final particles. While t decays as $t \rightarrow b \rightarrow c \rightarrow s,d$ with yielding many hadrons in the three cascade decays, b' decays with two steps as $b' \rightarrow c \rightarrow s,d$ with less mean multiplicity than t. The discrepancy between the efficiencies as shown in in figures 5.8 (a) and 5.9 (a) can be well understood by the fact, that is, e tends to be more isolated in the event with less multiplicity. Figure 5.9 (b) shows the expected number of events from b'-pair production and from this, the existence of b'-quark with mass less than 28.0 GeV/c^2 was excluded.

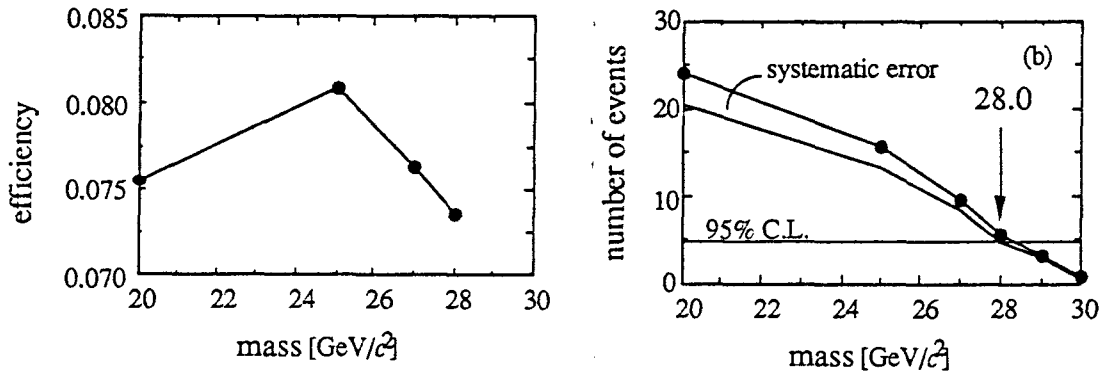

Figure 5.9 (a) Efficiency and (b) expected number of events for b'-pair production.

3. Unstable heavy neutrino N

Here we concentrate on the extreme case where the heavy fourth neutrino N dominantly decays into e. Namely, we assumed for the mixing matrix that;

$$|U_{Ne}|^2 \gg |U_{N\mu}|^2 + |U_{N\tau}|^2. \tag{5.5}$$

Figure 5.10 shows the expected number of events of short-lived N production, where the existence of short-lived N with dominant N-e coupling in the mass range 9.0 to 28.5 GeV/c^2 was excluded. For the long-lived case, the detection efficiency of N production decreases because tracks from the decay vertex distant from the colliding point usually do not satisfy the good track condition. We have actually evaluated the efficiencies for various masses and life-times using the fast simulation program. The critical cut-off parameter in this case is $R_{min} < 2.0$ cm, which CDC can measure with resolution within 2 mm. Because the R_{min} calculation from the generator information was also included with smearing by the resolution in the fast simulation program, we can evaluate the degradation by the flight correctly. Since the life-time of the decay is in inverse ratio to $|U_{Ne}|^2$, we can draw the exclusion contour of m_N versus $|U_{Ne}|^2$ with 95 % confidence level as shown in figure 5.11.

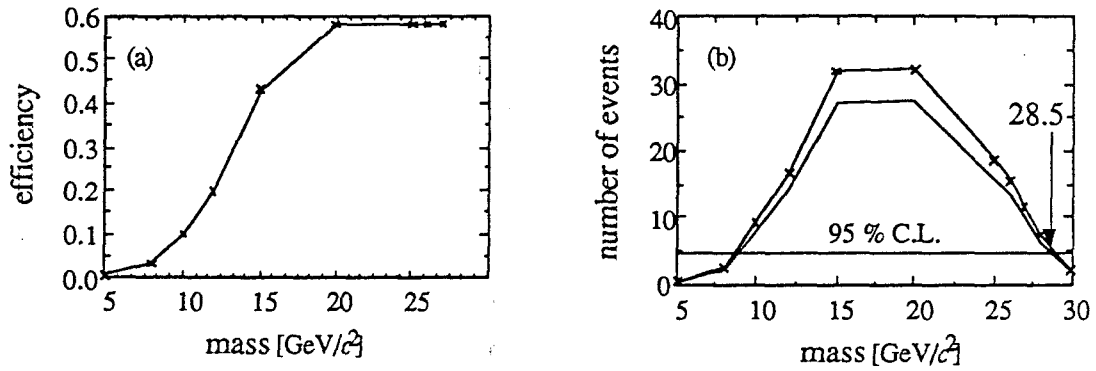

Figure 5.10 (a) Efficiency and (b) expected number of events for short-lived N-pair production.

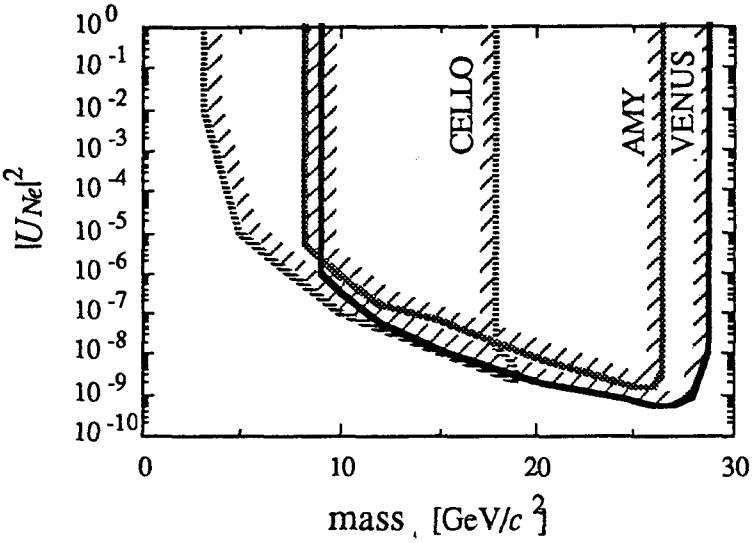

Figure 5.11 Exclusion contour of mass versus mixing parameter with 95 % confidence level ignoring N-μ and N-τ couplings.

4. Electron-type neutral heavy lepton E^0

We have considered the extreme case in which the coupling structure of e-E^0-W vertex is V+A type or V–A type. The difference between the two cases mainly appears in total cross section. The angular distribution become less important as m_E increases since the boost toward the production direction of E^0 becomes smaller. Figure 5.12 shows the efficiency and the expected numbers of events each for the two cases. We have excluded single production of new neutral heavy lepton weakly coupled to e with mass up to 54.0 (51.5) GeV/c^2 for V+A (V–A) case.

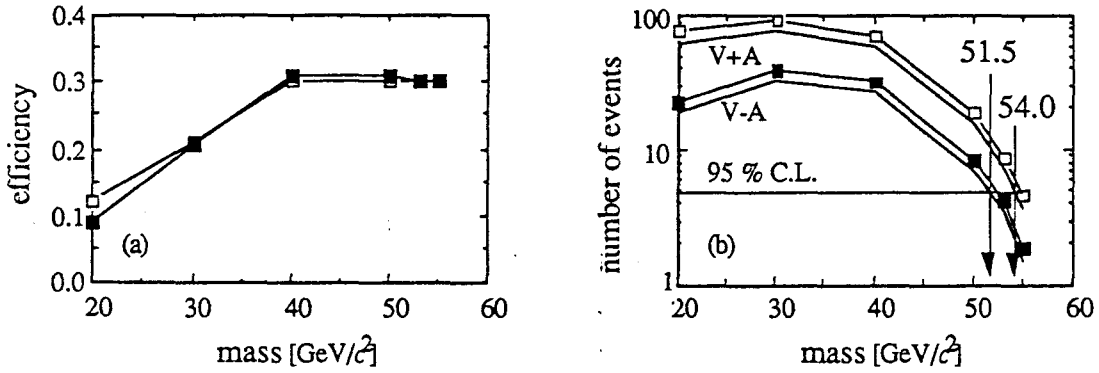

Figure 5.12 Efficiency and expected number of events for E^0 production.

5. First generation leptoquark χ

We have considered two models, $|Q_\chi| = 2/3$ and 1/3. This difference, namely whether e couples to $\bar{d}$ or u, appears only in total cross section. As both models allow χ to decay into eq and $\nu_e q$, there will be three types of final states, namely, including two e's or one e and one ν_e (missing) or two ν_e's as shown in figure 5.13. This analysis

has no sensitivity for the ν_e-ν_e mode. The selection efficiency is higher for e-e mode than for e-ν_e mode because of richer yield of e. Figure 5.14 (a) shows the efficiency for the e-e mode and for the e-ν_e mode. Using these efficiencies and fixing the branching ratio, we can expect the number of events to be selected as shown in figure 5.14 (b), where the branching ratio is fixed to $B(\chi \rightarrow eq) = 0.5$ for both cases, $|Q| = 2/3$ and 1/3. Assuming $B(\chi \rightarrow eq) = 0.5$, we have excluded first generation leptoquark with $|Q_\chi| = 2/3$ (1/3) in the mass range 4.0 to 26.0 (6.0 to 22.5) GeV/c^2. More generally, we can draw the exclusion contours of m_χ versus $B(\chi \rightarrow eq)$ as shown in figure 5.15. As was already described in chapter 1, the strength of e-q-χ coupling determines the life-time of χ which affects the efficiency. We have assured that the efficiency is nearly constant in the region $\lambda_e^2 > 10^{-13}$.

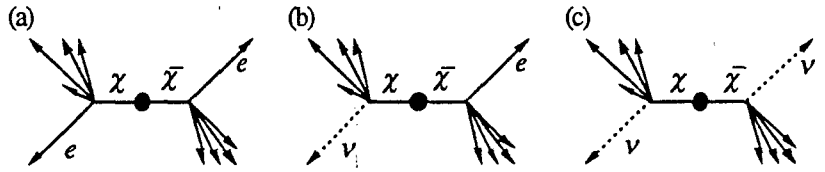

Figure 5.13 Three types of decay signatures in χ-pair production, (a) e-e mode, (b) e-ν mode, and (c) ν–ν mode.

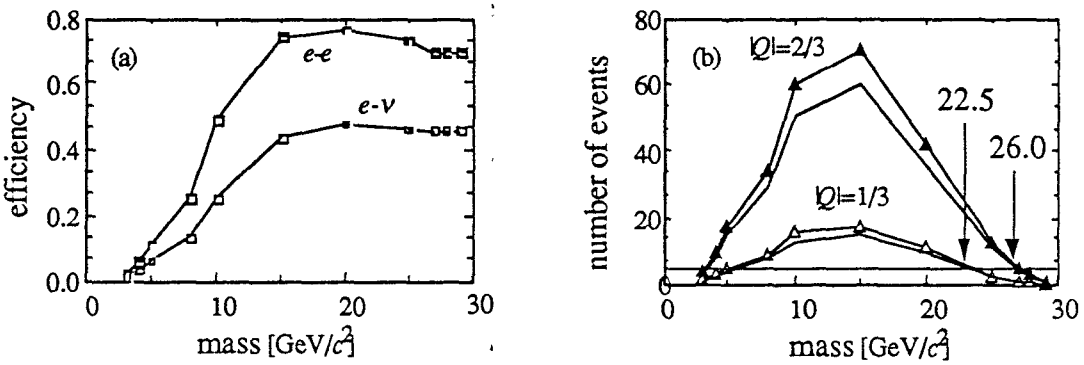

Figure 5.14 (a) Efficiencies for two final states from a leptoquark-pair production (e-e mode and e-ν_e mode) and (b) the expected numbers of events for $|Q|$=1/3 and 2/3 cases both with assuming $B(\chi \rightarrow eq)$=0.5.

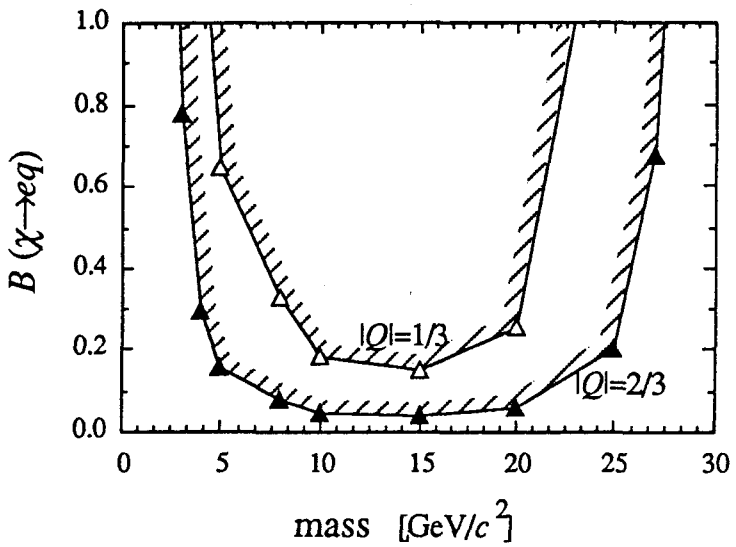

Figure 5.15 Exclusion contour of mass versus branching ratio to e with 95 % confidence level for χ-pair production with $|Q|=1/3$ (white triangle) and for one with $|Q|=2/3$ case (black triangle).

Chapter 6 Conclusion

We have searched for new particles looking into electron-inclusive multihadronic signature in e^+e^- collision, which is a characteristic final state for the production of many new heavy particles including new quarks and new leptons and a leptoquark. Among them, new quarks, t-quark and b'-quark which were suggested by a natural extension of the standard model, were the most likely targets. A new heavy neutrino which belongs to a weak doublet with the mixing between lepton flavors and also a right handed partner of the electron were our next objects. Finally, a leptoquark, a particle possessing both a color and a lepton number, which is naturally expected in unifying quarks and leptons, was investigated.

Events were selected from the multihadronic event sample, subsequently with requirements to be of low thrust and to include an energetic and isolated electron. No excess of events were observed. The remaining one event was consistent with expectation from ordinary quark production and the result was interpreted to set new constraints on them. To be conservative, no subtraction of the background was made. Table 6.1 summarizes the obtained lower mass limits with 95 % confidence level for the particles we have searched for.

new particle			this search	published limits	
sign	specification	gen. #		PETRA	TRISTAN
t	up-type quark	3	29.5	23.3^{M}	30.2^{V}
b'	down-type quark	4	28.0	22.7^{M}	28.2^{V}
N	unstable neutrino	4	28.5	18.0^{C}	26.5^{A}
E^0	neutral lepton (V+A)	1	54.0	37.4^{C}	none
E^0	neutral lepton (V–A)	1	51.5	34.6^{C}	none
χ	leptoquark ($\|Q\|$=1/3)	1	22.5	none	none
γ	leptoquark ($\|Q\|$=2/3)	1	26.0	none	none

Table 6.1 Obtained lower mass limits of new particles in GeV/c^2 and published limits by Dec. 1989, where N was assumed to decay always into e with short lifetime and the branching ratio of the decay of the leptoquark into an electron and a quark was assumed to be 50 %. These values are from ^{M}Mark-J, ^{C}CELLO, ^{V}VENUS, ^{A}AMY.

Appendix A Monte Carlo Simulation

A.1. Framework of event simulation

Data analysis is performed by comparing with the expectation from theoretical models. An event generator simulates particle productions based on the models. We mainly used LUND programs in an event generator of the new particle. It outputs four-momentum informations of the produced particles. Because some informations are inevitably lost in reconstruction, a simulation of the detector performance must be included in order to compare data with Monte Carlo directly. We have two kinds of programs. For a complete analysis, we used the full detector simulation program, VMONT, which simulates the particle behaviors in VENUS detector and the responses of the detector are produced. As VMONT outputs the detector responses in the same format as the real data, the tracks and the clusters in the Monte Carlo events can be reconstructed in quite the same way as the real data. For quick analysis, the fast simulation program was used, which directly produces the expected tracks and clusters for given particles simply by smearing their four-momenta from a event generator. Figure A.1 shows the flow-chart of an analysis using Monte Carlo simulation.

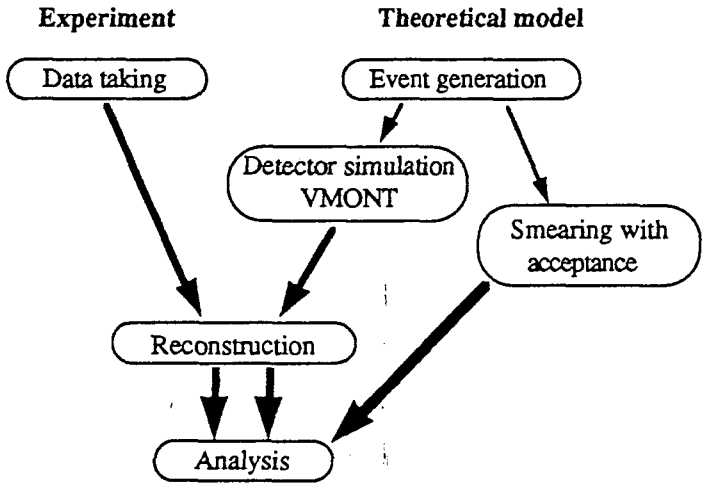

Figure A.1 Flow-chart of the analysis procedure.

A.2. Event generation

A.2.1. Quark-pair production

LUND Monte Carlo is by now a fairly old and well established program.[48] The program package for jet fragmentation and e^+e^- physics, named JETSET, is a popular

event generator of multihadronic events at e^+e^- colliding experiments. Eight quarks of four generations are originally supported. Two versions, JETSET 6.3 and JETSET 7.1, were used in this analysis. The difference between them is very small. Version 7.1 includes all the possible treatments in version 6.3. Their common features are described here.

The productions of a quark and its antiquark are calculated according to the electroweak theory with radiative and QCD corrections. The radiative correction is performed according to the scheme by Berends, Kleiss, and Jadach as described in appendix B.

The QCD correction is usually performed by parton shower model (PS) with leading logarithmic approximation. In this scheme, a parton shower develops by successive processes of $q \to qg$, $\bar{q} \to \bar{q}g$, $g \to gg$, and $g \to q\bar{q}$ as shown in figure A.2. The probability for these reactions are proportional to α_s which is determined by QCD scale parameter Λ. Since the perturbative treatment becomes impossible in low q^2 region, the cut-off parameter Q_0 for the invariant mass is imposed in these emissions. The parton-shower develops until the virtual mass of any parton becomes lighter than Q_0.

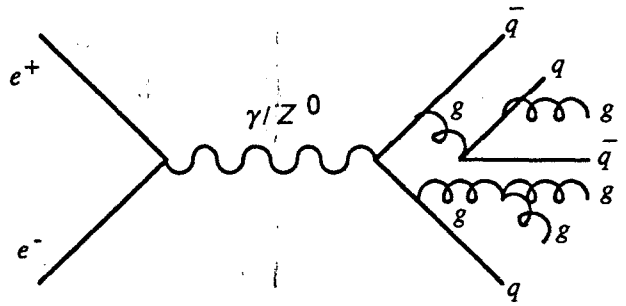

Figure A.2 QCD correction by parton shower model.

Besides the parton-shower model, an alternative correction by tree-level calculation of the QCD matrix elements (ME) up to α_s^2-order is also possible. In calculating the matrix elements, a cut-off parameter $y_{min} = (M_{ij}/s)_{min}$, the minimum scaled invariant mass between two partons i and j, is introduced. These diagrams are shown in figure A.3. The main difference from PS scheme appears in the fraction of multijet events, because ME can not reproduce more than four jets in principle.

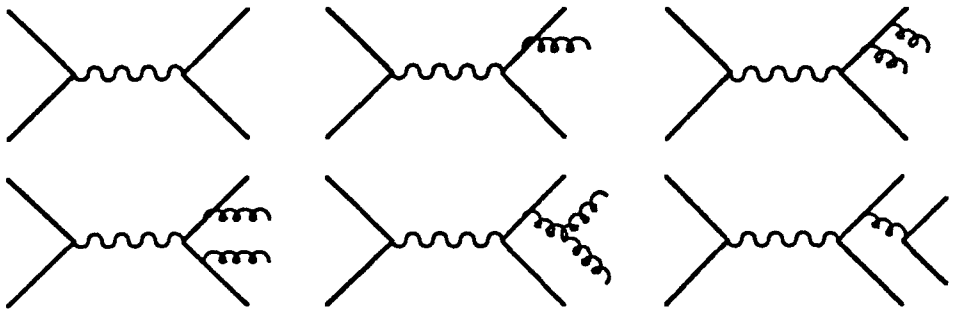

Figure A.3 Tree-level QCD diagrams up to second order of α_s.

Non-Abelian nature of QCD disables a perturbative approach in low q^2 region, where partons fragment into hadrons. The phenomenological models are used in the fragmentation processes. The string fragmentation model is based on the dynamics of string. Between the partons in a color-singlet system, a one-dimensional string is placed, where a quark is located at the end-point and a gluon is located at the intermediate point to be a kink as shown in figure A.4. The relative momentum between the partons determines the tension. The tension breaks the string with generating quark-antiquark pairs at the breaking point. The original parton brings one of the pair and forms a hadron (meson). The scaled longitudinal momentum of the hadron, $z = p_{hadron}/p_{parton}$, with respect to the direction of the parton is given by a fragmentation function. LUND symmetric function has two parameters, a and b;

$$f(z) = \frac{(1-z)^a}{z} \exp\left(-\frac{bm_T^2}{z}\right), \tag{A.1}$$

where $m_T = \sqrt{m^2+p_T^2}$ is the transverse mass of the produced hadron. The transverse momentum of the hadron, p_T, is produced independently by Gaussian distribution with standard deviation σ_q. The breaking of the string is repeated as far as the string has enough energy to generate a quark-antiquark pair. Baryons can be also produced by replacing the quark-antiquark pair by a diquark-antidiquark pair.

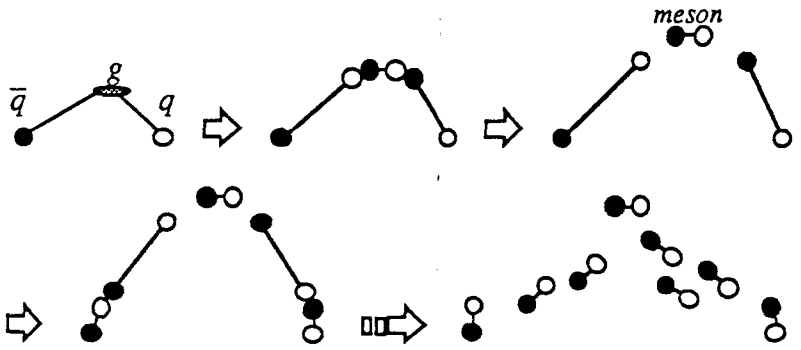

Figure A.4 String fragmentation scheme of multihadron production.

As was described above, there are some parameters to determine the effects of QCD and fragmentation. Because they are correlated one another, they should be

treated as a parameter-set. As shown in table A.1, these parameters were tuned by prior experimental groups,[49] in addition to the original default values.

PS	default	MarkII	TASSO	ME	default	Mark II	TASSO
Λ [GeV]	0.4	0.4	0.26	Λ [GeV]	0.5	0.5	0.62
Q_0 [GeV]	1.0	1.0	1.0	y_{min}	0.02	0.015	0.02
a	0.5	0.45	0.18	a	1.0	0.9	0.58
b [GeV^{-2}]	0.9	0.90	0.34	b [GeV^{-2}]	0.7	0.70	0.41
σ_q [GeV]	0.35	0.33	0.39	σ_q [GeV]	0.4	0.33	0.40

Table A.1 The tuned parameter-sets for the parton shower scheme (PS), and for the matrix element scheme (ME), where the default values are originally given in the programs, JETSET 6.3 (PS) and JETSET 5.3 (ME).

LUND program also supports decays of unstable particles. A pair of quarks from virtual W-boson in heavy quark decays also develops a parton shower in version 7.1 quite in the same way as in the production while in version 6.3, hadrons are directly fragmented from the two quarks without perturbative QCD corrections. Except for this, there is no significant modification which influences this analysis.

A.2.2. Two-photon-exchange interaction

In two-photon-exchange interaction, the event with outgoing e in the central region of the detector is particularly important in this analysis. But actually, such a event rarely occurs. In order to conserve the CPU time, the event generator with a tagging angle cut for the outgoing e, developed by Berends *et al.*,[50] is used. The original program is a $e^+e^-\mu^+\mu^-$ generator and the modification to a $e^+e^-q\bar{q}$ generator was made. The mass and the charge of μ were replaced with those of a quark. This generator includes all the α^4-order QED diagrams as shown in chapter 1. The outgoing four particles are then treated by LUND program, where partons are fragmented into hadrons and unstable particles decay.

A.2.3. New particles

We coded the programs which treat the new particle productions given in chapter 1 of the text. Fragmentations and decays were performed by LUND program, mainly JETSET version 7.1. We believe it better because QCD correction by parton shower evolution is included also in decays.

A.3. Detector simulation

A.3.1. Full detector simulation program

A detector simulation program, VMONT, simulates the responses of VENUS detector in fine steps. VMONT accepts four-momenta of final particles which were produced by an event generator. The particles are traced in the detector, where they undergo various processes including decays of long-lived particles, multiple Coulomb scattering, bremsstrahlung, pair-conversion, Compton scattering, and energy loss. Hadron absorption effect by nuclear interactions is also included. The expected responses are converted into the same format as the real data, such as drift time, energy deposit, time of flight, etc. The resolution of each detector part was tuned so as to reproduce the realistic response. Electromagnetic showers in the calorimeters are simulated by EGS program,[51] and hadron responses are simulated by empirical functions obtained by the test-beam as described in appendix C.

A.3.2. Fast detector simulation program

VMONT is so much time-consuming because it traces the particles with fine steps. The CPU time typically amounted about 3 seconds to simulate one multihadronic event with a main-frame computer, FACOM-M780. Moreover, it is necessary to "reconstruct" the particles from the detector responses in quite the same way as actual data, which also takes about 2 seconds for a multihadronic event. For the purpose of systematic evaluation where large statistics is needed, we developed a rough but fast simulation program where track and cluster informations are directly produced from the input four-momenta informations. A charged particle expected to leave hit points in CDC is recognized as a track with its momentum smeared according to the expected resolution. The track parameters which can be calculated by input four-vectors, such as R_{min}, Z_{min}, etc. in the text are reproduced by the program. Particles expected to inject into the calorimeter is recognized as a cluster of which energies are smeared by the empirical functions in the same way as in VMONT. For the estimation of systematic dependences on parameters which are not sensitive to detector simulation, we utilized this fast simulation program. For a detailed analysis which is essentially affected by detector simulation, such as particle identification, this fast simulation program can not reproduce the responses with required accuracy. Since we know the source of the reconstructed tracks in the simulation, we applied the e identification efficiency to the produced e in the simulation, directly without any identification procedure. The efficiency for an isolated e was estimated both by the real data and by VMONT as was described in chapter 4 of the text, where we adopted one by data. Since we are looking

only into an isolated e, e's in a jet and the contamination of misidentified hadrons were ignored.

Appendix B Radiative correction

B.1. Significance of the higher order effect

We must evaluate the expectation value of the particle production of our interest as exactly as possible. The higher order effect, which is called radiative correction, is important because this effect in total cross section is expected typically to be a few tens of percent in total cross section. Because the magnitude of the correction decreases with the order of coupling, we can neglect the contributions beyond the second order. In practice, it is very difficult to include more complicated diagrams.

B.2. Radiative correction to γ/Z^0 annihilation processes

We have adopted the correction procedure developed by Berends, Kleiss, and Jadach,[52] for the Monte Carlo simulations of the pair-production processes *via* γ/Z^0 annihilation, where diagrams shown in figure B.1, so-called vertex correction, vacuum polarization, and initial-state radiation are included.

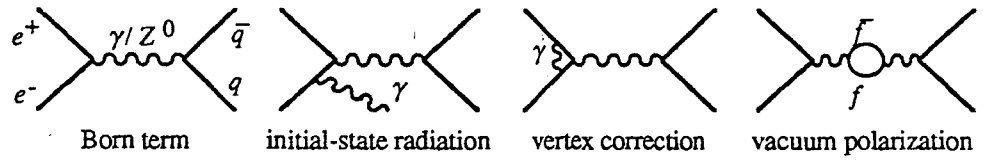

Figure B.1 Radiative diagrams included in the correction by Berends-Kleiss-Jadach.

The lowest order cross section σ_0 should be corrected into σ as follows ignoring the threshold effect due to the mass of the final particle;

$$\sigma = (1+\delta)\,\sigma_0 \tag{B.1}$$

$$\delta = \delta_{vertex} + \delta_{vacuum} + \delta_{soft} + \delta_{hard},$$

where δ_{vertex}, δ_{vacuum}, δ_{soft}, and δ_{hard} are effects of vertex correction, vacuum polarization, soft initial-state radiation, and hard initial-state radiation, respectively. The energy spectrum of the "hard" radiation is limited to avoid the divergence in infra-red region, where the correction was performed by the "soft" part neglecting real γ emission. The cut-off on the scaled energy of the γ, $k_{min} = (E_\gamma/E_{beam})_{\min}$, is normally set to 0.01. The maximum energy of the "hard" γ should be determined by the mass of the produced particle but we normally set the upper limit, $k_{max} = 0.99$, for light particles. The magnitudes of these corrections to five-flavor quark-pair productions at $\sqrt{s}$ = 60 GeV are calculated to be, $\delta_{vertex} = 0.0844$, $\delta_{vacuum} = 0.0845$, $\delta_{soft} = -0.4793$, and

δ_{hard} = 0.5654. This leads the total cross section to increase 25.5 %. However, in particular for a heavy particle production, this effect of hard radiation is not correct because it enhances the threshold effect which amounts to $\beta(3-\beta^2)/2$ for a fermion-pair production or β^3 for a scalar-pair production, where β is the velocity of the particle in the center of mass system of the pair. The effect of hard radiation is corrected by Monte Carlo integration in the same way as in the next section.

B.3. Basic correction of initial-state radiation

The radiative correction by Berends *et al.* is applicable only to γ/Z^0 annihilation processes. For any heavy particle production near its threshold, initial-state radiation is the most significant correction. In order to calculate the effect in searching for electron-type neutral heavy lepton which is a W exchange process, we adopted a naive correction of initial-state radiation by Etim, Pancheri, and Touschek,[53] which was based on the semiclassical electromagnetic dynamics. The radiative process is approximated by a model where a real γ is emitted from the initial e independently followed by the e^+e^- collision with reduced center of mass energy. The corrected cross section is given by the averaging integration;

$$\sigma(s) = \int \sigma_0(s-ks)\rho(k)\mathrm{d}^3k, \tag{B.2}$$

where σ_0 is the lowest order cross section, $k \equiv |\boldsymbol{k}|$ is the γ energy divided by the beam energy, and $\rho(k)$ expresses a probability to emit γ with scaled energy k. A calculation of semiclassical electrodynamics leads to number of emitted γ's per event as;

$$\mathrm{d}n = \frac{4\alpha\beta^2}{(2\pi)^2}\frac{\mathrm{d}k}{k}\frac{\sin^2\theta_k}{(1-\beta^2\cos^2\theta_k)^2}\,\mathrm{d}\cos\theta_k\,\mathrm{d}\phi_k, \tag{B.3}$$

where β is the velocity of the initial e, and θ_k and ϕ_k represent the direction of the emitted γ. The integration over θ_k and ϕ_k yields;

$$n(k) \equiv \frac{\mathrm{d}n}{\mathrm{d}k} = \frac{\xi}{k}, \tag{B.4}$$

where ξ is given by;

$$\begin{aligned}\xi &= \frac{2\alpha\beta^2}{\pi}\int_{-1}^{+1}\frac{1-x^2}{(1-\beta^2x^2)^2}\mathrm{d}x = \frac{\alpha\beta^2}{\pi}\left[\frac{1+\beta^2}{\beta}\ln\left(\frac{1+\beta}{1-\beta}\right)-2\right] \\ &\approx \frac{2\alpha}{\pi}\left[\ln\left(\frac{s}{m_e^2}\right)-1\right] \qquad (\beta\to 1)\end{aligned} \tag{B.5}$$

If multiple radiation in a collision is neglected, the number-density $n(k)$ is equivalent to the probability-density $\rho(k)$. The integration of $n(k)$ over k, corresponding to the number of γ's in a event, however diverges in infra-red region. Because the correction

to the cross section, $(\sigma_0(s-ks)-\sigma_0(s))/\sigma_0(s)$, is very small in the infra-red region of $k \approx 0$, we can remove the infra-red divergence by setting the cut-off parameter k_{min}. In order to minimize the error, k_{min} must be chosen properly to satisfy the following relations;

$$\sigma_0(s) \approx \sigma_0(s-k_{min}s), \qquad \int_{k_{min}}^{+1} n(k)\mathrm{d}k \ll 1. \tag{B.6}$$

Here virtual corrections such as vacuum polarization and vertex correction are not included. This uncertainty was treated as a systematic error of production cross section in this analysis.

Appendix C Parametrization of Hadron Responses of VENUS Lead-glass Calorimeter

C.1. Hadron responses

In Monte Carlo simulation of detector-responses, it is so much difficult to describe complicated interaction of hadrons in matter. There are some program packages which treats the interactions generally. However, it is required to tune them in order to obtain the realistic responses of the detector. The precise simulation of a hadronic shower in a calorimeter is not so much important for the standard analysis with VENUS detector and we decided to parametrize the responses with empirical functions obtained at a beam-test, where the calorimeter components were exposed to pion beam with known momentum.

Hadron responses of a calorimeter have two aspects attributed to two processes, namely minimum-ionizing penetration and inelastic interaction. The most important subject is to reproduce a realistic energy response for a hadron. However, the sharing of the energy among the calorimeter modules is so much difficult a subject in parametrization.

C.2. Experimental set-up of the beam-test

We studied the response of lead-glass counters for pions which were installed in VENUS detector. The beam was operated in three periods, October 1987, November 1987, and March 1988 at $\pi 2$ beam-line of KEK 12 GeV proton synchrotron. This beam-test also intended to study transition radiation detector (TRD) for the use in VENUS detector. The experimental layout is shown in figure C.1. Pions and electrons were produced at the internal target and the component with fixed momentum were extracted to the beam-line by a bending magnet. The variation of momentum was 1, 2, 3, and 4 GeV/c and the typical intensities were 5 KHz and 40 Hz for pions and electrons, respectively, where the electron beam was used for calibration.

Pions and electrons were identified by two gas Cerenkov counters, C1 and C2. The beam is defined to 1 cm × 1 cm by two sets of two trigger counters, T1-T2 and T3-T4. Two anti-counters, V1 and V2, were placed in order to reject simultaneous hit of other particle in horizontal direction. In vertical direction, two drift chambers, D1 and D2, each of which had four sense wires horizontally strung, were used for rejection of multi-particle events. TRD is also used to reject electrons in the pion beam. The typical

size of the lead-glass counters is 11 cm x 12 cm in cross section and 30 cm in depth which corresponds to 18 radiation lengths or 1 nuclear interaction length. A 3-inch phototube is attached at the center of the counter through a plastic light-guide of 6 cm long. As shown in figure C.2, 3×3 counters (Oct, Nov-1987) or 2×2 counters corresponding to modules 1, 2, 4, and 5 (Mar-1988) are mounted with 1.5 mm spacing on a movable table. As also shown in this figure, the beam incident point into the lead-glass was moved in order to study position dependence of the response. Energy deposit in each counter was measured by a charge-sensitive ADC.

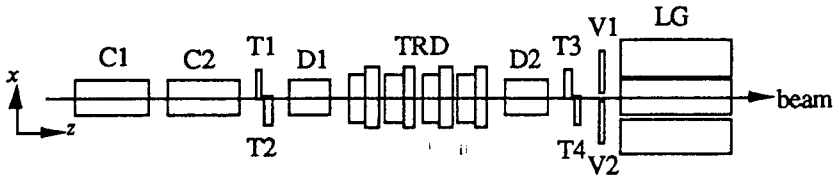

Figure C.1 Experimental layout at the beam-test.

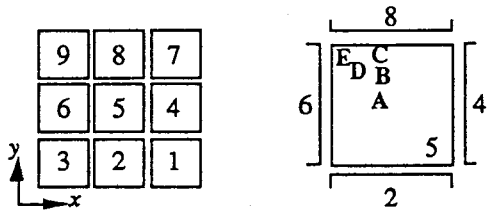

Figure C.2 Alignment of the lead-glass array at the beam-test.

C.3. Total energy distribution and its parametrization

The total energy E is the sum of the energies detected in the counter array. The black circles with error bars in figures C.3 shows E/p spectra for p = 2 GeV/c pions which were injected into the center of the central counter, namely point A in figure C.2, and near the edge, namely point C. Two features are noted here. First, the minimum ionizing peak produced by a penetrating pion for case A appears at about 600 MeV while it is about 200 MeV for case C. This is due to the additional Cerenkov light emitted by pions penetrating in the light-guide. Second, the spectrum of pion response caused by inelastic interaction extends far from the incident energy. This is also understood by the effect of light-guide, that is, the pion-induced shower may extend to the light-guide and produce additional Cerenkov light while the electron-induced shower is mostly contained in the lead-glass. Because the light-guide is attached directly to the phototube, the light emitted in the light-guide is enhanced by several times of the light in the lead-glass.

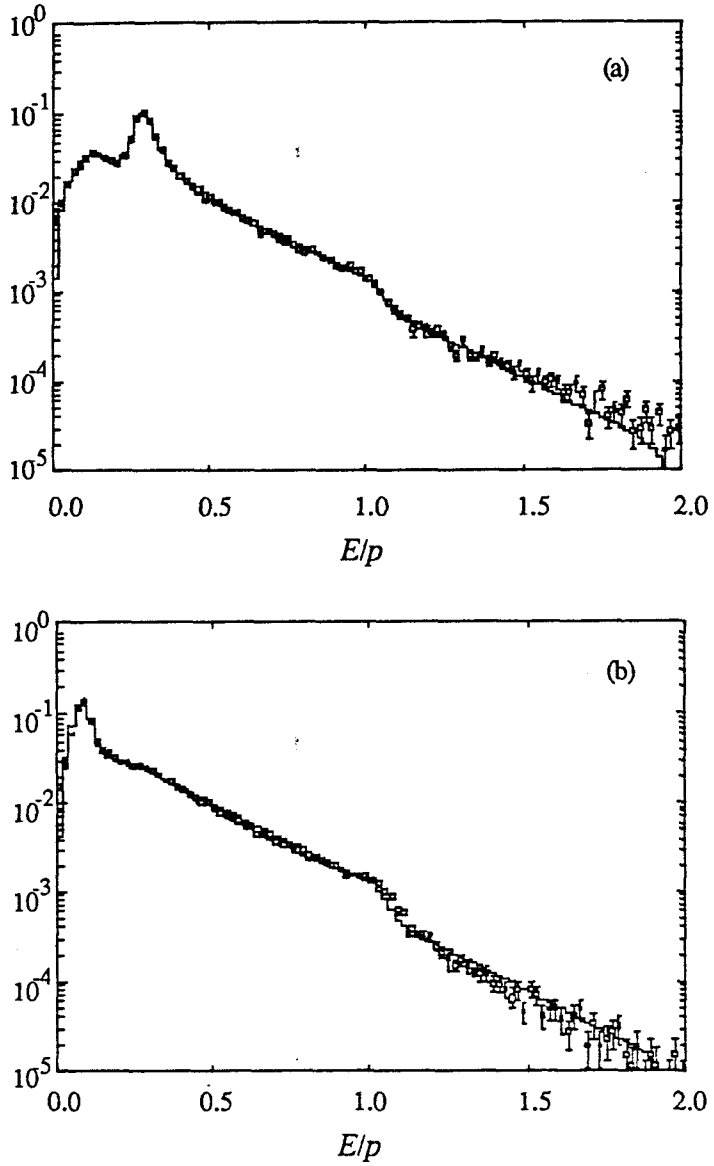

Figure C.3 Total energy spectrum of the pion beam with momentum of 2 GeV/*c* (squares with error bars) and the reproduced one (histogram), where the beam is incident at (a) point A or (b) point C in figure C.2.

We parametrized the total energy distribution for hadrons, separating the contributions of;

(1) the incident minimum-ionizing hadron in the lead-glass,

(2) the hadronic shower produced by inelastic nuclear interaction, and

(3) the additional light in the light-guide by a penetrating particle.

These contributions are added into the total energy, where (2) and (3) cannot appear simultaneously. The response for hadrons is reproduced according to this scheme, where the path and the incident position into the calorimeter module are given by the event generator.

First, the path-length in the lead-glass till the inelastic interaction occurs, d, is decided by random number with the exponential distribution;

$$f_d(d) = \frac{1}{\lambda}\exp\left(-\frac{d}{\lambda}\right), \tag{C.1}$$

where λ is a nuclear interaction length of the lead-glass. If d exceeds the maximum path-length, corresponding to the penetrating case, d is set to the path-length in the lead-glass. Muons and about 1/3 of hadrons are expected to penetrate the lead-glass. The contribution of Cerenkov light in the lead-glass before the interaction, E_m, is produced by Gaussian distribution for charged particles;

$$f_m(E_m) = \frac{1}{\sqrt{2\pi}\sigma_m\sqrt{\mu_m d}}\exp\left(-\frac{(E_m-\mu_m d)^2}{2\sigma_m{}^2\mu_m d}\right), \tag{C.2}$$

where μ_m is the mean contribution to E per unit path-length in the lead-glass and $\sigma_m\sqrt{\mu_m d}$ corresponds to a standard deviation of the distribution.

The contribution of the hadronic shower for the inelastically interacted hadron,E_i, is produced by the following spectrum;

$$f_i(E_i) = \frac{\varepsilon}{1+\gamma(E_i/p)^{-\beta}}\cdot\exp\left(-\alpha E_i/p\right). \tag{C.3}$$

The exponential behavior in high energy region, for which no dependence on p was observed, is determined by constant α and the rise in low energy region is determined by parameters β and γ, both of which depend on p as follows;

$$(\beta,\gamma) = \begin{cases} (\beta_1,\gamma_1) & (p < 1.5) \\ (\beta_2,\gamma_2) & (1.5 < p < 2.5) \\ (\beta_3,\gamma_3) & (2.5 < p < 3.5) \\ (\beta_4,\gamma_4) & (3.5 < p), \end{cases} \tag{C.4}$$

The energy to be generated is limited in the range $E_i/p < 2$ and in order to reproduce the observed kink at $E_i/p \approx 1$, the probability to generate the response with $E_i/p > \delta \approx 1$ is suppressed by parameter ε which is a function of the lateral distance from the center of the light-guide because this high energy response is due to the light-guide, namely;

$$\varepsilon = \begin{cases} 1 & (E_i/p < \delta) \\ \varepsilon_1-\varepsilon_2\sqrt{x^2+y^2} & (\delta < E_i/p < 2) \\ 0 & (E_i/p > 2). \end{cases} \tag{C.5}$$

For charged particles penetrating the light-guide, the contribution of the additional Cerenkov light, E_l, is reproduced by Landau distribution;

$$f_l(E_l) = \exp\left[-\frac{1}{2}\left\{\frac{E_l-\mu_l d_l}{\sigma_l\sqrt{\mu_l d_l}}+\exp\left(-\frac{E_l-\mu_l d_l}{\sigma_l\sqrt{\mu_l d_l}}\right)\right\}\right], \tag{C.6}$$

where μ_l is the mean energy per unit path-length in the light-guide and $\sigma_l\sqrt{\mu_l d_l}$ determines the width of the spectrum. The path-length in the light-guide, d_l, is given by the spatial information of the particle and geometry of the calorimeter. The probability to pass through the light-guide for a penetrating particle is about 1/3.

The interaction length λ is calculated from the ingredients of the lead-glass,[54] which is actually consistent with the experimental data. Parameters α, β's, γ's, δ, ε_1, ε_2, μ_m, σ_m, μ_l, and σ_l were determined by minimizing χ^2 between the real distribution obtained at the beam-test and the reproduced one after smearing by the resolution of (6 %)/$\sqrt{E}$. The parameters are fixed mainly using the data of the beam with p = 2 GeV/c. First, the parameters, μ_m and σ_m for the minimum-ionizing peak, α, β_2, and γ_2 for inelastic interactions, and δ and ε_1 for the suppression of high energy response, were fixed by the fit using the point C data, where the contribution of the light-guide did not exist. Then, the parameters for the light-guide effect, μ_l, σ_l, and ε_2 were fixed using the point A data. Using the data of p = 1, 3, and 4 GeV/c, the other β's and γ's were fixed. The reproduced spectra are also shown in figure C.3.

However, the minimum-ionizing peak in cosmic-ray events and in multi-hadronic events in VENUS experiment is placed at higher energy and is broader than that in the beam-test. This can be well understood by an optical effect. The acceptance of light into the light-guide depends on the injection angle because the refractive index of the light-guide is smaller than that of the lead-glass. The injection angle of the test-beam was fixed nearly perpendicular to the front-face of the lead-glass, which gives the minimum response in energy. Therefore, parameters μ_m and σ_m were determined to reproduce the peak for particles in multihadronic events. The fixed values of the parameters are shown in table C.1.

α	4.06	δ	1.06
β_1	0.628	γ_1	0.0985
β_2	0.731	γ_2	0.161
β_3	0.928	γ_3	0.153
β_4	1.271	γ_4	0.0809
ε_1	0.65	ε_2	0.03 [cm^{-1}]
μ_m	8.0 [MeV/cm]	σ_m	2.6 [MeV$^{1/2}$]
μ_l	65 [MeV/cm]	σ_l	2.0 [MeV$^{1/2}$]

Table C.1 Fixed values of the parameters for energy responses of hadrons.

C.4. Parametrization of energy-sharing

As the nuclear interaction length of the lead-glass is comparable with the counter dimension, hadronic showers tend to extend over the lead-glass modules irregularly, sometimes few and sometimes many. It is thus impossible to describe these behaviors as a simple function. Therefore, we installed the tables of experimental distributions at the beam-test, into the simulation program. Since the energy-sharing depends on the incident position, the parametrization was made using 2 GeV/c pion data with several incident points. The energy-sharing among the lead-glass modules for a hadron-induced shower with given total energy E, is reproduced as follows.

The sharing program accepts E, p, and the injection point for the hadron, where E is determined by the procedure described in the previous section. Because the lateral extension of shower cannot be independent on E/p, we classified E/p into three regions, which are $0 < E/p < 0.4$, $0.4 < E/p < 0.8$, and $E/p > 0.8$. The injection point is quantized to the nearest one of the five points, **A**, **B**, **C**, **D**, and **E** at the beam-test considering the spatial symmetry of x and y directions. Following random numbers will be generated by means of the real distributions at the beam-test.

First, we decide the random number of hit counters N_{hit} from one of the 3×5 distributions according to the total energy and the injection point. For example, figure C.4 shows the N_{hit} spectra.

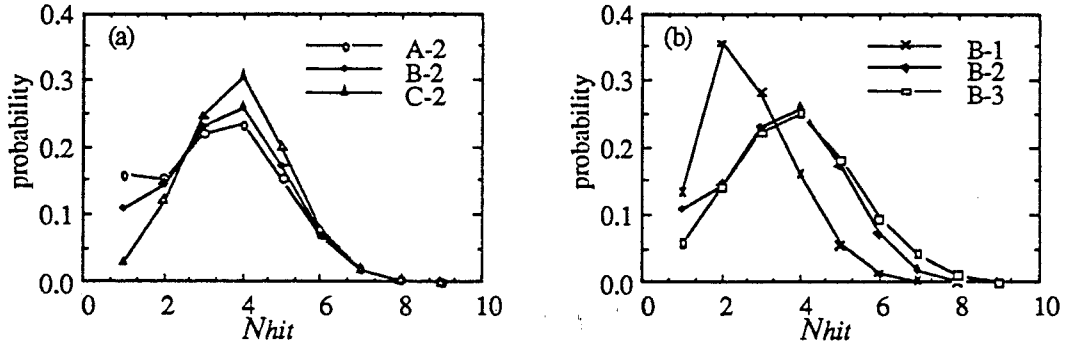

Figure C.4 Distribution of number of hit counters for a hadron, (a) incident at point A (A-2), B (B-2), and C (C-2) resulting to $0.4<E/p<0.8$, (b) incident at B with $E/p<0.4$ (B-1), $0.4<E/p<0.8$ (B-2), and $E/p>0.8$ (B-3).

Next, we decide the hit modules from those, numbered between 1 and 9 as shown in figure C.2, in the descending order of energy by using the distribution. For example, figure C.5 shows the the frequencies of the modules for each order of hits when a hadron injected at **B**, where the small correlation to E/p is neglected. In generating the random number of the counter number, the probabilities of already hit modules are removed and those of unhit modules are stacked. Modules beyond the fourth hit are selected using the same probabilities as for the fourth module.

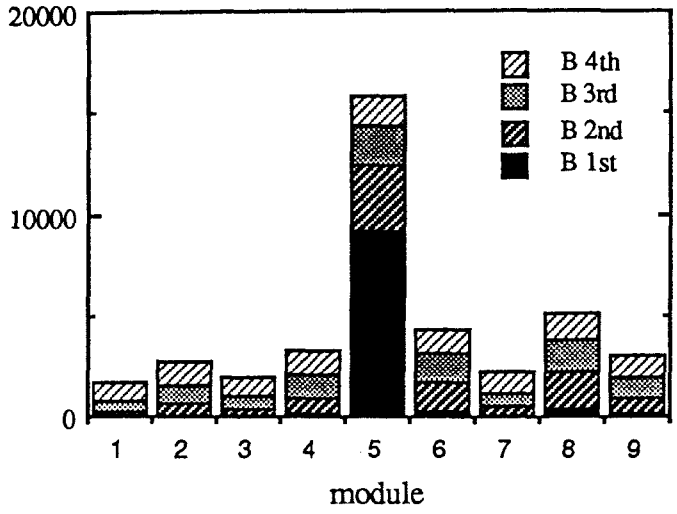

Figure C.5 Stacked histogram of counter number for each hit in descending order of energy for a hadron incident at B.

The energy deposit of each hit module is generated by the distribution of the module energy fraction with respect to the rest energy. The fraction is defined in the region $1/N_{rest}$ to 1, where N_{rest} is the number of the remaining hit modules. Redefining the energy fraction into the range (0,1), we defined parameter X_i as follows;

$$X_i = \frac{N_{rest}\frac{E_i}{E_{rest}} - 1}{N_{rest} - 1},$$

where E_i and E_{rest} are the energy of module i and of the remaining energy to be shared. For example, figure C.6 shows the distributions of X_i for the case, $0.4 < E/p < 0.8$ and the number of hit modules of 4. We have ignored the dependence on injection point and on E/p for the hit modules beyond the second hit which was not clearly seen in actual.

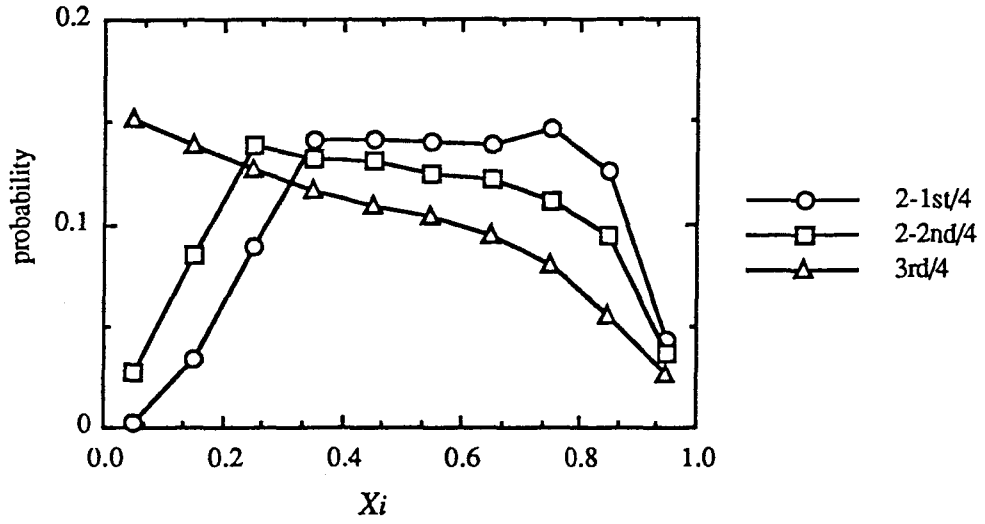

Figure C.6 Distribution of energy fractions with respect to the remaining energy to be shared, when a hadron injects at **B** with $0.4<E/p<0.8$ (first and second) and with number of hit counters of 4.

In above simulation procedure, we cannot help ignoring the correlation between the modules because it is too difficult to implement it into the simulation.

C.5. Performance of the simulation

Here we show the examples exhibiting the performance of the simulation program. Figure C.7 shows the comparisons of distributions between the data and the simulation for charged clusters. The distributions of the Monte Carlo simulation was made using event generator JETSET 6.3 and detector simulator VMONT which this simulation program was installed.

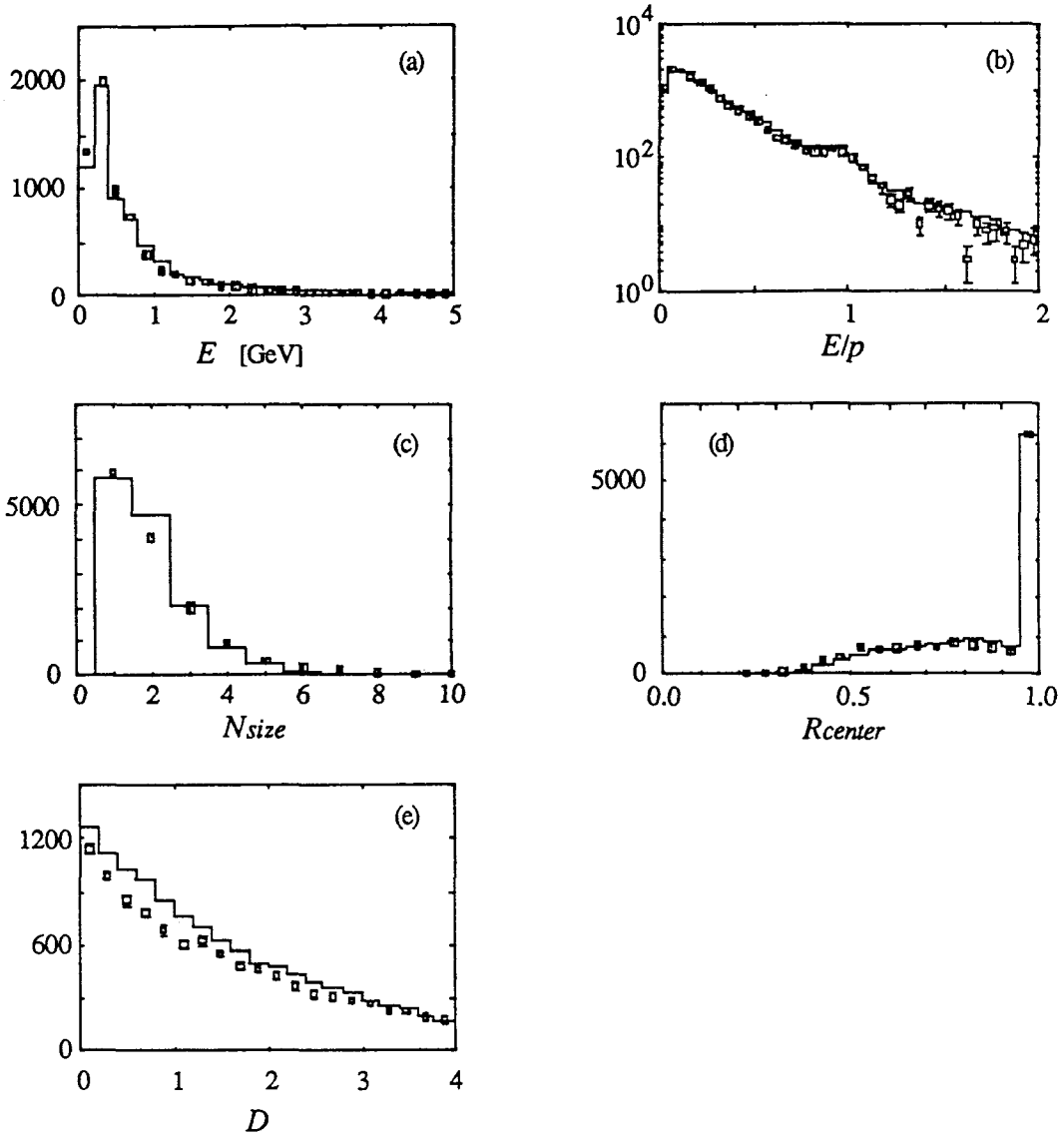

Figure C.7 Comparison between the distributions in the data (square) and in the simulation (histogram), (a) charged cluster energy E, (b) E/p, (c) number of modules in a cluster N_{size}, (d) energy fraction of central module R_{center}, and (e) track-cluster matching parameter D (see chapter 4 of the text).

Since cluster energy was used in the parametrization, both E and E/p in figure C.7 shows good agreement between the data and the simulation. Number of modules belonging to a cluster, N_{size}, and fraction of energy of the most energetic module to cluster energy, R_{center}, also shows good agreement. However, there is a deviation between the data and the simulation in track-cluster matching parameter D defined in chapter 4 of the text. The observed deviation can be understood as follows. The correlation of energies between the modules in a cluster, due to the inclination of particles in a hadronic shower, is expected to make a large displacement of the shower center. Therefore, the lack of such a correlation in the simulation must be responsible to the deviation. Moreover, the shower extension beyond more than 3×3 modules and nuclear

interaction before the calorimeter which also tend to make a laterally extended shower are not supported in the simulation. These defects must enhance the deviation, too.

Since this simulation procedure dose not trace the physics processes and thus dose not always reproduce observables except for the spectrum of total energy or the lateral spread of the shower which were used in the parametrization. The lack of the capability to reproduce the realistic fluctuation of shower center position for hadrons invalidate the direct use of this simulation in estimating hadron background in electron candidates.

Appendix D Preparation of electron sample for the study of electron identification

The Monte Carlo simulation program, VMONT, is sufficiently reliable to reproduce the response for e, where the energy deposit given by EGS program is artificially smeared to reproduce the realistic resolution. Since the lateral spread of the shower is not corrected, there remains some deviations mainly caused by the lack of the optical treatment of Cerenkov light. Therefore, we estimated the efficiency of the electron identification procedure for e by using real data sample. In order for these estimation, we made e sample from the collected data as follows.

The e sample was collected from the reactions, $ee \rightarrow e(e\gamma)$ and $ee \rightarrow ee(ee)$, where the particles in the parenthesis might escape along the beam-pipe and not be detected. We commonly required in order to select them:

(1) Total energy in LG is greater than 3.0 GeV.

(2) All the CDC tracks satisfy both $p > 1.0$ GeV/c and $|\cos\theta| < 0.75$.

(3) There is no LG clusters with $E > 0.3$ GeV outside the 10° cone around the expected hit point of the track.

For e from $ee \rightarrow ee(ee)$ reaction, we added the requirements:

(4) The number of CDC tracks is two.

(5) Both two tracks satisfy $p < 5$ GeV/c.

(6) The acolinearity angle between the two tracks is greater than 10°.

(7) The opposite track in the event is e-like to have $E/p > 0.8$.

While for the $ee \rightarrow e(e\gamma)$ sample, we simply required:

(4') The number of CDC tracks is one.

The selection was applied to a part of Process-1 data and the obtained sample includes 2012 e's. The momentum distribution is shown in figure D.1. The $e(e\gamma)$ sample was considered to be nearly background-free and the background contamination in $ee(ee)$ sample mainly from $ee \rightarrow \tau\tau$, $\tau\tau\gamma$, and $ee\tau\tau$ processes was estimated to be less than a few percent. It should be remarked that we must correct the biases caused by a hard bremsstrahlung, such as tracking-failure and making additional clusters from radiated γ's with $E > 0.3$ GeV outside the cone. These losses were estimated by using VMONT program to be less than 1 % for the e sample.

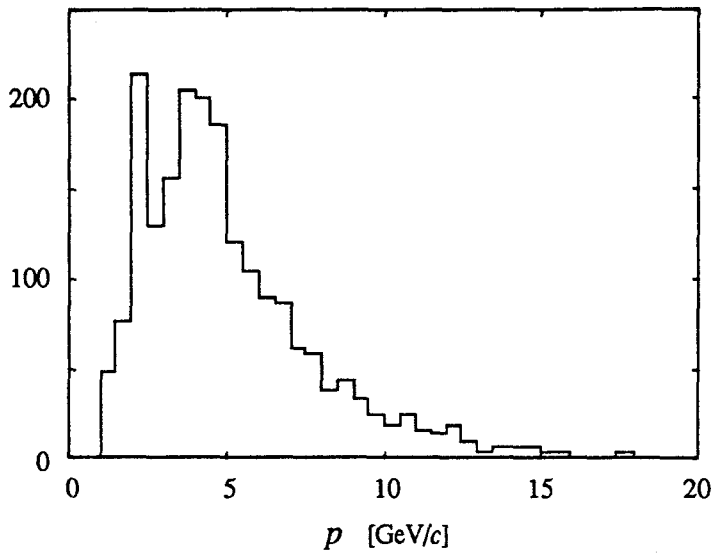

Figure D.1 Momentum distribution of the e sample, where the peak around 2 GeV/c came from $eeee$ reaction requiring that the opposite track to be p>1GeV/c and one around 4 GeV/c came from $ee\gamma$ reaction with the trigger condition (LG total energy trigger).

Acknowledgements

I had a very exciting time throughout my research days in VENUS collaboration. Especially when our VENUS detector began to work in November 1986, I was extremely glad to contribute a little to the detector development. Since then, TRISTAN had been giving us hopeful data with world-highest energy to find a new particle for three years. I would like to acknowledge all the people who made this experiment possible.

My thanks firstly go to Prof. Y. Nagashima, who gave me an opportunity to participate in VENUS collaboration. I could not accomplish this thesis without his continuous encouragement and effective suggestions.

I would like to thank Prof. S. Sugimoto for his patient guidance when I used to know nothing about high energy physics. I thank Prof. Y. Suzuki, Dr. J. Haba, and Dr. M. Takita for their helpful advices and fruitful discussions throughout my study.

I would like to acknowledge many collaborators in KEK where I had proceeded my research. I would especially like to thank Prof. F. Takasaki who guided me and taught me so much about physics with electron identification. I thank Prof. K Ogawa, Dr. T. Sumiyoshi, and Mr. K. Hayashi who worked with me for the construction and the operation of the lead-glass calorimeter. I thank Prof. K. Amako, Dr. J. Kanzaki, and Dr. T. Tsuboyama for their helpful support in offline analysis. It should be noted that this experiment would have been impossible without the invaluable efforts of all the staffs of the TRISTAN accelerator and of the TRISTAN computer system.

I thank my seniors, Dr. T. Kamitani, Mr. T. Yamashita, and Mr. H. Osabe, for their useful leads in proceeding the research. I thank my peers, S. Sakamoto, A. Tsukamoto, and T. Uebayashi, who made me enjoy my graduate school life. I also would like to thank all the colleagues in VENUS collaboration and in Osaka University whom I have not mentioned above.

References

[1] S. L. Glashow, Nucl. Phys. **22** (1961) 579,
S. Weinberg, Phys. Rev. Lett. **19** (1964) 1264,
A. Salam, in "*Elementary Particle Theory*" ed. by N. Svartholm (Alqvist and Wiksell, Stockholm, 1968) 367.

[2] M. Kobayashi and K. Maskawa, Prog. Theor. Phys. **49** (1973) 652.

[3] J. E. Augustin *et al.*, Phys. Rev. Lett. **33** (1974) 1406.

[4] M. L. Perl *et al.*, Phys. Rev. Lett. **35** (1975) 1489.

[5] S. Herb *et al.*, Phys. Rev. Lett. **39** (1977) 252.

[6] G. Flügge, in "*Proc. of the 19th Int. Conf. on High Energy Phys.*", Tokyo (1978),
L. M. Lederman, in "*Proc. of the 19th Int. Conf. on High Energy Phys.*", Tokyo (1978).

[7] D. P. Barber *et al.*, Phys. Rev. Lett. **46** (1981) 1663.

[8] R. Brandelik *et al.*, Phys. Lett. B **97** (1980) 453.

[9] B. Adeva *et al.* (Mark-J), Phys. Rev. D **34** (1986) 681,
M. Althoff *et al.* (TASSO), Phys. Lett. B **138** (1984) 441,
H. J. Berend *et al.* (CELLO), Phys. Lett. B **144** (1984) 297.

[10] C. Albajar *et al.* (UA1), Z. Phys. C **37** (1988) 505.

[11] H. Sagawa *et al.* (AMY), Phys. Rev. Lett. **60** (1988) 93,
I. Adachi *et al.* (TOPAZ), Phys.Rev.Lett.**60** (1988) 97.
H. Yoshida *et al.* (VENUS), Phys. Lett. B **198** (1987) 570,
K. Abe *et al.* (VENUS), KEK Preprint **89-135** (1989) (to be published).

[12] C. Albajar *et al.* (UA1), Phys. Lett. B **198** (1987) 271.

[13] G. S. Abrams *et al.* (Mark-II), Phys. Rev. Lett. **63** (1989) 1558,
M. Z. Akrawy *et al.* (OPAL), Phys. Rev. Lett. B **231** (1989) 530,
D. Decamp *et al.* (ALEPH), Phys. Lett. B **231** (1989) 519,
B. Adeva *et al.* (L3), Phys. Lett. B **231** (1989) 509,
P. Aarnio *et al.* (DELPHI), Phys. Lett. B **231** (1989) 539.

[14] C. Hearty *et al.* (ASP), Phys. Rev. Lett. **58** (1987) 1711,
K. Abe *et al.* (VENUS), Phys. Lett. B **232** (1989) 431.

[15] H. Meyer *et al.*(Mark-I), Phys. Lett. B **70** (1977) 469,
W. Bartel *et al.* (JADE), Phys. Lett. B **123** (1983) 353,
D. Errede *et al.* (HRS), Phys. Lett. B **149** (1984) 519,
C. Wendt *et al.* (Mark-II), Phys. Rev. Lett. **58** (1987) 1810.
H. J. Behrend *et al.* (CELLO), Z. Phys. C **41** (1988) 7.

[16] N. M. Shaw *et al.* (AMY), Phys. Rev. Lett. **63** (1989) 1342.

[17] J. D. Bjorken and C. H. Llewellyn Smith, Phys. Rev. D **7** (1973) 887.

[18] F. Bletzacker and H. T. Nieh, Phys. Rev. D **16** (1977) 2115.

[19] E. Farhi and L. Susskind, Phys. Rep. **74** (1981) 277.

[20] B. Schrempp and F. Schrempp, Phys. Lett. B **153** (1985) 101.

[21] P. Langacker, Phys. Rep. **72** (1981) 185,
W. Buchmuller and D. Wyler, Phys. Lett. B **177** (1986) 377.

[22] V. D. Angelopoulos *et al.*, Nucl. Phys. B **292** (1987) 59,
D. Schaile and P. M. Zerwas, CERN-EP/87-**158** (1987) 20.

[23] W. Buchmuller *et al.*, Phys. Lett. B **191** (1987) 442,
A. Dobado *et al.*, Phys. Lett. B **207** (1988) 97.

[24] H. J. Behrend *et al.* (CELLO), Phys. Lett. B **141** (1984) 145.

[25] H. J. Behrend *et al.* (CELLO), Phys. Lett. B **178** (1986) 452,
W. Bartel *et al.* (JADE), Z. Phys. C **36** (1987) 15.

[26] TRISTAN Project Group, KEK Report **86-14** (1986).

[27] VENUS collaboration, KEK Report **TRISTAN-EXP-001** (1983).

[28] Y. Yamada *et al.*, Kyoto Univ. **KUNS-853** (1987).

[29] R. Arai *et al.*, Nucl. Instr. Meth. A **217** (1983) 181,
R. Arai *et al.*, KEK Preprint 88-5 (1988).

[30] Y. Henmi *et al.*, Jpn. J. Appl. Phys. **26** (1987) 982.

[31] R. Arai *et al.*, Nucl. Instr. Meth. A **254** (1987) 317.

[32] T. Uebayashi *et al.*, Nucl. Instr. Meth. A **256** (1988) 457,
Y. Honma *et al.*, Nucl. Instr. Meth. A **274** (1989) 183.

[33] K. Ogawa *et al.*, Nucl. Instr. Meth. **228** (1985) 309,
K. Ogawa *et al.*, Nucl. Instr. Meth. A **243** (1986) 58.

[34] Nippon Kogaku K. K., 2-3 Marunouchi 3-chome, Chiyoda-ku, Tokyo, Japan.

[35] Hamamatsu Catalogue, Hamamatsu Photonics K. K., 1126-1, Ichino-cho, Hamamatsu, Japan.

[36] Y. Fukushima *et al.*, KEK Preprint **88-84** (1988).

[37] Y. Asano *et al.*, Nucl. Instr. Meth. A **259** (1987) 430,
Y. Asano *et al.*, Nucl. Instr. Meth. A **259** (1987) 438.

[38] T. Ohsugi *et al.*, Nucl. Instr. Meth. A **269** (1988) 522.

[39] Y. Arai *et al.*, IEEE Trans. on Nucl. Sci., **NS-35** (1988) 300.

[40] K. Amako *et al.*, Nucl. Instr. Meth. A **272** (1988) 687.

[41] "TKO Specification", KEK Report **85-10** (1985).

[42] Y. Nakagawa *et al.*, Jpn. Jour. Appl. Phys. **25** (1986) 1049.

[43] T. Sumiyoshi *et al.*, Nucl. Instr. Meth. A **271** (1988) 432.

[44] T. Kamitani, Doctor Thesis, Osaka University (1989).

[45] K. Tobimatsu and Y. Shimizu, Prog. Theor. Phys. **74** (1985) 567, **75** (1986) 905, and **76** (1986) 334,

S. Kuroda *et al.*, Computer Phys. Comm. **48** (1988) 335,
S. Kawabata, Computer Phys. Comm. **41** (1986) 127.

[46] J. Fujimoto and Y. Shimizu, Prog. Theor. Phys. **79** (1988) 701.

[47] A. Peterson *et al.* (Mark-II), Phys. Rev. D **37** (1988) 1,
W. Braunschweig *et al.* (TASSO), Z. Phys. C **41** (1988) 359.

[48] B. Anderson *et al.*, Phys. Rep. **97** (1983) 31,
T. Sjostrand and M. Bengston, Computer Phys. Comm. **43** (1987) 367,
T. Sjostrand, Int. J. of Mod. Phys. A **3** (1988) 751.

[49] A. Peterson *et al.* (Mark-II), Phys. Rev. D **37** (1988) 1,
W. Braunschweig *et al.* (TASSO), Z. Phys. C **41** (1988) 359.

[50] F. A. Berends, P. H. Daverveldt, and R. Kleiss, Nucl. Phys. B **253** (1985) 441,
Computer Phys. Comm. **40** (1986) 309.

[51] W. R. Nelson *et al.*, SLAC-**265** (1985).

[52] F. A. Berends, R. Kleiss, and S. Jadach, Nucl. Phys. B **202** (1982) 63,
Computer Phys. Comm **29** (1983) 185.

[53] E. Etim, G. Pancheri, and B. Touschek, Nuovo Cimento B **51** (1967) 276.

[54] G. P. Yost *et al.* (Particle Data Group), Phys. Lett. B **204** (1988) 54.

Table Captions

Figure Captions